Remote sensing geological structures using high resolution Digital Elevation Models

---

Matthew J. Cracknell BSc. (UTAS)

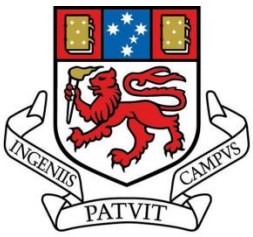

UNIVERSITY OF TASMANIA

A research thesis submitted in partial fulfilment of the requirements of the degree of Bachelor of Science with Honours

Primary supervisor: Dr Michael Roach

Associate supervisors: Dr Arko Lucieer (GES) & Dr David Green (MRT)

Project Sponsor:

DEPARTMENT of INFRASTRUCTURE, ENERGY & RESOURCES

Mineral Resources Tasmania

School of Earth Sciences, University of Tasmania

November 2009

Take a little walk to the edge of town and go across the tracks
Where the viaduct looms, like a bird of doom, as it shifts and cracks
Where secrets lie in the border fires, in the humming wires
Hey man, you know you're never coming back
Past the square, past the bridge, past the mills, past the stacks

On a gathering storm comes a tall handsome man
In a dusty black coat with a red right hand

He'll wrap you in his arms, tell you that you've been a good boy
He'll rekindle all the dreams it took you a lifetime to destroy
He'll reach deep into the hole heal your shrinking soul
But there won't be a single thing that you can do
He's a god, he's a man,
He's a ghost, he's a guru

They're whispering his name through this disappearing land
But hidden in his coat is a red right hand

You don't own no money?
He'll get you some
You don't have no car?
He'll get you one

You don't have no self-respect, you feel like an insect
Well don't you worry buddy, cause here he comes
Through the ghettos and the barrio and the bowery and the slum

A shadow is cast wherever he stands
Stacks of green paper in his red right hand

You'll see him in your nightmares,
You'll see him in your dreams
He'll appear out of nowhere but he ain't what he seems
You'll see him in your head, on the TV screen
And hey buddy, I'm warning you to turn it off
He's a ghost, he's a god,
He's a man, he's a guru

You're one microscopic cog in his catastrophic plan
Designed and directed by his red right hand

Red Right Hand – Nick Cave, 1994

Declaration

No material presented in this thesis has been accepted for the award of any other degree or diploma in any tertiary institution. To the best of my knowledge and belief, contains no material previously published by any other person, except where due reference is made in the text of the thesis.

Matthew J. Cracknell BSc.

13th November 2009

Abstract

The morphology of the Earth's surface is intimately related to geological phenomena. Lithological contrasts, in conjunction with the three dimensional (3D) geometry of geological structures, influence the spatial distribution of local scale erosional landforms. This is primarily a function of differential relative rates of weathering and erosion. Topographic discontinuities (i.e. rapid changes in elevation) can be used as proxies for the identification of geological structural trends.

A high resolution Digital Elevation Model (DEM), generated from Light Detection and Ranging (LiDAR) remote sensing data, is used here to identify and isolate local scale geological features. Methods for the enhancement of topographic discontinuities, manual selection and extraction of geological features, and automated estimation of best-fit planes representing bedding surfaces are presented and evaluated.

Enhanced curvature images were most useful for geological interpretation. Manual methods for feature extraction were more successful than automatic techniques but are subjective and relatively time consuming. Field based observations, remotely sensed structural data and curvature images have been used to interpret local and regional scale structural features in complexly folded Mathinna Group rocks in northeast Tasmania. In most cases, bedding plane orientations derived from the LIDAR DEM correspond reasonably well with field structural measurements.

The techniques developed to extract geological data from high resolution DEMs clearly compliment field based geological mapping and structural interpretations. The software and procedures for DEM interrogation are effective but workflows need to be optimised to make the interpretation process more interactive.

Acknowledgements

I am indebted to the intellectual and practical assistance provided by my supervisors throughout the year. Without their help this thesis would not have evolved from its conceptual origins and materialised into the real world. Special thanks must go to Dr D. Green for his tireless corrections and encouragement in all things geological. Thanks also to Dr A. Reading, Assoc. Prof. R. Berry, Dr A. McNeill and Dr D. Selley for answering my random and out of context questions during the last six months.

I would also like to thank Mineral Resources Tasmania for providing the Digital Elevation Models used in this project and their generous financial assistance.

Thanks to J. O'Farrell, Dr D. Green and L. Graham for the much needed assistance with python and the occasional shoulder to cry on. I am especially grateful for James' rapid introduction to the finer intricacies of Classes and Dictionaries, the majority of which still elude me.

Many thanks to the earth science Honours students of 2009; it was a pleasure to share with you our bitter and twisted induction to the world of academia. Special thanks to K. Knight, the many cups of gut rot combined with insightful and stimulating dialogue has helped me get through this year.

Lastly, I must thank Mark Benz for running manically up and down hills with me in the field while simultaneously wielding a geo hammer...Oh, and also for not getting into a fight at the Fingal Hotel.

Table of Contents

List of Figures

List of Tables

1. Introduction

Earth surface morphology is intimately associated with the geometry and composition of near-surface geological materials. The surface expression of geological phenomena is principally related to the differential weathering rates of solid Earth materials (Easterbrook, 1999; Wallace, Morris & Howarth, 2006). Geological lineament analysis attempts to associate topographic/geomorphic discontinuities with geological structures and lithological contrasts. Although lineaments have been shown in some cases to aid the interpretation of regional tectonic structures and the distribution of ore and petroleum deposits, their analysis has been viewed with some scepticism (Rice, 1997; Wladis, 1999; Pluijm & Marshak, 2004). This is because expert visual analysis and manual extraction is often employed to subjectively select linear (or curvilinear) features of interest from remote sensing imagery and/or topographic maps. Light Detection and Ranging (LiDAR) remote sensing systems have the potential to provide geoscientists with high resolution Digital Elevation Models (DEMs) that can be used to define geological features at higher resolutions than could previously be achieved. LiDAR imagery may also enable automated extraction and analysis of lineaments (Wladis, 1999; Wallace, Morris & Howarth, 2006).

1.1. Aims and objectives

This project aims to investigate the application of high resolution DEMs and their derivatives for the analysis of local scale geological structures and lithologies. During the course of this research, methods (manual and automated) for enhancing, selecting and extracting geological features from high resolution DEMs have been investigated. This includes an automated method for calculating planar surfaces from topographic discontinuities representing geological phenomena. Ultimately, the work produced from this project aims to aid geological interpretations using remotely sensed geological structures within a Geographic Information System (GIS).

1.2. Geology and landforms

This project investigates the extraction and classification of topographic discontinuities representing geological features that have unique mappable landform expressions. Topographic discontinuities are defined as rapid changes in elevation over short distances and are primarily expressed as steps or abrupt changes in a landscape. For example, topographic highs (ridges) can be associated with the presence of relatively resistant lithologies (e.g. coarse grained sedimentary

and igneous rocks). Conversely, topographic lows (channels) can be the result of exposing less resistant lithologies (e.g. fine grained sedimentary rocks) or the presence of structures conducive to enhanced weathering and erosion of geological materials (i.e. joint arrays and fracture systems associated with faults) (Easterbrook, 1999; Pluijm & Marshak, 2004; Wallace, Morris & Howarth, 2006). Further details on this topic are provided in Chapter 2.

1.3. LiDAR

Elevation is a critical element in the analysis of spatial relationships (Jensen, 2007). DEMs are commonly stored as continuous surfaces within a grid or raster image format (Lillesand, Kiefer & Chipman, 2007). To date there have been few investigations into the application of high resolution DEMs to lineament studies and geological mapping. Previous studies have been primarily concerned with natural hazard assessment or geomorphological mapping including, detection and monitoring of active fault systems (Blakely *et al.*, 2004; Chan *et al.*, 2007) and landslide zones (Haugerud *et al.*, 2003; McKean & Roering, 2004), and surface morphology (landform) mapping and classification (French, 2003; Rutzinger *et al.*, 2007; Hyun-chong, Kampa & Slatton, 2007).

A limited number of studies have investigated the use of high resolution DEMs obtained from LiDAR surveys for purely geological mapping applications. For example, Nyborg, Berglund & Triumf (2007) mapped lineaments (brittle rock structures) in order to characterise hydraulic pathways and relationships in an area being prospected for nuclear waste storage. Whereas, Wallace, Morris & Howarth (2006) used 2 m resolution DEMs to map local scale structural trends (defined as ridgelines) and concluded that morphological differences could be discerned between varied geological terranes. Wallace, Morris & Howarth (2006) suggested that using LiDAR DEMs allowed for the detection of short wavelength features and provided analysts with superior vertical and lateral accuracy as compared to traditional remote sensing technology (i.e. Side-Looking Aperture Radar).

The principle of LiDAR systems is based around calculating range (distance) by measuring the time taken for a laser pulse return between source (transmitter) and target (reflecting surface or object) (Wehr & Lohr, 1999). By using the range between source and target and knowing the precise location and orientation of the transmitter, the elevation of target surfaces can be determined. LiDAR is a cost-effective method for obtaining precise elevation data over large areas of the Earth's surface (as compared to photogrammetric methods or field surveys) (Baltsavias,

1999; Charlton, Large & Fuller, 2003). Because LiDAR has the capability to some extent to "see" though vegetation and detect reflections from bare Earth surfaces it can be used to generate accurate "bare earth" DEMs (Nyborg, Berglund & Triumf, 2007). Today, LiDAR is becoming standard practice for the remote acquisition of discrete point elevation data for the generation of high resolution DEMs (Liu, 2008). Summaries of LiDAR data acquisition and methods used for generating the high resolution DEMs used during this project are provided in Chapter 3.

1.4. Lineament enhancement, selection and extraction

There are a number of sequential stages that must be addressed when carrying out lineament studies using digital datasets (Koike, Nagano & Ohmi, 1995; Wladis, 1999; Haugerud *et al.*, 2003; Pluijm & Marshak, 2004; Ekneligoda & Henkel, 2006). They include: the enhancement of target features; manual or automated selection and extraction of features using observational criteria or defined numeric thresholds; association of spatial properties to the extracted features; validation of results; and interpretation of their geoscientific significance via the integration of other datasets (i.e. field data, geophysics) in a GIS.

The ability to remotely sense local scale geological features and extract bedding plane information has only recently been presented in a highly technical paper authored by Fernández *et al*, (2009). In this paper, Fernández *et al.* (2009) outline automated developmental software for the integration of multiple geological datasets including, field structural measurements, geological maps and digitised geological features. Datasets are combined to produce 3D "ribbons" representing geological contacts while simultaneously defining structural features such as fold axial planes.

Chapter 4 provides an outline of the most recent methods developed for both manual and automated lineament enhancement, selection and extraction. Specific attention is placed on current advanced automated methods for feature selection and extraction techniques including morphological filters (Wood, 1996) and point cloud analysis (Ronacella & Forlani, 2005). Chapter 4 concludes with a summary of the two-dimensional (2D) and three-dimensional (3D) spatial attributes that can be associated to remotely sensed geological features, facilitating their analysis and classification.

1.5. Study area

The project study area is located in north eastern Tasmania, approximately 2 km south of the township of Mathinna. The total area under investigation is approximately 50 km^2. Selection of a study area was limited to locations where LiDAR data has been collected previously. Figure 1.1 provides a regional Tasmanian map with the general location of the study area marked. A summary of the general geology of northeast Tasmania with specific attention on the geology of the study area is presented in Chapter 5.

During this project, a field validation exercise was carried out to assess the accuracy of the extracted planes and geological features (if any) defined by the selected lineaments. Field observations included identifying the geological features that influence a particular topographic discontinuity, then measuring, and if possible, identifying the dominant geological structure expressed. In addition, numerous orientations of bedding planes, cleavage planes and fault planes, and trend and plunge of fold hinges were measured for the comparison of the remotely sensed structures to real world geological features.

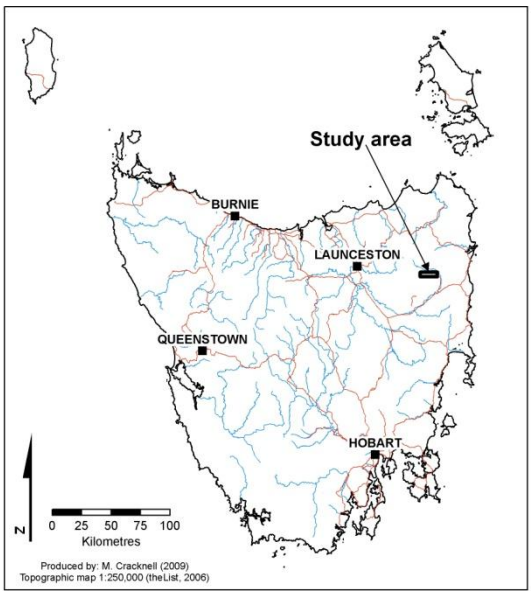

Figure 1.1 Study area location, NE Tasmania

1.6. Methodology

As part of this study, DEM image enhancement techniques have been explored at different scales with the aim of highlighting topographic discontinuities or edges in the landscape. The ultimate aim of these studies was to develop an automated method for identifying edge features that represent geological lineaments, and to extract geological structures (and lithologies if possible) based on DEM derivatives and landscape feature extraction methods. Unfortunately, the results of the automated methods were less than reliable. The most promising results, given the limited time available for this research, have been obtained from manual methods for selecting geological features from DEM 2nd derivative surfaces.

Once a lineament has been identified and isolated it is possible to extract the 3D coordinates of points (i.e. x, y and z) representing the feature within a GIS. These 3D points can be used to calculate best-fitting planes via a method proposed by Fernández (2005), called Moment of

Inertial (MOI) analysis. The MOI analysis method was automated within software developed using python programming language. Details of the manual methods used to enhance, select and extract geological features from high resolution DEMs and the automated MOI best-fit plane algorithm are provided in Chapter 6.

1.7. Results

Initial interpretation of the orientations of best-fitting planes generated from the MOI results and from manually selected geological features was difficult. Qualitative and quantitative analysis of the comparisons between field data (including data supplied by Mineral Resources Tasmania (MRT)) and the MOI results showed that many best-fitting planes simulated the slope and aspect of the terrain rather than the orientation of geological structures. Thus an attempt to improve the reliability of MOI results via filtering was carried out. Chapter 7 details the findings obtained throughout the course of this research project.

1.8. Digital data

Accompanying this thesis is a DVD containing: a digital copy of the thesis, its figures and appendices; software written for the enhancement of DEMs and calculation of best-fit planes from 3D georeferenced points. Included in the DVD are the digital datasets generated as part of this research. Further information is provided in the readme.txt file.

2. Geomorphic expression of lithology and geological structures

Linear features visible at the Earth's surface, aligned in a preferred direction, differ from the patterns of nearby features and presumably conform to geological phenomenon are known as topographic lineaments (O'Leary, Friedman & Pohn, 1976; Maukisch *et al.*, 2007). This project is primarily concerned with (geological) structural lineaments, which can be defined as the structurally controlled alignment of topographic discontinuities such as ridges, channels and escarpments. In most cases, structural lineaments are the geomorphic expression of geological structures such as faults, joint arrays, folds, dykes and lithological contacts (i.e. bedding planes) (Easterbrook, 1999; Pluijm & Marshak, 2004). Detailed studies of structural lineaments can lead to a better understanding of the distribution of structural features, aid the identification of ore/petroleum deposits and shed light on tectonic history/seismicity at regional scales (Pluijm & Marshak, 2004; Graniczny, Mizerski & Piatkowska, 2005). However, the evolution of the landscape is not controlled by lithology contrasts and the 3D geometry of geological materials alone, but also to varying degrees by climate, biological activity, topography and time. Although absolute rates of weathering and erosion are controlled by the five interdependent influences mentioned above, it is the relative weathering and erosion rates of geological materials that generate high frequency topographic discontinuities. Thus we can simplify gross landscape evolution, and assume that compositional contrasts of near surface geological materials and the presence of brittle geological structures in discrete zones are the primary factors to be considered when interpreting structural lineaments (Easterbrook, 1999; Prothero & Schwab, 2004).

2.1. Lineaments

Lineaments are expressed as anomalies or discontinuities within the surrounding terrain as observed by remotely sensed data (O'Leary, Friedman & Pohn, 1976; Wladis, 1999; Argialas & Mavrantza, 2004; Rutzinger *et al.*, 2007). That is, they are expressed as rapid changes in a surface characteristic, specifically related to contrasts within underlying geological materials (whether geometric or compositional). A formal definition of lineaments was primarily developed in the late 70s' using work published by Hobbs (1904) and Hobbs (1912) in O'Leary, Friedman & Pohn (1976 p. 1463),

> *"A lineament in an essentially geomorphological sense...is a mappable, simple or composite linear feature of a surface, whose parts are aligned in a rectilinear or slightly curvilinear relationship and which differs distinctly from the patterns of adjacent features and presumably reflects a subsurface phenomenon."*

Lineaments (not necessarily topographic) can be observed within a range of remotely sensed datasets such as: geophysical imagery (i.e. gravity and magnetics (Sarp & Toprak, 2007)); multi and hyperspectral satellite imagery (Argialas & Mavrantza, 2004); airphotos (Koike, Nagano & Ohmi, 1995); radar (GahGah *et al.*, 2007); and topographic maps and DEM imagery (Raghavan, Wadatsumi & Masumoto, 1993). In the examples mentioned above, all lineaments are observed at regional scales (i.e. 10-100 km) (O'Leary, Friedman & Pohn, 1976; Clark & Wilson, 1994; Wladis, 1999; Pluijm & Marshak, 2004). Presumably this is a function of the available resolutions associated with commonly used remotely sensed data (i.e. satellite imagery). However, high resolution LiDAR datasets now provide researchers with the possibility of mapping local scale discontinuities (Wallace, Morris & Howarth, 2006; Rutzinger *et al.*, 2007; Chan *et al.*, 2007), thus reducing the regional scale limitations of lineament characterisation.

The primary lineament type investigated in this project are defined as topographic (O'Leary, Friedman & Pohn, 1976) or structural (Pluijm & Marshak, 2004); that is, they have a geomorphic expression or landform characteristic and can be identified from DEMs. O'Leary, Friedman & Pohn (1976) go on to state the general characteristics that "topographic" lineaments must express are:

- geomorphic expression (topographic discontinuity)
- continuous or composite in nature
- alignment in a single direction (which may or may not conform to a regional trend)
- straight or slightly curved
- occur at regional scales and extents (traditionally)
- possess scale dependent relationships

Examples of common geomorphic features that can be considered as lineaments include linear ridges, channels and escarpments. These are essentially discriminated by rapid changes in elevation over short distances (relative to the scale of observation) (Easterbrook, 1999; Pluijm & Marshak, 2004). Lineaments can be negative (e.g. channels and depressions) or positive (e.g. ridges and escarpments) (O'Leary, Friedman & Pohn, 1976). In addition, a lineament observed at regional scales may look continuous but can in actual fact be composed of smaller contiguous or detached features at local scales observation (O'Leary, Friedman & Pohn, 1976). Therefore, the

regional scale orientation of geological structures can be difficult to measure at local scales due to the presence of cover materials, brecciation or movement due to geomorphic processes. Lineament analysis in a traditional sense can help to constrain the overall trend of a structure rather than the observable non-linear mesoscopic representation of a complex feature (Graniczny, Mizerski & Piatkowska, 2005).

2.2. Weathering and erosion

Weathering and erosion work in combination to denude the landscape over time. Weathering is the decomposition or disintegration of geological materials *in situ* due either to physical or chemical processes or varying combinations of both. Erosion on the other hand, is the subsequent removal and transportation of weathered geological materials from their source.

Dominant weathering processes and absolute rates of weathering for particular geological materials are governed by several mutually dependent factors. These factors include: the type of material being weathered; the climate and hence, availability of water; ambient air temperature; organic activity, in particular the growth of vegetation; topography (i.e. slope, aspect and elevation); and time (Easterbrook, 1999; Prothero & Schwab, 2004). For example, in hot and humid climes, the dominant weathering processes are chemical reactions that transform rocks either by their breakdown into ions or the creation of new minerals. In addition, vegetation growth is more vigorous in warm climates and hence increases the ability of roots to wedge rocks apart and exposes them to water and oxygen. Accelerating weathering processes are biologically produced chemical compounds released into the environment. In cold and/or arid climes, where mechanical processes are predominant; freeze-thaw shattering and ice abrasion breaks rocks into smaller pieces and vegetation is more subdued and less vigorous. The examples given are two extremes of many situations. In reality, rates of weathering and erosions are governed by local processes and the regional context of the landscape in question.

We can reduce the complexity associated with absolute rates of weathering and erosion by just considering *relative* rates of weathering and erosion for the specific purpose of understanding the geomorphic expression of near surface geological materials. This requires some understanding of the contrasting weathering susceptibilities of rocks with differing mineral composition (i.e. lithology) and the spatial distribution of bedrock porosity and permeability (i.e. structures) (Easterbrook, 1999; Prothero & Schwab, 2004). It is these physical properties that influence a

particular geological materials resistance to weathering, and thus the propensity for it be eroded, relative to adjacent materials.

2.3. Lithology (compositional contrasts)

The resistance of a geological material to weathering is in part controlled by its mineral composition. Minerals within rocks decompose at the Earth's surface because they may initially have been formed, or were altered at depth, within the crust under different temperature and pressure regimes. As a result, geological materials may be in disequilibrium with the conditions present on the Earth's surface and must change in order to reach equilibrium (Pluijm & Marshak, 2004; Prothero & Schwab, 2004).

2.3.1. Igneous and metamorphic rocks

Most igneous rocks contain high proportions of aluminium, silica and iron, which weather to become aluminium oxide, quartz, iron oxide and clays. Of these, quartz is the most mechanically persistent because of its silica tetrahedral crystal structure and strong Si-O bonds that are difficult to break. Grain size also influences weathering susceptibility. For instance, coarse grained quartz rich rocks (i.e. granites) generally weather more slowly than fine grained rocks (Easterbrook, 1999; Prothero & Schwab, 2004). Therefore, it is more common to find granites at the core of mountain ranges or topographic highs due to their resistance to denudation (Easterbrook, 1999). However, this is not always the case. For example in eastern Tasmania, dolerite (medium to coarse grained mafic rock) outcrops ubiquitously to form plateaus and topographic highs (McClenaghan & Baillie, 1975; Leaman, 2002).

Foliated metamorphic rocks have more fissures and cracks (i.e. cleavage) for water to gain access and increase weathering and erosion rates than un-metamorphosed rocks. In addition, high grade metamorphic minerals are often less stable than magmatic minerals because the extreme temperature and pressure regimes of the rocks origins (Prothero & Schwab, 2004). As a result, some metamorphic rocks have a propensity to be denuded rapidly.

2.3.2. Sedimentary rocks

Most sedimentary rocks were initially clastic or biological sediments, deposited at the Earth's surface and comprised mainly of siliciclastic (persistent quartz and moderately persistent clays) and carbonate minerals (Prothero & Schwab, 2004). Carbonate rocks are relatively easy to dissolve in surface waters, forming distinctive karst landscapes. For simplicity's sake these will not be discussed further. Of more relevance to this project is the contrasting resistance to weathering

and erosion of siliciclastic rocks of differing composition and grain size. At one end of this spectrum are the resistant coarse grained quartz rich rocks, such as conglomerates and sandstones, while at the other are the less resistant fine grained clay rich rocks, such as mudstones and shales. Thus it is common to find sandstones forming ridges and escarpments, and mudstones forming depressions and channels (Figure 2.1) (Easterbrook, 1999).

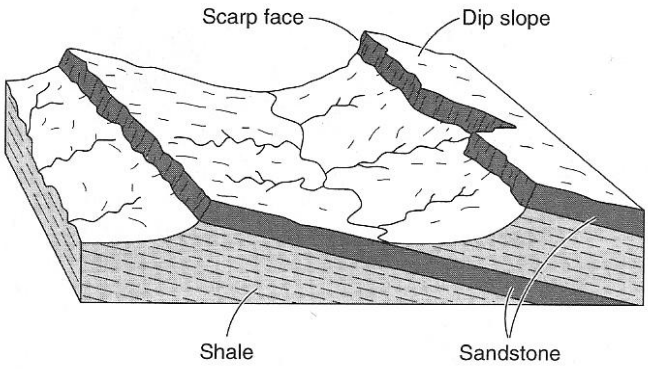

Figure 2.1 Asymmetric topography development due to differential resistance of interbedded and tilted sedimentary units to weathering and erosion (Easterbrook, 1999)

2.4. Structures

Lineaments in many cases represent brittle tectonic structures, which include faults (fracture zones) and joint arrays (Wladis, 1999; Nyborg, Berglund & Triumf, 2007). Nevertheless, lineaments have been associated with other geological structures such as folds and lithological contacts (i.e. unconformities and bedding planes) (Easterbrook, 1999; Maukisch *et al.*, 2007). Weathering and erosion rates of geological structures are primarily determined by the ability of water and oxygen to filter into cracks and fissures, thus accelerating denudation. The scale of the structure under scrutiny, and current rates of deformation are important considerations when identifying and interpreting structural controls on the landscape (Easterbrook, 1999).

2.4.1. Faults

Faults are generated by the tectonic displacement of geological materials. Faults in the landscape can be expressed as topographic highs where offset of the surface has occurred recently (Figure 2.2), or where resistant quartz veins have been precipitated within fractures. Faults can also be expressed as topographic lows where dormant fault zones have been intensely fractured and weathering has taken place within these zones of weakness.

Strike slip faults can display steeply dipping surfaces and in some cases are characterised by stream channel and ridge lateral offset. Low angle reverse faulting, or thrust faults have the ability

to cause large displacement. Thrusts can be expressed geomorphically by irregular outcrop patterns due to gently dipping fault planes and the reduction of bed dip in the hanging wall (Easterbrook, 1999).

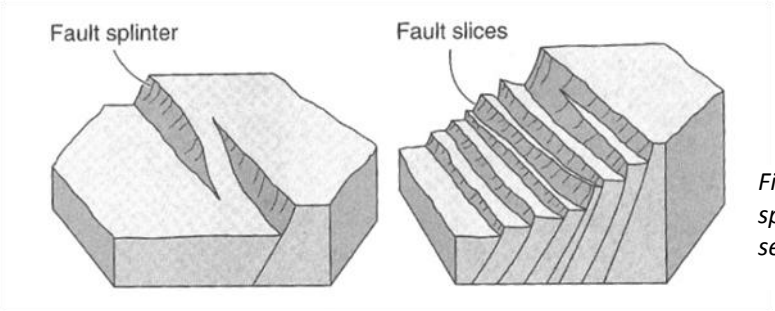

Figure 2.2 Fault slices and fault splinters formed in areas of active seismicity (Easterbrook, 1999)

2.4.2. Joints

Joints are fractures in rocks where no discernable displacement has occurred and often form arrays or dense fracture groups. They occur in many situations but are commonly the result of brittle failure and are often generated perpendicular to the principle axis of compressional stress (i.e. in tensional stress situations) (Pluijm & Marshak, 2004). Contrasting joint patterns develop within sedimentary and igneous rocks (Easterbrook, 1999). In igneous rocks, joints may result from thermal contraction during cooling and develop perpendicular to the igneous body surface (Leaman, 2002). However in the case of granites, which are emplaced at depth within the crust, the process of unloading causes joints to form parallel to the surface thus generating irregular joint arrays. Jointing is typically more regular and closely spaced in sedimentary rocks when compared to igneous rocks. In general, jointing within rocks provides pathways for water, air and roots to penetrate bedrock materials accelerating weathering and erosion. This can lead to the development of preferential drainage patterns depending on the alignment and spacing of the joint array patterns.

2.4.3. Folds

Ductile deformation of sedimentary (originally horizontal) rocks can produce folding. In some situations, ridges and valleys orientations conform to the fold axis. Although this is not always the case, as deformation rates are usually considerably lower than the rates of weathering and erosion. Therefore, these landforms are less likely to conform to 3D rock geometry and more to compositional contrasts and differential resistance to weathering and erosion (Easterbrook, 1999).

In the case of dipping strata, dip and dip direction initially encourages the development of channels and ridges parallel to the direction of dip on exposed resistant beds (Figure 2.1, p.11). The resulting drainage channels can then expose resistant strata, causing them to be reflected perpendicular to the direction of dip. This has the potential to develop over time into a series of

asymmetrical ridges crested with resistant lithologies. The flanks on one side of the ridge conform to bedding dip and dip direction (dip slopes) truncated by scarps exposing less resistant materials on the opposing side. Accumulation of materials (colluvium) at the base of scarps can cause an apparent dip slope of ~25-35°, thus conforming to the angle of repose of unconsolidated clastic materials and obscuring the geological surfaces in question (Easterbrook, 1999).

2.4.4. Unconformities

Extreme examples of unconformity related topography contrasts develop on angular unconformities (Figure 2.3). If the overlying geological unit is composed of resistant sub-horizontal quartz rich rocks, a distinct stepped topographic high such as a plateau can evolve. The underlying folded strata then develops a different geomorphic expression such as the asymmetrical ridge and valley topography described in Section 2.4.3 (Easterbrook, 1999).

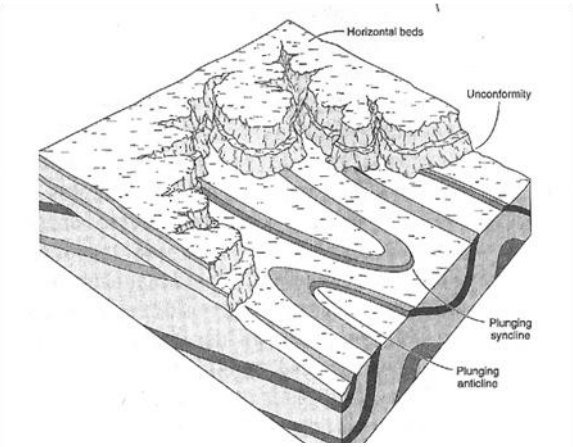

Figure 2.3 Angular unconformity related landform contrasts (Easterbrook, 1999)

Prior to the erosion of an overlying sedimentary unit and exposure of the structures below, drainage patterns can develop freely on the palaeolandscape. In this case, superposed drainage patterns continue to evolve even after the exposure of the underlying folded strata, thus maintaining the general topographic patterns of the previously overlying strata. Therefore, the alignment of ridges and channels can be independent of the structural features within the rocks below an unconformity (Easterbrook, 1999).

2.5. Closing remarks

One must be careful to distinguish between geomorphological and geological phenomena as both can be interpreted as lineaments. For example, Clark & Wilson (1994) analysed lineament orientations associated with drumlins and other glacially derived landforms to determine ice flow paths during the last glacial maxim. In addition, not all valleys conform to zones of fracturing and faulting and not all ridges are the topographic representation of resistant strata. However, the preceding discussion has hopefully assisted in defining some of the potential geomorphic features resulting from compositional contrasts and the 3D geometry of geological materials.

3. Light Detection and Ranging (LiDAR) and DEM interpolation

It is important to clarify the nomenclature used in this project as airborne laser ranging is known by many names. It is variably called Laser-induced Direction and Ranging (LiDAR) (e.g. Charlton, Large & Fuller (2003)), Airborne Laser Scanning (ALS) (e.g. Baltsavias (1999)), Airborne Laser Swath Mapping (ALSM) (e.g. Shrestha *et al.* (2005)) and Laser Detection and Ranging (LADAR) (e.g. Wehr & Lohr (1999)). These acronyms represent the same remote sensing technology. In this thesis, the term Light Detection and Ranging (LiDAR) (e.g. Liu (2008) and Bater & Coops (2009)) will be used as it appears to be the most commonly accepted acronym used in recent times.

Small footprint, full-waveform LiDAR remote sensing systems utilise backscattered laser pulses to image the Earth's surface and near surface objects (i.e. buildings and vegetation). LiDAR systems are comprised of four main components, a laser transmitter and receiver (sensor), Differential Global Positioning System (DGPS), Inertial Measurement Unit (IMU), and digital data storage system (Wehr & Lohr, 1999; Reutebuch, Andersen & McGaughey, 2005; Jensen, 2007). The principle of LiDAR remote sensing is based upon measuring the distance between sensor and target (reflecting surface or object). By knowing the precise distance between the transmitter and target, the location of the transmitter (using DGPS) and its attitude (using IMU), it is possible to determine the 3D position (*x*, *y* and *z* coordinates) of individual targets (Lillesand, Kiefer & Chipman, 2007; Liu, 2008). LiDAR is a cost-effective method (as compared to photogrammetric or field based survey methods) for obtaining dense, randomly distributed point data that represents Earth's surface elevation and can be used to produce high resolution DEMs (Carter *et al.*, 2001; Charlton, Large & Fuller, 2003).

The generation of high resolution DEMs using LiDAR data is becoming standard practice as it offers an effective and reliable means of producing accurate elevation models for terrain analysis (Liu, 2008). LiDAR is currently used for a wide range of applications that include: urban environment and infrastructure mapping (e.g. buildings, bridges and powerlines) (Wehr & Lohr, 1999); hydrological modelling and flood hazard assessment (French, 2003; Mouton, 2005; Hyun-chong, Kampa & Slatton, 2007); forest inventory and monitoring (Reutebuch, Andersen & McGaughey, 2005); coastal mapping and change detection (Shrestha *et al.*, 2005); glacier mass balance calculations (Arnold *et al.*, 2006); and geomorphological mapping and landform classification (Charlton, Large & Fuller, 2003; French, 2003). One of the most important aspects of

LiDAR for applications in terrain modelling is its ability to image the Earth's surface in steep or inaccessible terrain and to penetrate vegetation canopies (Nyborg, Berglund & Triumf, 2007; Lillesand, Kiefer & Chipman, 2007; Liu, 2008). Despite this, there has been limited research into the use of LiDAR high resolution DEMs for earth science applications. Most applications are concerned with geological hazard mapping and assessment via the detection of landslides and the identification of active faults and volcanism (Carter *et al.*, 2001; Haugerud *et al.*, 2003; Chan *et al.*, 2007).

3.1. Basic LiDAR theory and data acquisition

LiDAR data capture systems are active remote sensing systems that transmit and receive reflected laser pulses from an airborne platform. By measuring the two-way travel time of an individual laser pulse and knowing the speed at which light travels, a precise measurement of the distance from sensor to reflecting surface or object can be calculated using the following equation (Baltsavias, 1999):

$$\boldsymbol{R = c\,\frac{t}{2}} \qquad (3.1)$$

Where: R = distance (m) between transmitter and target
c = speed of light (ms^{-1})
t = two-way time (s)

Precise determination of the relative and/or absolute elevation of the Earth's surface and above ground objects such as trees and buildings at a particular point is achieved by integrating distance R with several post-processing steps. Post-processing involves a knowledge of the position of the sensor in space (using DGPS), its attitude (using IMU) (i.e. pitch, roll and yaw of the aircraft carrying the sensor) and the scan angle of the sensor (Baltsavias, 1999; Jensen, 2007; Mallet & Bretar, 2009). Figure 3.1a presents a generalised view of a LiDAR remote sensing system including the important components and parameters of a survey.

Modern LiDAR systems have the ability to detect up to six or seven returns for an individual pulse (Figure 3.1b), thus allowing for the 3D reconstruction of surface features and objects (Mallet & Bretar, 2009). The main use for multiple return data is in the forestry industry, as detailed images of canopy structure and the dimensions of individual trees can be generated (Lillesand, Kiefer & Chipman, 2007). However, for geological interpretations using LiDAR data it is only the Earth surface points or ground returns that are required to produce "bare earth" DEMs.

LiDAR survey parameters such as pulse duration, scanning rate, maximum off-nadir scan angle and flying height can be adjusted to obtain the desired information for a particular application (Wehr & Lohr, 1999). Laser beam divergence and flying height determine the instantaneous laser footprint. The instantaneous laser footprint represents the area illuminated by a single laser pulse and is usually given as a measurement of the diameter of an approximately circular area. It is the dimensions of the laser footprint that determines the scale at which features are imaged, and the nature of the pulse return detected by the scanner receiver (Baltsavias, 1999). On flat terrain at close to nadir angles the laser footprint is approximately circular. At larger scan angles and where surface targets are steep slopes, the laser footprint becomes increasingly elliptical, resulting in a lower energy density and reduced canopy penetration (Hopkinson, 2006). Nevertheless, for most applications the laser footprint is assumed to be circular (Baltsavias, 1999; Wehr & Lohr, 1999).

The Pulse Repetition Rate (PRR) describes the rate of individual pulse transmissions per second. Modern systems have PRRs greater than 200 kHz. PRR, flying height, scanning rate, maximum scan angle and flying speed of the aircraft determine ground return separation, and hence point density (Lillesand, Kiefer & Chipman, 2007). This is an important factor when designing a survey for specific applications as point density has implications for the appropriate resolution of the resulting DEMs.

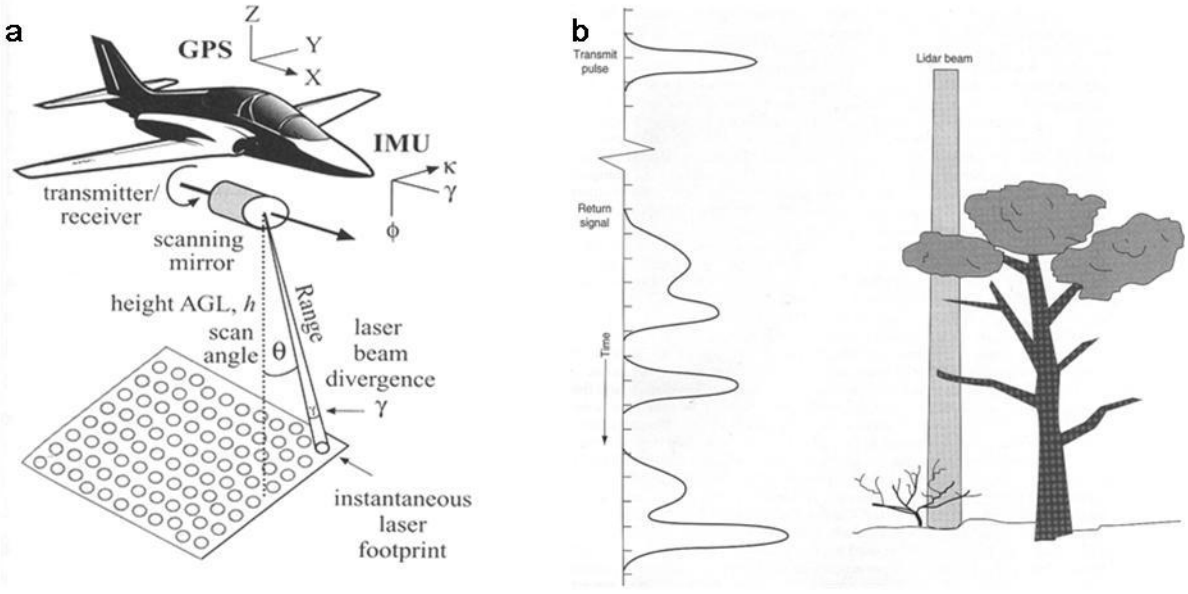

Figure 3.1 LiDAR survey schematic diagrams, a) survey components and parameters (Jensen, 2007), b) full-waveform multiple pulse return characteristics as caused by intercepted surface objects (Lillesand, Kiefer & Chipman, 2007)

3.2. LiDAR survey precision and accuracy

There are two main sources of inaccuracies associated with LiDAR collection systems: positional error and ranging error. Positional error influences point cloud horizontal accuracy and can be attributed to inconsistencies in determining the location of the aircraft (DGPS) and its orientation (IMU) (Hodgson & Bresnahan, 2004). Sources of ranging inaccuracies, in order of decreasing importance, include laser timing errors, laser system stability, photon scattering, variations in pulse amplitude, and background noise (i.e. changes in temperature and ambient light conditions) (Baltsavias, 1999; Evans & Hudak, 2007). Horizontal positioning errors are typically larger than vertical position errors (Hodgson & Bresnahan, 2004; IGI mbH, 2009). Positional inaccuracies can cause significant errors to creep into LiDAR point cloud datasets, especially in areas of steep slopes or complex terrain. Hodgson & Bresnahan (2004) investigated LiDAR DEM accuracy and found that in areas with slopes greater than 25° the elevation error was twice that of flat terrain.

3.3. Ground point classification

Separation of ground and non-ground points (classification) is a critical step for producing accurate DEMs. Point classes are used to filter the post-processed LiDAR datasets for interpolation and gridding into continuous surfaces for a desired application. Liu (2008) provides an excellent summary of the currently available point classification algorithms; these include interpolation, slope and morphology/curvature methods. LiDAR survey providers commonly deliver the LiDAR datasets as a collection of classified 3D points. The output 3D coordinates of a point cloud dataset is inherently georeferenced allowing for its rapid integration into GIS (Lillesand, Kiefer & Chipman, 2007). The dataset is subjected to the point classification process giving each of the points within the dataset an attribute. This attribute is related to the elevation of the reflecting surface relative to the ground. The classification process is initiated by separating returns based on the pulse return number (i.e. first, last or intermediate), then undergoes further classification where points are separated into ground returns, vegetation canopy categories and buildings.

Information provided within the TerraScan User's guide (Soininen, 2005) outlines the algorithm behind the classification of the LiDAR data used in this project. This algorithm is an iterative slope based filtering method that initially identifies the lowest point within a local area and assumes that it represents a ground return. The algorithm then generates a Triangular Irregular Network (TIN) model using selected ground points (local lows). The next step of the process identifies

points within a user defined neighbourhood (distance parameter) and calculates the slope of the line between these points relative to the TIN surface (Figure 3.2). Identified points are classified as ground or non-ground returns based on a user defined slope threshold (angle parameter). Low slope thresholds are best applied to areas of flat or undulating terrain. In areas of steep slopes or more complex terrain, higher slope thresholds are necessary. Despite this, the algorithm described above still requires manual corrections and validation of the classified points.

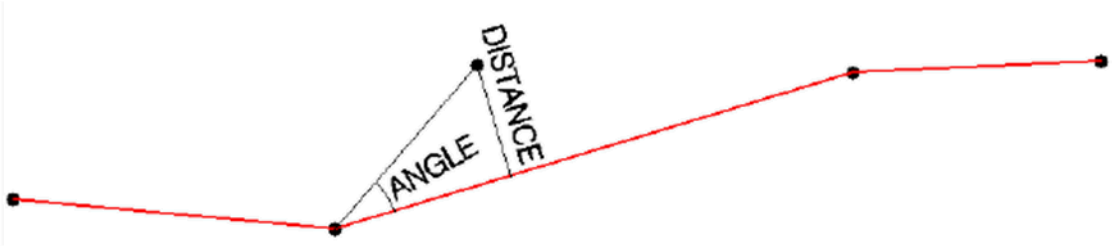

Figure 3.2 Graphic depiction of TerraScan's LiDAR point cloud classification algorithm (Soininen, 2005)

3.4. LiDAR system and specifications

The data used in this project were collected by Digital Mapping Australia Pty Ltd (DiMap) using a LiteMapper 5600 small footprint, full-waveform laser scanner system. The following specifications were provided with the LiDAR data used in this project (DiMap, 2009). The data capture rate averaged 2 points m^{-2} and the minimum data capture was not less than 1 point m^{-2}. All spatial data was provided in Universal Transverse Mercator (UTM) coordinates in the Geodetic Datum of Australia (GDA94 (MGA zone 55G)), and using the Australian Height Datum 1983. The spatial positioning of points is within ± 0.15 m of their true position in x, y and z dimensions. Maximum LiDAR scan angle does not exceed 30° off-nadir. Overlap between swaths average 30%, with a minimum of 10%. Incorrectly classified ground points do not exceed 0.01%. The data was provided as 1 km x 1 km tiles in LAS file format. The LAS file includes:

- spatial position (x, y, z coordinates in UTM GDA94 (MGA zone 55G))
- intensity (DN)
- number of returns per given pulse
- return number (n)
- scan angle (°)
- point source (ID)
- classification (Unclassified, Ground, Low Vegetation, High Vegetation)
- Global Positioning System (GPS) time (UTC)

3.5. DEM construction

This project has used points classified as ground returns in the point cloud dataset to produce a "bare earth" DEM. It is apparent that no single interpolation technique is superior to all others in every respect. In this case, using information provided in Bater & Coops (2009) and iterative experimentation with different gridding algorithms and interpolation parameters, the minimum curvature spline interpolator has been employed. The following sections describe the interpolation algorithm, developed by Bombadieri, Green & Mazengarb (2009) for the creation of the DEM used in this project.

3.5.1. Preparation of point cloud data

The initial preparation of the ~1 x 1 km tiled point cloud dataset used Lastools (Isenburg & Shewchuk, 2009). Lastools is a very efficient, freely available command prompt based software package for editing, filtering and viewing LiDAR data (LAS file format). The steps involved in the preparation of LAS files for interpolation (i.e. generation of a gridded DEM) are:

- merging and clipping tiled LAS files
- filtering points other than ground returns (class 2)
- exporting LAS binary file to ASCII text file format (with ability to select point attributes such as elevation, x and y coordinates, GPS time, and point classification)

3.5.2. DEM interpolation

ArcGIS has the ability to automate DEM production using python based coding (ESRI, 2008). This allows for the importation of filtered point cloud data into ArcGIS and the ability to program the output grid cell size and optimal interpolation parameters for the generation of continuous surfaces. Interpolation error assessment conducted by Bater & Coops (2009) concludes that the best DEMs for geological applications are obtained using a spline (minimum curvature) interpolator with tensioning and sub-metre grid cell sizes. A spline interpolator applies two conditions on the resulting continuous surface; the surface must pass exactly through the data points and the cumulative sum of the squares of the 2^{nd} derivative of the surface at each point must be a minimum (ESRI, 2008).

There are several parameters available when generating spline surfaces in ArcGIS, Regularized [sic], Tension, point search radius and output grid cell size. Higher values of the Regularized weight leads to the production of a smooth surface together with smooth 1^{st} derivative surfaces. The Regularized parameter is important if the 2^{nd} derivative of the interpolated surface is to be calculated without fitting quadratic surfaces. Zero values for the Tension weight results in a basic thin plate spline or stiff surface (i.e. reduced curvature between points). Increasing Tension

weights creates a surface that begins to approximate the form of a membrane or rubber sheet. The point search radius defines the number of points surrounding the target grid cell. More information regarding the mathematical basis for these parameters can be accessed in the ArcGIS help files (ESRI, 2008).

The DEMs produced for this project were given the following parameters (Bombadieri, Green & Mazengarb, 2009):

- Regularized weight = n/a
- Tension weight = 1
- Point search radius = 30
- Grid cell size = 0.5 m

A 30 point search radius was chosen for DEM interpolation so that a minimum number of 4 points normal to the scan line are included in interpolation process. The 30 point search radius allows for a 2nd order (spline) surface to be fitted to the point data confidently, allowing for variations in the minimum point separation (D. Green pers. comm., April 2009) (Figure 3.3a). Actual ground point spacing is on average less than the theoretical spacing thus the search area varies as a function of point density (Figure 3.3b, c and d).

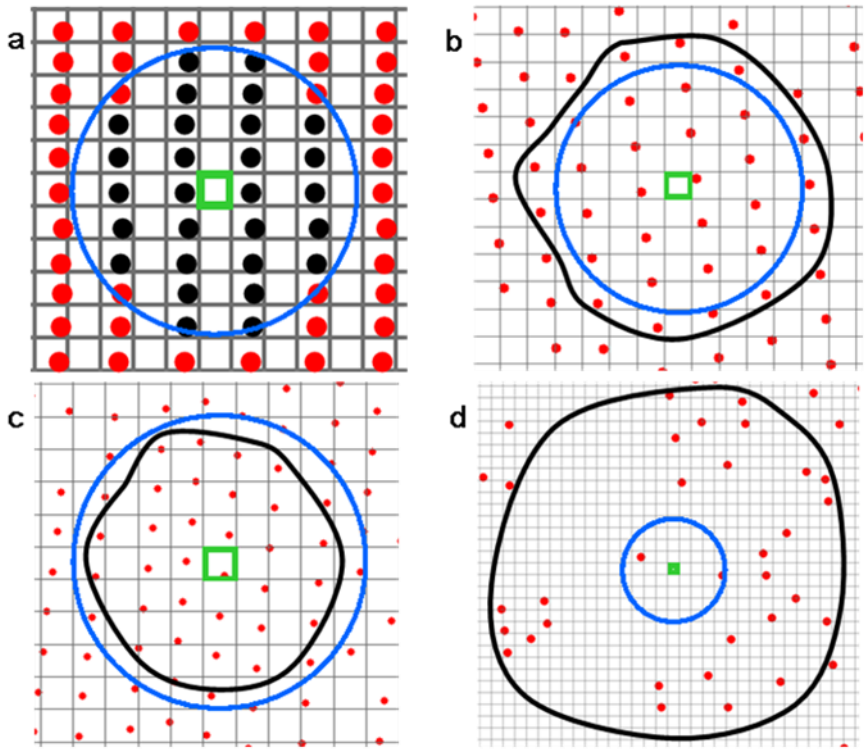

Figure 3.3 Graphic representation of a) theoretical ground return point spacing and resulting 2 m search radius (blue circle) of target cell (green square), b) average point density (~1 m-1) with 30 point search radius (included in black line), c) high point density (> 5 m-1), and d) low point density (< 0.5 m-1), all grid lines represent 0.5 m intervals.

3.6. DEM uncertainty and artefacts

Uncertainty within LiDAR DEMs is a function of point density and the interpolation method used to generate continuous surfaces (Liu, 2008; Bater & Coops, 2009). Point density is reduced in thick vegetation as tree canopies intercept a greater proportion of the laser beam energy. This effect is accentuated with higher off-nadir scan angles as the beam must pass through a relatively larger proportion of canopy to reach the ground (Jensen, 2007; Bater & Coops, 2009). In addition, PRR and the laser pulse energy density are also significant factors that determine the ability of LiDAR to penetrate forest canopies (Hopkinson, 2006).

In certain cases it became apparent that the DEM generated for this study contained a range of spurious features primarily a result of LiDAR data collection inaccuracies and the exacting nature of the DEM interpolation algorithm. Striping and step artefacts were the most obvious and most detrimental to the DEM image enhancements carried out. Striping was most apparent on surfaces inclined away from the flight path and where points were collected with large scan angles (i.e. limits of the swath width) (Figure 3.4). The striping effect is probably due to a slight scan mirror alignment error that is accentuated with large laser beam to surface incidence angles (i.e. large off-nadir scan angles and terrain surface inclined away from the flight path). The wavelength of the striping is ~2 m and coincides with every 5^{th} swath path. The DEM profile in Figure 3.4e shows that the amplitude of the striping is ~0.2 m, equivalent to the approximate error in the LiDAR systems vertical precision (IGI mbH, 2009). The orientation of the striping changes between flightlines since they remain perpendicular to each flight path.

Scarp or step artefacts are laterally curving features observed at abrupt boundaries between points collected from different flightlines (Figure 3.5). Scarp artefacts are characterised by vertical steps (> 0.5 m high) in the DEM and are most likely due to poor DGPS or IMU corrections during point cloud post-processing (Blakely *et al.*, 2004). Mound artefacts are also seen in Figure 3.5; these appear to coincide with points collected from one (northern) flightline (red points) in an area where the majority of point are collected from an adjacent flightline (green points). This suggests that mounds are caused by similar errors in point cloud post-processing that result in scarp artefacts.

The effects of the LiDAR point data artefacts mentioned above have been reduced using low pass filtering (see Figure 3.4b and Figure 3.5b). A low pass filter or smoothing filter eliminates high frequency features within digital images by calculating the average of the grid cells surrounding the target cell. In both cases a filter kernel size of 21 x 21 (i.e. 10.5 m x 10.5 m) has been used.

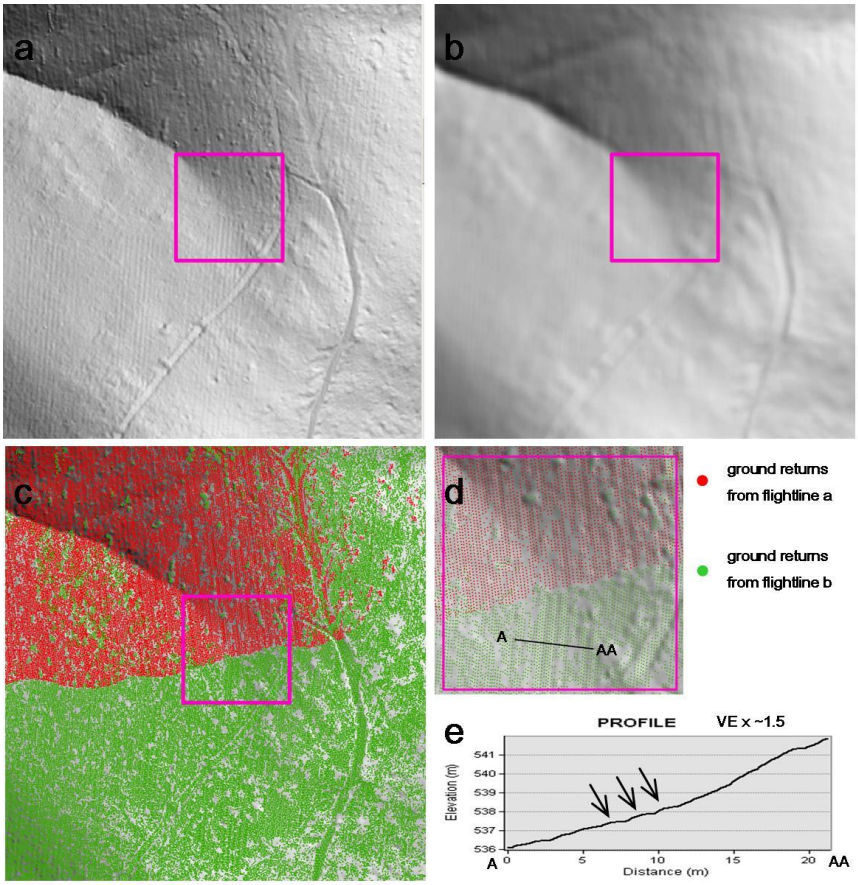

Figure 3.4 DEM striping artefacts highlighted in purple square, a) 0.5 m grid DEM interpolated using Spline, b) low pass filtered (smoothed) 0.5 m DEM using 21 x 21 grid kernel (i.e. 10.5 m x 10.5 m), c) overlayed ground returns showing points from two distinct flightlines, d) zoom view showing location of the profile in e) arrows represent crests of stripe artefacts (DEM enhanced with a sun angle filter, NE azimuth and 45° angle)

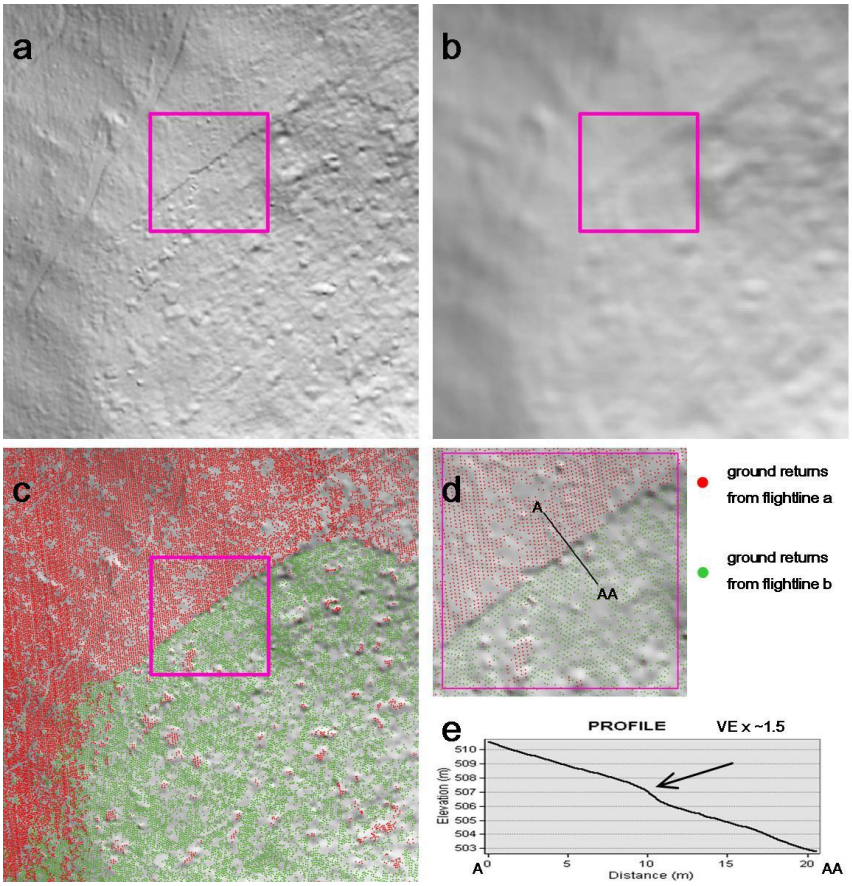

Figure 3.5 DEM scarp artefacts highlighted in purple square, a) 0.5 m grid DEM interpolated using Spline, b) low pass filtered (smoothed) 0.5 m DEM using 21 x 21 grid kernel (i.e. 10.5 m x 10.5 m), c) overlayed ground returns showing points from two distinct flightlines, d) zoom view showing location of the profile in e) arrow represents location of scarp artefact (DEM enhanced with a sun angle filter, NE azimuth and 45° angle)

3.7. Closing Remarks

In this chapter a brief description has been given of LiDAR remote sensing system technology, data acquisition methods and point cloud post-processing steps. In addition, LiDAR system parameters for the data used in this project have been presented along with a summary of DEM interpolation methods, touching on the important and relevant points concerning the theory behind minimum curvature spline with Tension interpolators. Although LiDAR has the capacity to produce highly precise elevation data it is still prone to inaccuracies. The main artefacts present in the DEMs such as striping, scarps and mounds have been highlighted descriptively and graphically. These artefacts seem to be most prevalent at larger scan angles and steeper terrains, and are produced by slight errors in post-processing steps, positioning of the aircraft and its attitude between different flightlines.

4. Lineament enhancement, extraction and classification

Lineament identification has, in the recent past, been seen within the geological fraternity as a quasi-science and as a result viewed with some scepticism (Rice, 1997). This is because of the heavy reliance on subjective identification and extraction of lineaments, often manually performed by an expert observer (Wladis, 1999; Argialas & Mavrantza, 2004). As Raghavan, Wadatsumi & Masumoto (1993) and Wladis (1999) point out; manual methods have the potential to introduce bias from the observer, thus generating unreproducible results based on the qualitative perception of features under investigation. Therefore, automated techniques aim to provide objectively generated results for the quantitative analysis of landforms and robust assessment of the relationship between the landscape and underlying geological structures (Raghavan, Wadatsumi & Masumoto, 1993; Wladis, 1999).

Many lineament extraction methods integrate manual (subjective) and automated (objective) techniques (Sarp & Toprak, 2007). Initially, a series of image enhancement processes are used to accentuate the features of interest, followed by extraction or selection of these features. In general, there are several steps involved in lineament studies once the input datasets have been prepared and processed (Koike, Nagano & Ohmi, 1995; Wladis, 1999; Haugerud *et al.*, 2003; Pluijm & Marshak, 2004; Ekneligoda & Henkel, 2006). They include:

- the enhancement of features within a given dataset
- the extraction of target features (manually or automatically) using defined observational criteria or numeric thresholds
- association of spatial properties to extracted features for classification
- result validation and interpretation of lineament geoscientific meaning, often involving the integration of other relevant datasets (i.e. field data and geophysics) in a GIS environment

This chapter deals with the theory behind the first three steps described above while focussing on automated methods. Object-Based Image Analysis (OBIA) is a semi-automated method that incorporates the steps outlined in this chapter using a set of rules for the classification of extracted features. For example, during OBIA target pixels are identified, features extracted and classified based on the pixel values and the values of the neighbouring cells (Argialas & Mavrantza, 2004; Mavrantza & Argialas, 2006; Rutzinger *et al.*, 2007).

4.1. Lineament enhancement

Several different methods with varying degrees of complexity have been proposed for lineament enhancement and identification from gridded images. In general, defining surface discontinuities utilises edge detection image based processing algorithms. Most edge detection algorithms use differentiation to detect rapid changes in a surface property using convolution filter kernels of varying sizes. The simplest edge detectors involve using directional filters (i.e. hillshade and Sobel Operator) that highlight discontinuities perpendicular to the filtering direction. Once features are enhanced within hillshade images, manual selection and digitisation of lineaments based on established criteria usually follows (Blakely *et al.*, 2004; Maukisch *et al.*, 2007; Nyborg, Berglund & Triumf, 2007). More complex edge detection filters use non-directional filters (i.e. Laplacian Operator or 2nd derivatives) for the enhancement of multi-directional features in potential field datasets (i.e. magnetics and gravity) (Wladis, 1999; Eaton & Vasudevan, 2004) and satellite imagery (Karnieli *et al.*, 1996). These methods are usually accompanied with some form of line extraction algorithm such as the Hough Transform.

Morphological filters are akin to edge detection methods and use differential convolution filter kernels to calculate the geometry of a surface (i.e. slope, aspect, and curvature) (Wladis, 1999; Argialas & Mavrantza, 2004). The most important derived surface for lineament extraction is surface curvature, or the 2nd derivative of a surface (Wood, 1996; Maukisch *et al.*, 2007). Morphological filters have the advantage of highlighting features of maximum (ridges) and minimum (channels) curvature (linear slope discontinuities) (Wallace, Morris & Howarth, 2006; Rutzinger *et al.*, 2007) without the bias seen when using directional edge detection filters. Morphological filters incorporate the capacity to characterise and classify surface features based on the derived values within neighbouring pixels.

Several experimental lineament extraction methods have been proposed that group surfaces with homogeneous slope and aspect and identify region boundaries (Maukisch *et al.*, 2007). More complex algorithms involve the geometric analysis of the original point cloud dataset rather than the enhancement of interpolated grid surfaces (Filin, 2004; Ronacella & Forlani, 2005; Filin & Pfeifer, 2006).

4.1.1. Edge detection

Several methods are available for the identification of edges in digital geophysical and satellite imagery datasets that can be applied to the extraction of topographic lineaments. Edge detection methods identify adjacent pixels in a digital image with contrasting values via differentiation. Thus edges are associated with rapid changes in a surface, accentuating the high frequency

components of an image. Edge detectors can be implemented at a variety of scales defined by the size of the kernel window used to traverse the image (Koike, Nagano & Ohmi, 1995; Argialas & Mavrantza, 2004). The processing of data with edge detectors usually involves three steps: averaging the surface to reduce noise; edge identification via differentiation; and linking pixels that share edge boundaries. The final step involves the application of line linking algorithms such as the Hough Transform or Skeletonisation (Argialas & Mavrantza, 2004; Eaton & Vasudevan, 2004; Cooper, 2006).

The basic principle of directional filters is based around calculating the horizontal 1st (partial) derivative of a surface in a pre-defined direction. Resulting surfaces have directional bias, where surface discontinuities perpendicular to the derivative filter direction are enhanced preferentially to those parallel to the filter direction (Raghavan, Wadatsumi & Masumoto, 1993). Changes to the illumination azimuth (direction), angle and vertical exaggeration have the ability to highlight different features within images. The most robust methods for directional edge detection are obtained using multiple illumination azimuths (e.g. the eight orthogonal directions of the compass rose) (Rice, 1997; Blakely *et al.*, 2004; GahGah *et al.*, 2007).

Hillshade enhancement is commonly used for the visual identification, manual extraction and digitisation of surface features. However, Raghavan, Wadatsumi & Masumoto (1993) used a Directional Segment Detection Algorithm (DSDA) to automatically detect linear features in DEMs. The DSDA defines features by contrasts in brightness levels in a user defined direction. Hillshade is most often used to enhance the original image, although it is feasible to use this method on any image or its derivatives (i.e. slope or curvature).

The Sobel Operator is analogous to the hillshade filter and has been used for the enhancement of edge features and lineaments in potential field datasets (Karnieli *et al.*, 1996). In contrast, Laplacian Operators are non-linear (non-directional) filters. Wladis (1999) used a Laplacian Operator based 2nd vertical derivative filter with a weighted edge detection kernel, originally developed for the enhancement of potential field geophysical data. Appropriate weights were selected on the basis of the 2D frequency response of the surface in question.

4.1.2. Morphological filters

Five terrain parameters can be defined for any 2D continuous surface: elevation; slope and aspect; profile and plan curvature (Evans, 1979 in Wood, 1996 p. 82). These parameter groups correspond to the 0, 1st and 2nd order partial differentials respectively, where the latter functions have components in the XY and orthogonal planes (Wood, 1996). The most important derivative of a surface for the detection of lineaments is curvature (2nd derivative). Curvature defines the

location of slope discontinuities or edges (analogous to edge detection algorithms) on a surface (Wallace, Morris & Howarth, 2006; Rutzinger *et al.*, 2007). In addition, the polarity of the discontinuity is implied with the sign of the curvature values calculated. For example, ridges (convex) are positive and channels (concave) are negative slope discontinuities (Maukisch *et al.*, 2007).

Spatial domain convolution filters can be used to approximate a surface by fitting a bivariate quadratic function of the form (Evans, 1979 in Wood, 1996 p. 83):

$$z = ax^2 + by^2 + cxy + dx + ey + f \qquad (4.1)$$

Using convolution filters of varying sizes in the spatial domain and considering the partial differential equations of the general quadratic forms (i.e. elliptic, parabolic and hyperbolic, Figure 4.1), it is possible to define the morphological properties of a surface, thus describing its geometry at the scale of the filter kernel (Wood, 1996; Wallace, Morris & Howarth, 2006; Rutzinger *et al.*, 2007). An advantage with defining surface parameters using the method described above is that inherent directional bias is eliminated. There are limitations to using quadratic surfaces to approximate the geometry of a landscape. Limitations result from the process of minimising residuals (often with least squares fitting) to "best-fit" the calculated quadratic surface to kernel values. However, it is actually the value within the central cell of the kernel that is used to define the calculated surface. Therefore, statistical best-fit determination of the surface coefficients may not necessarily provide appropriate values for identifying surface parameters (Wood, 1996).

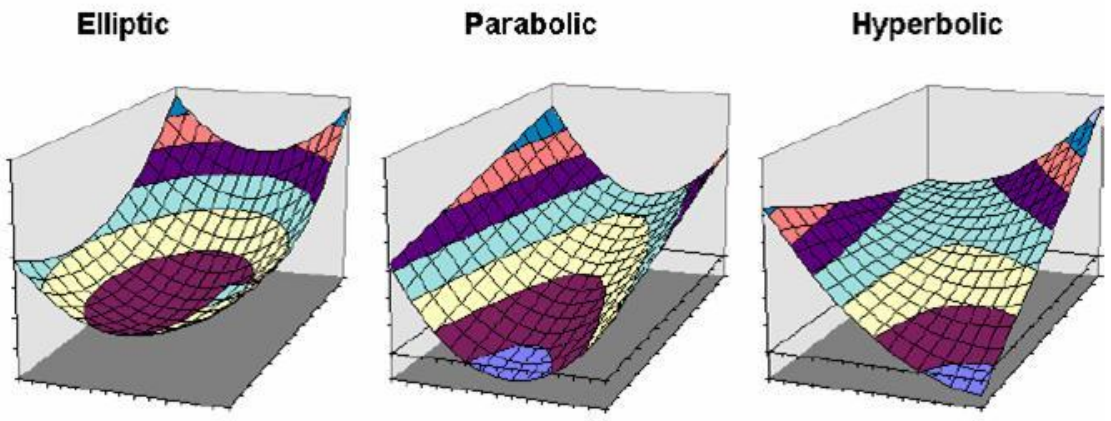

Figure 4.1 General quadratic forms of the partial differential equations of a surface, adapted from Wood (1996)

4.1.3. Point cloud analysis

Recently, algorithms have been developed that involve the geometric analysis of point cloud datasets rather than using enhanced continuous (interpolated) surfaces. Most point cloud geometry analysis algorithms have been developed for the extraction of buildings in urban environments and the classification of points (Filin & Pfeifer, 2006; Chen *et al.*, 2008). Whereas, Ronacella & Forlani (2005) applied these principles to modelling geological outcrops using data obtained from Terrestrial Laser Scanners (TLS). Improvements in these algorithms have been possible with an increase in computing power.

The general principle behind the geometric analysis of point clouds is conceptually simple. Each point is compared with its neighbours and planar surfaces between points are calculated. Thresholds are used to form homogenous groups representing clusters of points that lie on a planar surface. Surfaces are modelled conforming to the respective geometries of homogeneous point clusters (Filin, 2004; Ronacella & Forlani, 2005; Chen *et al.*, 2008). This method preserves the original feature based data structure. Surface accuracy approximation is often conducted by calculating the residuals between points and associated surfaces (Ronacella & Forlani, 2005; Chen *et al.*, 2008). However, the computational complexity for extracting surfaces from point clouds is apparent with Filin's (2004) algorithm defining seven dimensional space for the orientation of a plane that point clusters lie on. Ronacella & Forlani (2005) constructed multi-resolutional pyramids for the generation of planes at every scale of observation using topological constraints. Constraints were based on thresholds that defined limits for the connectivity of points, curvature of the surface and its shape.

4.2. Lineament (feature) extraction

Once the location of target features have been enhanced and identified within an image, the next step is to extract the feature in question and assign attributes or unique values. Conversion to vector data formats (i.e. lines) is an important step as it allows for the association of spatial attributes to extracted features (Maukisch *et al.*, 2007). Conversion often involves selecting pixels that represent a surface discontinuity based on a numeric threshold. Then contiguous pixels representing a single feature are linked using methods such as the Hough Transform, Skeletonisation and Segment Tracing Algorithm (Argialas & Mavrantza, 2004). Morphological filters employ a rule based OBIA to identify target features and classify the surface into six feature classes. A feature extraction algorithm traverses the classified image and links cells based on surface network topological relationships (Wood, 1996).

4.2.1. Hough Transform

Remote sensing image to line conversion algorithms have commonly utilised the Hough Transform. The Hough Transform detects boundaries in gradient-intercept space (i.e. pixels that are associated with edges within the surface) and then searches adjacent pixels for incorporation into the feature. If a large enough number of adjacent edge cells align with a common orientation, then it is probable that the edges correspond to a linear feature (Karnieli *et al.*, 1996; Cooper, 2006). Once the orientation of the edge feature has been determined a line is drawn within the data scene. Hough Transforms are of limited benefit because they are computationally expensive (becoming less of an issue with the improvement in computing power) and extracted lines are extrapolated across the entire image. Therefore, the resulting orientation of the lineament (extracted feature) takes precedence over its spatial distribution (Wladis, 1999).

4.2.2. Skeletonisation

Skeletonisation was originally developed for the extraction of seismic reflectors. As a result vertical and sub-vertical features were not initially recognised (Eaton & Vasudevan, 2004). Skeletonisation is a rule based pattern-recognition method that can be applied to band-limited gridded data for the construction of a line and subsequent association of attributes. This method has been used to identify cyclic patterns of peak positive and negative amplitudes within aeromagnetic data. Eaton & Vasudevan (2004) developed a Skeletonisation process that detects features in all azimuth directions for the extraction of edges in aeromagnetic data. Attributes that can be associated with extracted lines include the amplitude of the feature, its average azimuth (orientation), length and mean of the calculated residuals.

4.2.3. Segment Tracing Algorithm

Koike, Nagano & Ohmi (1995) developed the Segment Tracing Algorithm (STA), which is a non-filtering directionally variable approach to identifying and extracting line elements from grey level images. STA utilises the sun illumination effect of passive multispectral satellite imagery to identify and simultaneously classify topographic highs (ridges) and lows (valleys). The STA detects the orientation of a feature (valley or ridge) by examining the local deviation of grey levels and establishes if the feature is a line by differentiating grey levels perpendicular to the target feature mean orientation. It then determines if the target pixels are linearly continuous. The classification of ridges and valleys is established from the variation in grey levels surrounding the target feature. The average direction of complex (curvilinear) lineaments is determined using a least squares approach.

4.2.4. Surface morphology

Morphological feature extraction algorithms are based on topological rules and attempt to connect cells that meet particular criteria for the generation of surface networks (Wood, 1996). Six morphometric feature types that are characteristic of any surface, not necessarily geomorphic, are planes, channels, ridges, passes, peaks and pits (Figure 4.2). These can be described in terms of the 2nd partial derivatives of the three orthogonal components (x, y and z). Classification of discrete morphometric features can be obtained by passing a local kernel over a DEM and comparing the relationship between the target cell (central cell) and it neighbours (Table 4.1) (Wood, 1996).

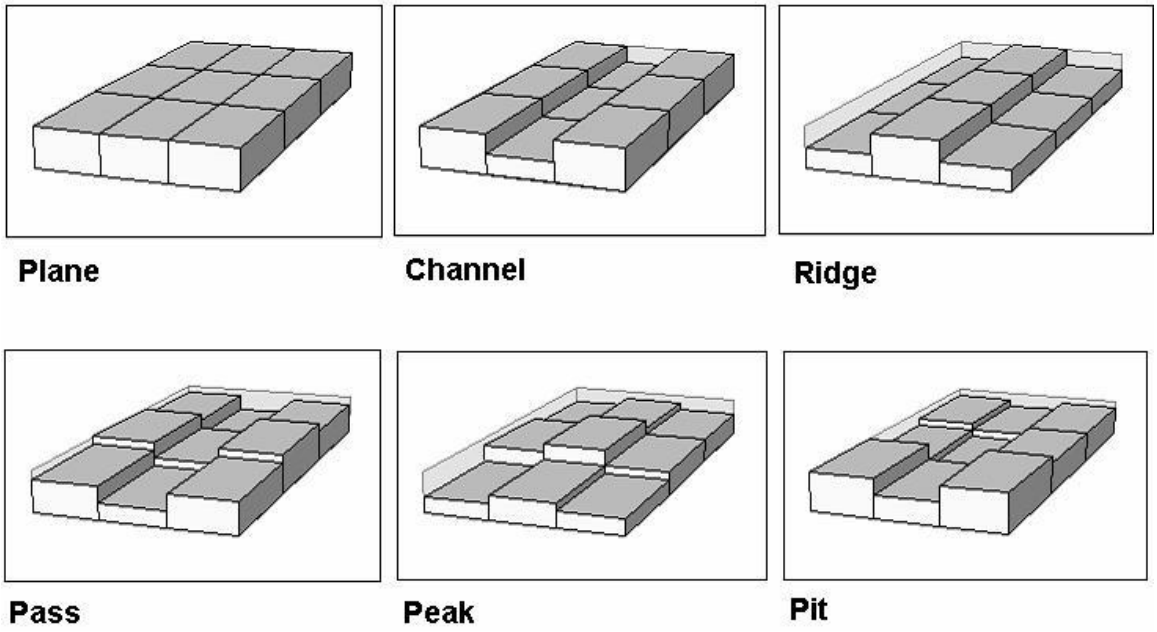

Figure 4.2 The six morphometric feature types of a surface (Wood, 1996)

The morphometric classification procedure generates an image where each grid cell is assigned an attribute that represents the morphological feature determined by the algorithm. A network extraction algorithm traverses the classified image and links ridge and valley networks based on a series of topological constraints (Figure 4.3). Peaks, pits and passes are represented by points and ridges and channels are represented by lines connecting points, such that ridges connect peaks and passes, and channels connect passes and pits (Wood, 2000).

Table 4.1 Morphometric feature types as described by 2nd partial derivative topological relationships (Wood, 1996)

Feature name	Derivative expression	Description
Peak	$\frac{\delta^2 z}{\delta x^2} > 0, \frac{\delta^2 z}{\delta y^2} > 0$	Point that lies on a local convexity in all directions (all neighbours lower).
Ridge	$\frac{\delta^2 z}{\delta x^2} > 0, \frac{\delta^2 z}{\delta y^2} = 0$	Point that lies on a local convexity that is orthogonal to a line with no convexity/concavity.
Pass	$\frac{\delta^2 z}{\delta x^2} > 0, \frac{\delta^2 z}{\delta y^2} < 0$	Point that lies on a local convexity that is orthogonal to a local concavity.
Plane	$\frac{\delta^2 z}{\delta x^2} = 0, \frac{\delta^2 z}{\delta y^2} = 0$	Points that do not lie on any surface concavity or convexity.
Channel	$\frac{\delta^2 z}{\delta x^2} < 0, \frac{\delta^2 z}{\delta y^2} = 0$	Point that lies in a local concavity that is orthogonal to a line with no concavity/convexity.
Pit	$\frac{\delta^2 z}{\delta x^2} < 0, \frac{\delta^2 z}{\delta y^2} < 0$	Point that lies in a local concavity in all directions (all neighbours higher).

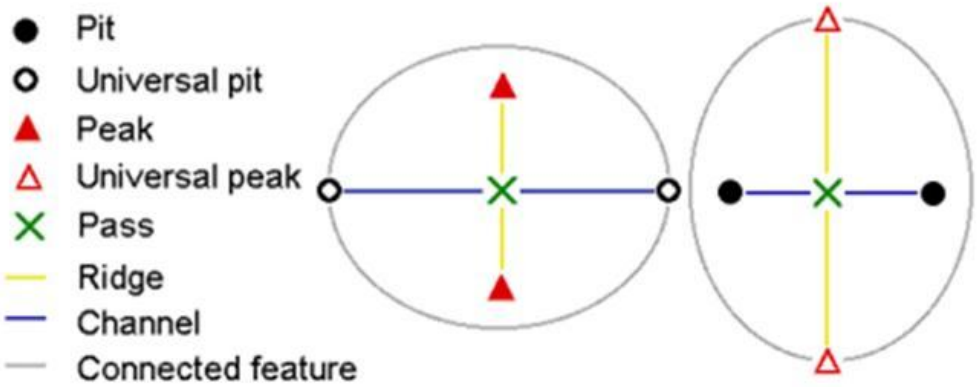

Figure 4.3 Using topological rules to generate ridge and channel networks by linking peaks, pits and passes (Wood, 2000)

4.3. Feature spatial properties and classification

Determining the spatial properties of extracted features is an important step that allows for the quantitative assessment and analysis of lineaments (Eaton & Vasudevan, 2004). Attributes can be assigned to features based on their inherent spatial properties such as location, polarity, orientation, length and scale of observation. Other attributes can be included such as, density per

unit area and clustering of features with similar characteristics (Clark & Wilson, 1994). The scale of the feature in question is an important attribute. It is usually determined by the resolution of the original gridded image and the size of the filter kernel used to either enhance or extract the feature. 3D attributes can be calculated using knowledge of the features 3D spatial location and distribution.

The most common approach for assigning attributes to features is via object-orientated classification (Mavrantza & Argialas, 2006; Rutzinger *et al.*, 2007). This approach utilises a knowledge based hierarchical division of features, determined by their spatial attributes and progressively sub-divides features using a series of user defined rules. These fuzzy classification rules can be applied to assist in the automated determination of class membership (Mavrantza & Argialas, 2006).

4.3.1. Scale

The scale of a surface feature is a useful diagnostic property (Wood, 1996). Scale is determined by the product of the convolution filter kernel size used to enhance target features in the spatial domain and the resolution of the image being examined. The resolution of the image is determined by the grid cell size. Higher resolution images provide greater detail and definition of the surface being imaged and therefore allow for identification of local scale discontinuities and thus smaller surface features. However, as the scale of observation decreases the enhancement of surface noise increases (Rutzinger *et al.*, 2007).

In addition to the morphometric measures of topography, fractal dimension D can be calculated with respect to a given scale of observation (Koike, Nagano & Ohmi, 1995; Wood, 1996; Wallace, Morris & Howarth, 2006). D in essence, provides a measure of feature complexity (Gloaguen, Marpu & Niemeyer, 2007) and can be used to describe the geometry of natural phenomena (Sun *et al.*, 2006). The non-integer fractal dimension between 2 and 3 represents the ruggedness or roughness of a statistically self-similar surface (Koike, Nagano & Ohmi, 1995; Wood, 1996; Wallace, Morris & Howarth, 2006).

4.3.2. 2D spatial attributes

The most obvious 2D spatial attributes of a linear feature are location, orientation and length (Clark & Wilson, 1994). The location of a line can be reduced to a mean position in 2D (i.e. x and y coordinates). A perfectly straight lines' mean position can be generated by averaging the minimum and maximum x and y coordinates of the end nodes. Line azimuth direction can be determined by taking the end nodes and calculating the angle θ with respect to grid north (this requires an additional quadrant adjustment) (Ekneligoda & Henkel, 2006). If the line is curvilinear,

the mean orientation of the segments that the line is composed of can be calculated (ESRI, 2008). In addition, the circular variance of a curvilinear line with respect to a straight line is a useful feature characteristic (Rutzinger *et al.*, 2007). Length is simply the linear distance between start and end vertices of the line or the sum of the segments in the case of curvilinear features (Ekneligoda & Henkel, 2006).

Feature density per unit area and clustering is obtained by utilising the location of a feature reduced to a single point. Lineament density can be expressed as the number of features per unit area or the total length of features per unit area (Ekneligoda & Henkel, 2006). The establishment of a sampling area is required to calculate feature density (Sarp & Toprak, 2007). Clustering on the other hand, identifies groups of features that share homogeneous characteristics (e.g. orientation or length) and is typically expressed statistically as the degree of variation between an individual feature and neighbouring features (Clark & Wilson, 1994).

4.3.3. 3D spatial attributes

The methods described above, determine 2D spatial attributes for line features. However, because geological structures have true 3D geometric characteristics it is theoretically feasible to extract 3D spatial attributes based on a feature's 3D spatial distribution (Fernández, 2005; Ronacella & Forlani, 2005). Fernández (2005) proposes two surface fitting algorithms that elaborate on the traditional three-point problem and utilise multiple 3D coordinates representing a feature to estimate a best-fit plane. Two assumptions are made in order to generate planes: the surface is assumed to be planar and the points selected for the best-fit algorithm are representative of the plane. A different approach conducted by Ronacella & Forlani (2005) utilised the 3D geometry of the original point cloud data to extract planar surfaces (i.e. scanned outcrops).

In both cases described above, several 3D geometric attributes can be assigned to a feature. The average 3D coordinates of the feature. The coefficients of the equation representing the best-fit plane determined from the feature in question. A measure of the degree-of-fit of the plane to the 3D points used to determine the surface (e.g. RMSE and co-planarity), and the reliability of the measurement (e.g. co-linearity) (Fernández, 2005; Fernández *et al.*, 2009). The vector normal to the plane generated from either method described above can be used to calculate dip (slope as measured from the horizontal axis) and dip direction (azimuth of the maximum slope direction). These angular measurements define the orientation of a planar surface in 3D (Fernández, 2005; Ronacella & Forlani, 2005).

5. Study area and northeast Tasmanian geology

This chapter provides a brief summary of the geology of northeast Tasmania. Specific attention is given to the stratigraphy, structures and mineralisation present within the study area.

5.1. Regional setting

Northeast Tasmania is loosely defined as the area east of the Tamar Valley and north of the Esk Highway. The geology of northeast Tasmania (Figure 5.1) is dominated by early-mid Palaeozoic deep-marine turbidites, known regionally as the Mathinna Group (Powell *et al.*, 1993). The Mathinna Group was intruded by I and S type granites during the Middle to Late Devonian (Goscombe, McClenaghan & Everard, 1992; Reed, 2001b; Reed, 2001a). Pre-Carboniferous rocks are unconformably overlain by the flat lying sediments of the middle Palaeozoic Parmeener Supergroup. The Parmeener Supergroup has been extensively intruded by dolerite sheets during the Jurassic, remnants of which form most topographic highs in the region (Turner & Calver, 1987). Tertiary basaltic lavas are predominantly found in topographic lows as are Quaternary alluvial sediments. Dolerite talus, glacial; and periglacial deposits mantle the flanks of higher peaks (McClenaghan & Baillie, 1975).

Northeast Tasmania has historically been one of the largest gold producing areas in Tasmania and therefore is of significant economic importance. The majority of gold in this area has originated from a NNW-SSE trending zone between the Scottsdale and Blue Tier Batholiths, called the Alberton – Mangana Lineament (Taheri & Findlay, 1992; Keele, 1994). The abandoned New Golden Gate Mine (NGGM), located ~2 km south of Mathinna was in its time the largest producing gold mine in the area. However, most gold mining activities south of Mathinna were small alluvial and near surface workings that operated around the turn of the 20th Century (Taheri & Findlay, 1992; Reed, 2004).

5.1.1. Stratigraphy

Mathinna Group (Ordovician – Devonian)

The Mathinna Group turbidites are comprised of a monotonous sequence of interbedded, commonly graded quartz sandstones (minor psammites) and pelites. These sediments are thought to have been deposited during the Ordovician to Devonian, although biostratigraphic evidence is rare especially east of the Scottsdale Batholith (Powell *et al.*, 1993; Seymour & Calver, 1995; Reed, 2004). The total thickness of Mathinna Group sediments is suspected to be ~6-7 km but the lack of good stratigraphic markers means that the overall thickness of the package is

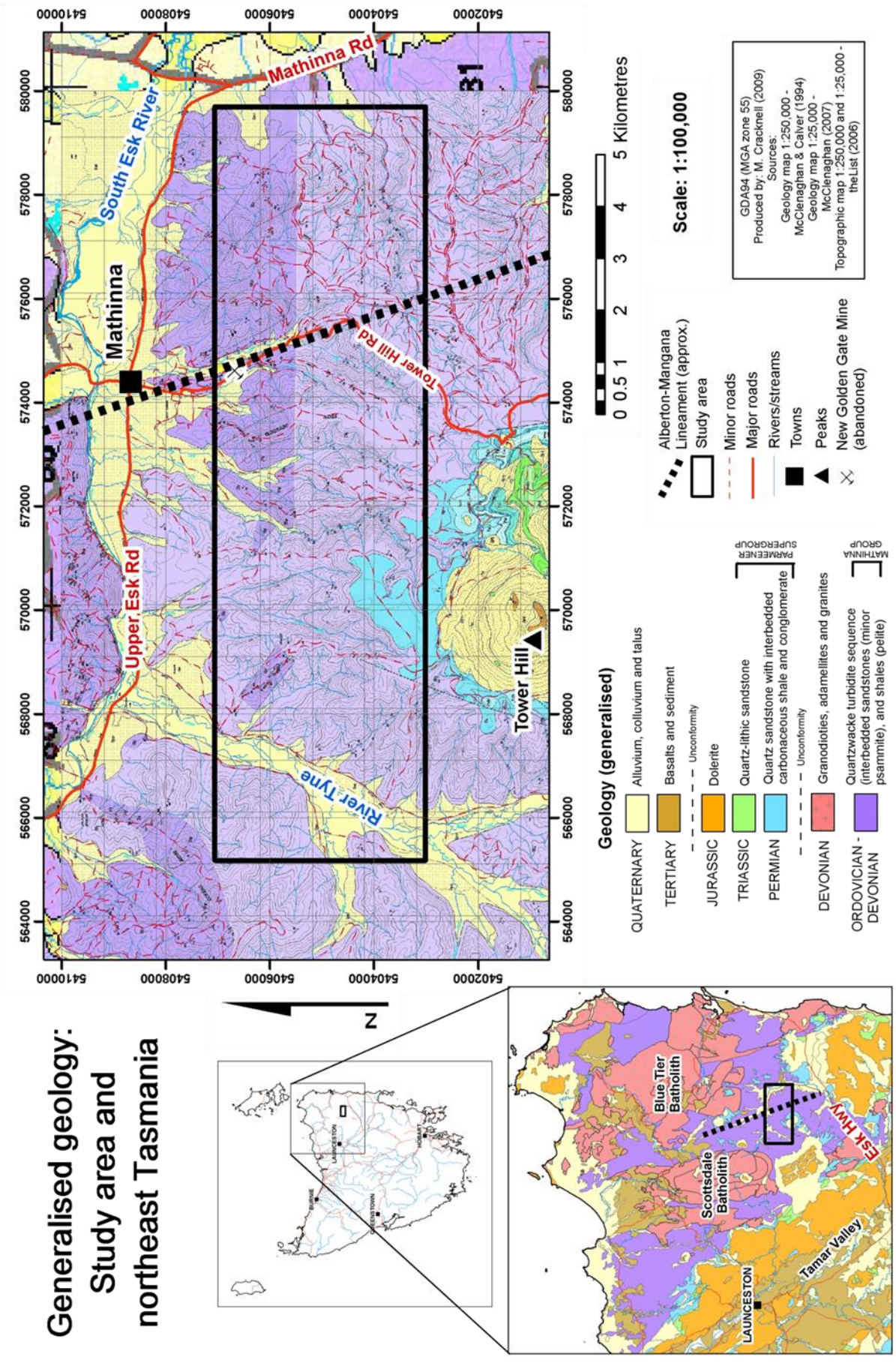

Figure 5.1 Generalised geology of the study area and northeast Tasmania

poorly constrained (Seymour & Calver, 1995; Seymour, Green & Calver, 2006). Regionally the Mathinna Group stratigraphy is interpreted to young from west to east and consists of the:

- Stony Head Sandstone (quarztose turbiditic sandstone)
- Turquoise Bluff Slate (black pelite)
- Bellingham Formation (increasingly sand dominated sequence of quarztose turbiditic sandstones)
- and Sidling Sandstone (feldspatholithic turbiditic sandstones) (Powell *et al.*, 1993)

Powell *et al.* (1993) originally proposed a conformable stratigraphy for the Mathinna Group. However, Reed (2001a) notes that the Stony Head Sandstone and Turquoise Bluff Slate have experienced a deformation event not seen in the overlying Bellingham Formation and Sidling Sandstone east of the Scottsdale Batholith. From this evidence, Reed (2001a) suggests that the boundary between the Turquoise Bluff Slate and Bellingham Formation is a depositional hiatus and that the Mathinna Group should be given Supergroup status and divided into two separate groups at this boundary. It is not the aim of this project to reconcile stratigraphic boundaries; therefore no further discussion of the specifics of this issue will be considered.

Granitoid intrusions (Devonian)

Devonian granitoid intrusions are found throughout northeast Tasmania. These granitoids can be divided into two general granitic masses: in the west the Scottsdale Batholith and the east the Blue Tier Batholith (Patison *et al.*, 2001) (Figure 5.1 p. 36). Granitoid emplacement is thought to have occurred during the Late to Middle Devonian (Goscombe, McClenaghan & Everard, 1992). These batholiths are variably composed of granodiorite (I-Type), biotite granite/adamellite (S-Type) and alkali-feldspar granite (McClenaghan, 1985 in Seymour & Calver, 1995; Reed, 2004). Regional gravity modelling has shown these granitoid bodies to be part of a N-NNW trending mass that underlies much of eastern Tasmania (Leaman and Richardson, 1992 in Seymour & Calver, 1995; Reed, 2004).

Regional metamorphism of the Mathinna Group is widespread but not above sub-greenschist facies (McClenaghan, Turner & Everard, 1992; Patison *et al.*, 2001). A penetrative often slaty cleavage has developed predominantly within pelitic units. Narrow metamorphic aureoles are apparent proximal to granitoid bodies, forming minor psammites and pelites from contact effects within the Mathinna Group sediments (Goscombe, McClenaghan & Everard, 1992; Patison *et al.*, 2001).

Post-Carboniferous

Permo-Triassic sediments of the Parmeener Supergroup unconformably overlie both the Devonian granitoids and folded Mathinna Group sediments (Taheri & Findlay, 1992; Richardson & Roach, 1994; Reed, 2004). Deposition of these sediments has occurred from the Late Carboniferous to Late Triassic (Goscombe, McClenaghan & Everard, 1992). The Parmeener Supergroup sediments in northeast Tasmania are predominantly composed of a flat lying paralic and marine sedimentary facies disconformably overlain by non-marine (i.e. deltaic and fluvial) sediments. The lower sequence is comprised of quartz sandstones and conglomerates, laminated mudstones and limestones, and minor coal measures. The upper sequence is predominantly comprised of quartz-arenites (Turner & Calver, 1987). In some areas the Quaternary erosional surface has only recently exposed the underlying basement rocks (i.e. pre-Permian surface) (McClenaghan & Baillie, 1975).

Dolerite sheets extensively intrude the Upper Parmeener Supergroup sediments across northeast Tasmania often forming topographic highs (McClenaghan & Baillie, 1975; Turner & Calver, 1987). Basaltic lavas have extruded across a pre-Tertiary erosional surface. Quaternary alluvial sediments fill topographic lows, and colluvium and talus deposits (predominantly dolerite derived) mantle higher slopes (McClenaghan & Baillie, 1975; Taheri & Findlay, 1992).

5.1.2. Deformation history and structures

Powell (1992), Patison *et al.* (2001) and Reed (2004) propose broadly similar regional deformation models for the rocks of north eastern Tasmania although their models differ in detail. Overall deformation intensity/complexity decreases from west to east. Nevertheless, it is difficult to constrain regional deformation models due to the lack of stratigraphic markers within the Mathinna Group.

Powell (1992) proposes a three phase deformation history; D_1 and D_2 are part of the Middle Devonian Tabberabberan Orogeny, interpreted to occur prior to and after granitoid emplacement respectively. D_3 is characterised by Mid-Carboniferous (?) overprinting mega-kinks. Patison *et al.* (2001) suggest that there have only been two deformations (Powell's (1992) D_1 and D_2) and does not mention the mega-kinking event. In contrast, Reed (2001a) and Reed (2004) propose a deformation model that includes three events in which D_1 occurs during the Silurian Benambran Orogeny and affects the Mathinna Group in the western extremity of the terrane (i.e. west of the Scottsdale Batholith). Reed's (2004) D_2 and D_3 are analogous to Powell's (1992) and Patison *et al.'s* (2001) D_1 and D_2 events. The presence of mega-kinking is described by Goscombe & Findlay (1989), Goscombe, McClenaghan & Everard (1992) and Goscombe *et al.* (1994) and has been based on abrupt changes in S_1 cleavage trends at variety of scales. Similar structural features have

been identified within the Lachlan Fold Belt of southeast Australia (Goscombe & Findlay, 1989). However, Reed (2001b) and Reed (2004) suggest the timing of the mega-kinking is poorly constrained and that Goscombe & Findlay (1989), Goscombe, McClenaghan & Everard (1992) and Goscombe *et al.* (1994) did not differentiate between S_2 (i.e. Powell's (1992) and Patison *et al.'s* (2001) S_1) and S_3 (i.e. Powell's (1992) and Patison *et al.'s* (2001) S_2) cleavages. Consequently, Reed (2001b) and Reed (2004) propose that the mega-kinking event occurred during late D_2 and prior to D_3 due to the fact that variations in the orientation of S_2 are not mirrored by variations in S_3.

Regardless of the specifics of the actual deformation history of northeast Tasmania, Powell (1992), Patison *et al.* (2001) and Reed (2004) agree that the deformations associated with the Tabberabberan Orogeny, either Powell's (1992) and Patison *et al.'s* (2001) D_1 and D_2 or (Reed's, (2004) D_2 and D_3 have similar characteristics and structural trends. Only these major events are considered to have affected the Mathinna Group within the study area (i.e. east of the Scottsdale Batholith). The first deformation (henceforth called D_1), is interpreted as a compressional event and was directed toward the NE. D_1 occurs prior to the emplacement of the Middle to Late Devonian granitoids. This event generated NE verging folds, axial planar cleavage and steeply dipping NE directed thrust faults. Fold axial planes trend NNW and dip steeply to the SW. Fold geometry is commonly upright, open to tight concentric to sub-concentric chevron style. Faults are common in the F_1 hinge zones of sandstone beds. The second regional deformation event (henceforth called D_2), is interpreted to postdate granitoid emplacement and was directed toward the WSW-SW. D_2 has refolded D_1 folds and displays SW verging fold geometries. SW directed thrusting with NE side up, showing dextral reverse offset is relatively common and fold geometry is again of an upright concentric chevron style. D_2 structures are hard to observe without clear cross-cutting relationships, thus the differentiation of structures from separate events is difficult in the field.

Two trends of mesoscopic kinking (outcrop scale) are observed across northeast Tasmania. Sinistral kink bands are dominant and trend NNE-NE with vertical or steeply dipping planes. In contrast, dextral mesoscopic kink bands trend over a large range, between NE and ESE-SE, with the average trend E (Goscombe & Findlay, 1989; Reed, 2004). Variations in the trend of cleavage due to mega-kinking (at regional scales) are commonly in the order of 20° across kink “hinges”. Mega-kink hinges are interpreted to be continuous for up to 30 km. It appears that the dextral kinking event pre-dates sinistral kinking (Goscombe & Findlay, 1989).

5.2. Tyne study area

The study area is located south of the Mathinna Township and ~15 km east of the southern margin of the Scottsdale Batholith. It covers ~50 km^2 (12 x 4 km) and is bounded to the north and east by the South Esk River, to the east by the River Tyne and the south by Tower Hill (Figure 5.1 p. 36).

5.2.1. Stratigraphy

Stratigraphy in the area is poorly understood, although Reed (2004) subdivides the area into a generally fining-up sequence of quartz sandstones, lithic sandstones, cyclic shale and sandstone packages, and a shale rich sequence. Keele, Taylor & Davidson (1994) and Keele (1994) have inferred that the units in the vicinity of the study area form part of the contact between the Turquoise Bluff Slates and the overlying Bellingham Formation and Sidling Sandstones. This relationship is considered tenuous as it is based solely on outcrop lithologies. In several places, post-Carboniferous Lower Parmeener Supergroup sediments form distinctive (topographic highs) escarpments, while in other areas the unconformity surface is only recently exposed.

5.2.2. Structures

The most significant structure in the area forms part of the Alberton – Mangana Lineament, a generally NW-NNW trending topographic feature known colloquially as the Main Slide. This feature is ~2 km wide and ~90 km long (Taheri & Findlay, 1992). To the immediate north of the study area the Main Slide is thought to be offset by a major NE trending sinistral fault/dilatational jog (Taheri & Findlay, 1992; Keele, 1994). This structure, interpreted as a mega-kink domain boundary, runs SW-NE through the study site ~3 km west of the NGGM. Cleavage varies across this boundary from dominantly NNW to NW, south to north (Goscombe & Findlay, 1989). Keele (1994) has inferred a sinistral transfer zone extending from the Main Slide that offsets stratigraphy and structures based on the position and orientation of this mega-kink boundary.

The study area is characterised by NNW-SSE trending folds (D_1) and several major observed and inferred thrust faults and related transfer zones (D_1 and D_2). Generally, fold geometry is of upright chevron style with variable wavelengths (i.e. dm-km). Fold wavelength is observed to decrease with an increasing shale content and decreasing competencies of host lithologies (Reed, 2004). Cleavage is statistically axial planar but can be at high angles to fold axis, presumably from refraction in sand rich beds. Folds plunge either NW or SE up to 30-40° (Taheri & Findlay, 1992; Keele, 1994).

Faulted F_1 hinges are common and often contain quartz veins. However, there are several generations of quartz veins, some of which trend ~10-15° clockwise when compared to the

orientation of proximal NE trending mesoscopic sinistral kink bands (Taheri & Findlay, 1992; Goscombe, McClenaghan & Everard, 1992). A SW directed D_2 compressional event has refolded D_1 folds and caused steeply NE dipping dextral reverse faulting, preferentially on the steep to overturned NE limbs of D_1 folds (Reed, 2004).

5.2.3. Mineralisation

The now abandoned NGGM, was at one time the largest producer of lode gold east of the Tamar Valley (Taheri & Findlay, 1992; Reed, 2004). The NGGM mine was worked to significant depth in contrast to the numerous shallow surface mining prospects and alluvial workings found in the area (Taheri & Findlay, 1992). The area surrounding the NGGM is structurally complex. Reef gold mineralisation occurs within the NE limb of a D_1 anticline in a series of *en-echelon* quartz veins (Finucane, 1935 in Reed, 2004), coincident with the contact between the sandstone rich units and interbedded shale and sandstone succession. The structural setting of the mineralised zone is indicative of NE side-up reverse faulting, consistent with the D_2 deformation orientation (Taheri & Findlay, 1992; Reed, 2004).

Taheri & Findlay (1992) propose a mesothermal gold mineralisation model for the Alberton – Mangana Lineament as mineralisation appears to be concentrated around deep seated regional/crustal scale faults. These faults are likely to have promoted the flow of mineralising fluids possibly originating from granitoid magmas at ~2-3 km depth (Keele, Taylor & Davidson, 1994; Richardson & Roach, 1994). However, the relationships between folding, faulting and mineralisation are still unresolved. There is potential for the discovery of previously unknown gold mineralisation at shallow to moderate depths southeast of Mathinna following the trend of the Alberton-Mangana Lineament and coincident with the buried contact between the sandstone rich and interbedded sandstone and shale units (Taheri & Findlay, 1992).

6. Methodology

This chapter outlines the methods employed for the enhancement, manual extraction/selection and association of attributes to geological structures identified remotely within the study area. It also describes the Moment-of-Inertia (MOI) best-fit plane algorithm, including the assessment and analysis of MOI results.

6.1. Outcrop/lineament identification

6.1.1. DEM derivatives

The method for generating DEM derivatives (smoothed DEM, slope, aspect and curvature) used a semi-automated approach within the GIS software package LandSerf 2.3 (Wood, 2009). LandSerf has the ability to generate both 1st and 2nd derivatives images from continuous surface datasets. This is achieved by fitting quadratic functions to surfaces using predefined kernel filter sizes and a variety of parameters. LandScript is a Java based coding interface that executes various image processing commands (and others) through LandSerf. A script was written in LandScript that imports individual DEM's and generates selected derivatives, aspect, fractal dimension (D), mean curvature (combination of both profile and planar curvature), slope and surface network. The script also generates frequency histograms for each image. A copy of this script (DEM_Derivatives.lsc) can be found in Appendix 1.

The most important images generated in LandSerf for use throughout the course of this project have been DEM slope, aspect and curvature. Slope is defined as the maximum slope (in degrees from horizontal) for each grid cell in the DEM. Aspect is defined as the azimuth (in degrees from grid north) of the maximum slope direction for each grid cell. Slope and aspect are essentially 1st horizontal derivatives of the DEM surface (Wood, 1996). The 2nd derivative of the DEM surface is curvature. Curvature calculates the rate of change of the gradient (slope) of a surface (Wood, 1996) and has been important for defining edges or topographic discontinuities in the landscape.

All image files were converted from ArcGIS grid file format to ASCII (ARC grid text) image format. This was carried out because the ASCII file format (ASC) is read by a large range of image processing GIS software packages and allowed for broad experimentation. The trade-off associated with converting images to the ASC format was that the files sizes are larger resulting in a longer processing time.

6.1.2. Automated lineament detection

A great deal of time was spent investigating the development of automated lineament selection and extraction techniques from DEM derivatives. Unfortunately, these experimental methods did not produce reliable results. Consequently, focus was placed on developing manual interpretive based lineament selection and extraction methods. A summary of the experimental automated methods developed and preliminary results are provided in Appendix 2.

6.1.3. Feature enhancement

Manual identification and digitisation of outcrop/lineament traces was conducted in ArcMAP using a DEM 2nd derivative surface (curvature). Initially the grid cell size of the DEM was resampled from 0.5 m to 2 m. The resolution of the DEM was reduced to minimise the effects of noise and artefacts. The resulting curvature image was displayed in ArcMAP with an image stretch based on 3 standard deviations and inverted rainbow colour ramp with transparency set to 50%. Several hillshade (directional 1st horizontal derivative) images were produced from the curvature image for a range of sun azimuth directions (i.e. 0°, 45°, 90° and315°) with sun angle and vertical exaggeration set to 45° and 4 respectively. The hillshade image was displayed beneath the curvature image. The combination of images resulted in a DEM 3rd derivative surface with positive (i.e. convex) and negative (i.e. concave) surface curvature represented as red and blue coloured pixels respectively. The hillshading defines pixels of maximum curvature (positive or negative) as the boundary between dark and light shades. 10 m contour lines were generated from the 2 m DEM and overlayed on the enhanced curvature images to represent elevation. Figure 6.1 provides an example of the image combination used to manually select and digitise outcrop/lineament traces.

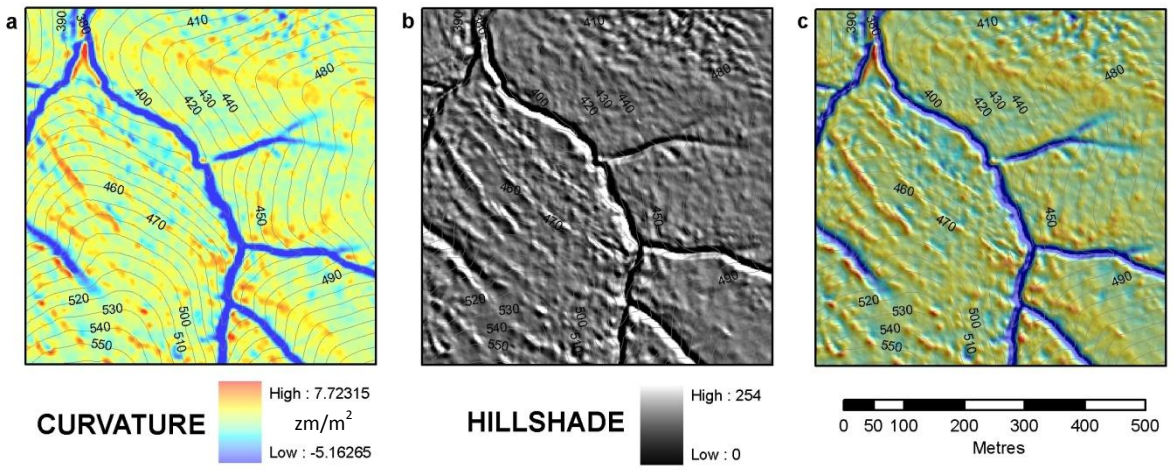

Figure 6.1 Example images for outcrop/lineament identification a) curvature (2nd derivative of 2 m grid DEM (zm/m2)), b) hillshade with azimuth 045°, sun angle 45° and Vertical Exaggeration 4, and c) combined images with curvature transparency set to 50%

6.1.4. Manual outcrop/lineament selection

The enhanced DEM curvature image has been exclusively used to identify, select and manually digitise outcrop/lineament traces within the study area. Traces were identified using visual pattern recognition techniques and digitised as lines in ArcMAP. Digitised traces were given several attributes including: the resolution of the image used (i.e. grid cell size), polarity of the feature (i.e. ridge-convex or channel-concave) and estimated confidence levels.

Confidence levels

Confidence levels were divided in the three categories based on suspected outcrop/lineament trace expression. They are as follows:

- are the pixels representing the feature connected (continuous = 1 or segmented = 3)
- is the feature represented by intense and consistent colour (obvious = 1 or subtle = 3)
- does the feature conform to a suspected structure (plausible = 1 or implausible = 3)
- is the feature straight or curved across the image (curvilinear = 1 or linear = 3)
- is the feature long or short (> ~100 m = 1 or < ~50 m = 3)

Examples of the various confidence level attributed to digitised traces are provided in Figure 6.2. The example of a trace given a confidence level of 1 shows a long (~150 m), continuous, curvilinear feature without discernable offset covering a range of elevations. The intensity of this feature (i.e. its redness) is not high, although colour is reasonably uniform across its entire length. The example of a trace given a confidence level of 3 displays a non-continuous/segmented form. Also it is not a standalone feature, as the centre of the feature blends with another area of high convexity making precise digitisation difficult. The example of a trace given a confidence level of 2 displays offset but is intensely red in colour and its length is in the vicinity of ~80-100 m.

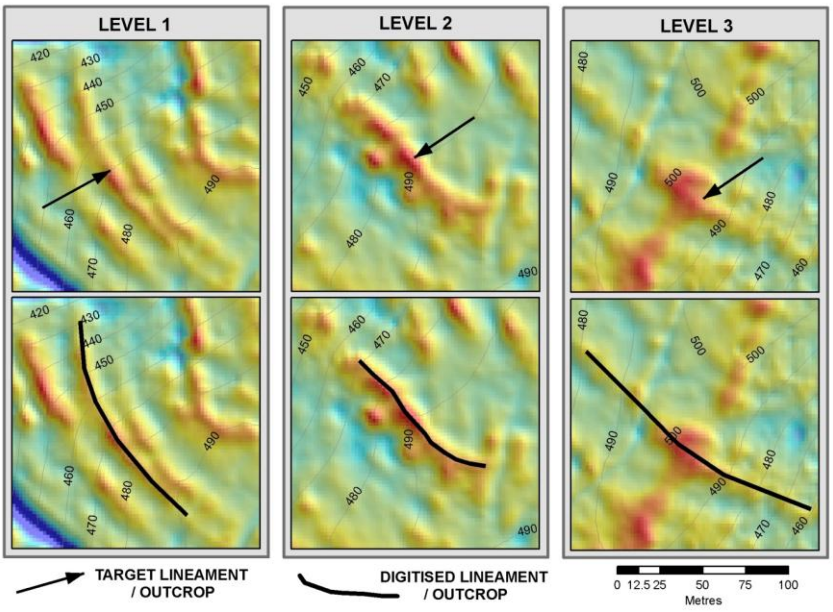

Figure 6.2 Example confidence levels attributed to digitised outcrop/lineament traces identified from enhanced curvature images (zm/m2)

6.2. 3D georeferenced point extraction

Conversion of lines to points in ArcMAP proved to be a long and convoluted process; therefore the following instructions outline the details of the conversion process. Once target features (i.e. outcrop/lineaments) have been identified and digitised as a line in geographic space, the next step is to convert these lines to points. This can be achieved by following the step by step processes summarised in Figure 6.3 and discussed below.

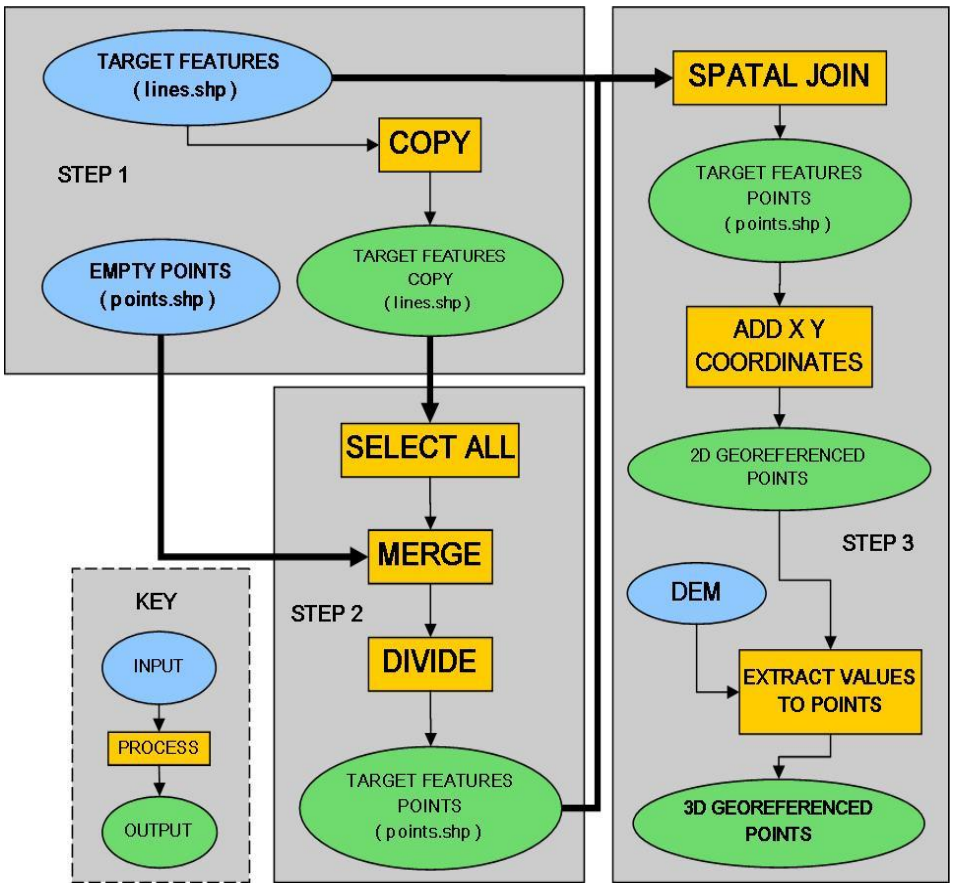

Figure 6.3 Digitised outcrop/lineament trace (line) to points work flow diagram using the ArcMAP editor toolbar

STEP 1 – Preparing feature (line and point) datasets

Copy the file containing the manually digitised lines (outcrop/lineament traces), then create a new empty point feature shapefiles. Both of these files must be placed in the same directory and have a projected coordinate system assigned (e.g. GDA94_MGA_zone_55).

STEP 2 –Converting lines to points

Activate the ArcMAP Editor Toolbar, "Start Editing" and select the directory with the lines and points created in Step 1. Ensure that the empty_points.shp file is the editing Target and that "Task – Modify Feature" is selected. Select all lines (from the copied lines file) that are to have points

associated. Choose the “Merge” function from the drop down “Editor” tab and ensure that one of the Target_features_Lines_Copy.shp rows is selected (Figure 6.4a). Then choose the “Divide” function from the drop down “Editor” tab and select an appropriate spacing via “Place points separated by every *n* units” (Figure 6.4b). Units are determined by the map projection used, in this example points are spaced every 1 m.

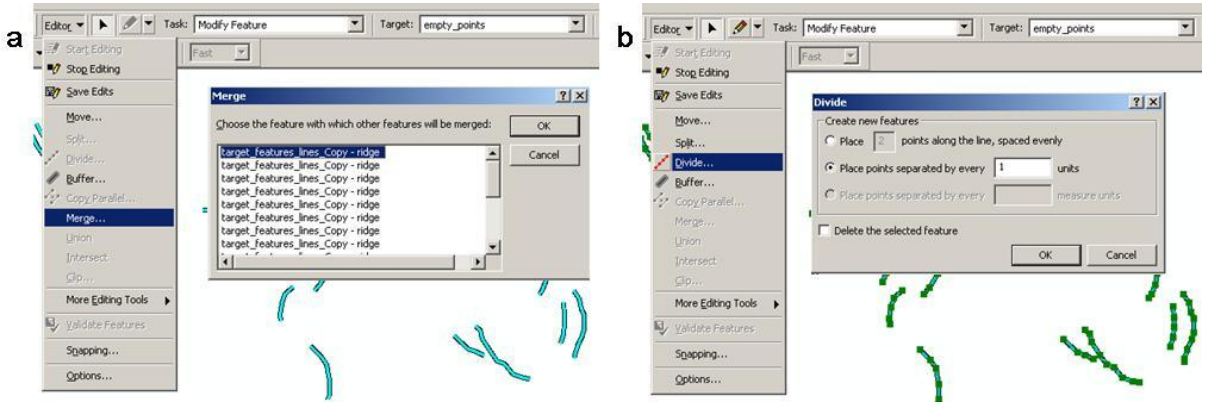

Figure 6.4 Step 2 – ArcMAP Editor Toolbar screen grab a) merging empty points with lines, and b) dividing lines and creating points

STEP 3 – Associating line feature ID and 3D georeferenced coordinates to points

In the Table of Contents (TOC) select the points file created in Step 2, right click and select: “Joins and Relates → Join...”, this opens the “Join Data” window. Ensure that a spatial join will be carried out and that the layer to be joined to the points file is the original Target_features_lines.shp, as the copy of this file has been altered during Step 2. Select “Each point will be given all the attributes of the line that it is closest to...” and choose an appropriate output file name for the joined points shapefile (Figure 6.5). A spatial join associates the original line unique identifier (FID) to the points that were created from respective lines, this is necessary for the PointsToPlane.py program (see Section 6.3) to gather all the points attributed to line features and estimate best-fitting planes.

3D coordinate attributes can be associated to each individual point using the following processes. Firstly, x and y coordinates can be added via: “ArcToolbox → Data Management Tools → Features → Add XY Coordinates”. Secondly, the z coordinate (elevation) is attributed to each point from the appropriate DEM using: “ArcToolbox → Spatial Analyst Tools → Extraction → Extract Values to Points” (a Spatial Analysis Licence is required for this function). Figure 6.6 provides an example point attribute table containing the original digitised line feature unique identifier (FID_2), x (POINT_X), y (POINT_Y) and z (RASTERVALU) coordinate fields for individual points.

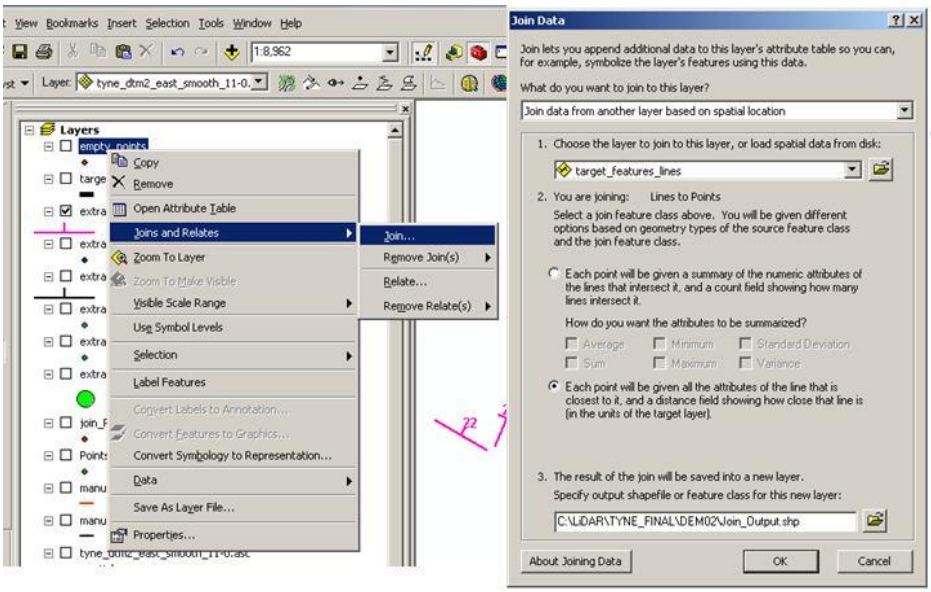

Figure 6.5 Step 3 – Associating points to lines using the spatial join function in ArcMAP

Attributes of extract_Points_manual_first_pass_22_dem_2

FID	Shape *	FID_2	POINT_X	POINT_Y	RASTERVALU
60	Point	0	568457.917871	5403764.34225	666.285339
61	Point	0	568458.917871	5403764.34225	666.387939
62	Point	1	568241.607858	5403889.11146	578.592896
63	Point	1	568242.607858	5403889.11146	579.349121
64	Point	1	568243.607858	5403889.11146	579.349121

Record: 0 Show: All Selected Records (0

Figure 6.6 3D georeferenced points attribute table, note unnecessary fields have been deleted for clarity

6.3. Moment-of-Inertia (MOI) analysis

Fernández (2005) presents two methods for the estimation of best-fit planes through a series of 3D georeferenced points. Both methods assume that the 3D georeferenced points are representative of a planar feature. The first method calculates planar regression statistics for the three coefficients (a, b and c) of a surface in scalar form:

$$z = ax + by + c \qquad (6.1)$$

These coefficients can then be converted to dip and dip direction of a surface in geographic space. The Root Mean Square Error (RMSE) is determined by calculating the distance between the plane and the points that it was generated from. The RMSE provides a measure of the degree-of-fit for the calculated best-fit plane to the points used to estimate it. The degree-of-fit is inversely proportional to the distance between the points and the best-fit plane. However, Fernández

(2005) points out that the RMSE does not necessarily provide an adequate representation for the reliability of the measurement, and thus the stability of the resulting solution.

The second method proposed by Fernández (2005) estimates the Moment-of-Inertia (MOI) of a series of points using the pole (vector normal to a surface) of the best-fit plane as the axis of the MOI. To establish MOI parameters, a symmetrical matrix is constructed containing the products of the difference vectors from the mean x, y and z, coordinates of the points representing a 3D trace of the surface in question. The symmetrical matrix can be solved to obtain its three eigenvalues (λ_1, λ_2 and λ_3) and corresponding eigenvectors (v_1, v_2, and v_3) as outlined by Woodcock (1977) for the calculation of best-fit girdles. Eigenvector v_3 is representative of the pole to the best-fit plane and can be used to determine the linear coefficients of the plane that best-fits the points. It is then possible to convert the linear coefficients to dip and dip direction of the best-fit plane. Using the ratios of eigenvalues, the degree-of-fit and solution reliability can be defined, providing a better representation of result accuracy (Woodcock, 1977; Fernández, 2005).

The degree-of-fit M, obtained from the MOI analysis is defined by the ratio:

$$M = \ln(\lambda_1/\lambda_3) \quad (6.2)$$

Larger ratios represent more co-planar points and increased measurement precision. For example, low values of M are obtained either from a surface that does not fit the assumption of a planar surface (i.e. from folding) or the line feature itself does not correlate well with the exposed surface (i.e. poor extraction) (Fernández, 2005).

Measurement reliability K, is defined by the ratio:

$$K = \ln(\lambda_1/\lambda_2)/\ln(\lambda_2/\lambda_3) \quad (6.3)$$

K corresponds to the degree of co-linearity of points used to define the plane. Smaller values of K represent reduced co-linearity and a more reliable solution (Fernández *et al.*, 2009). Figure 6.7 presents a graphical explanation of M and K values in terms of the spread of the points used to estimate a best-fit plane. The thresholds proposed by Fernández (2005) for optimum results from the MOI analysis are: M > 4 corresponding to points distributed within less than 6° above and below (co-planarity) the estimated best-fit plane; and K < 0.8 corresponding to a distribution of points greater than 30° along the estimated best-fit plane (co-linearity).

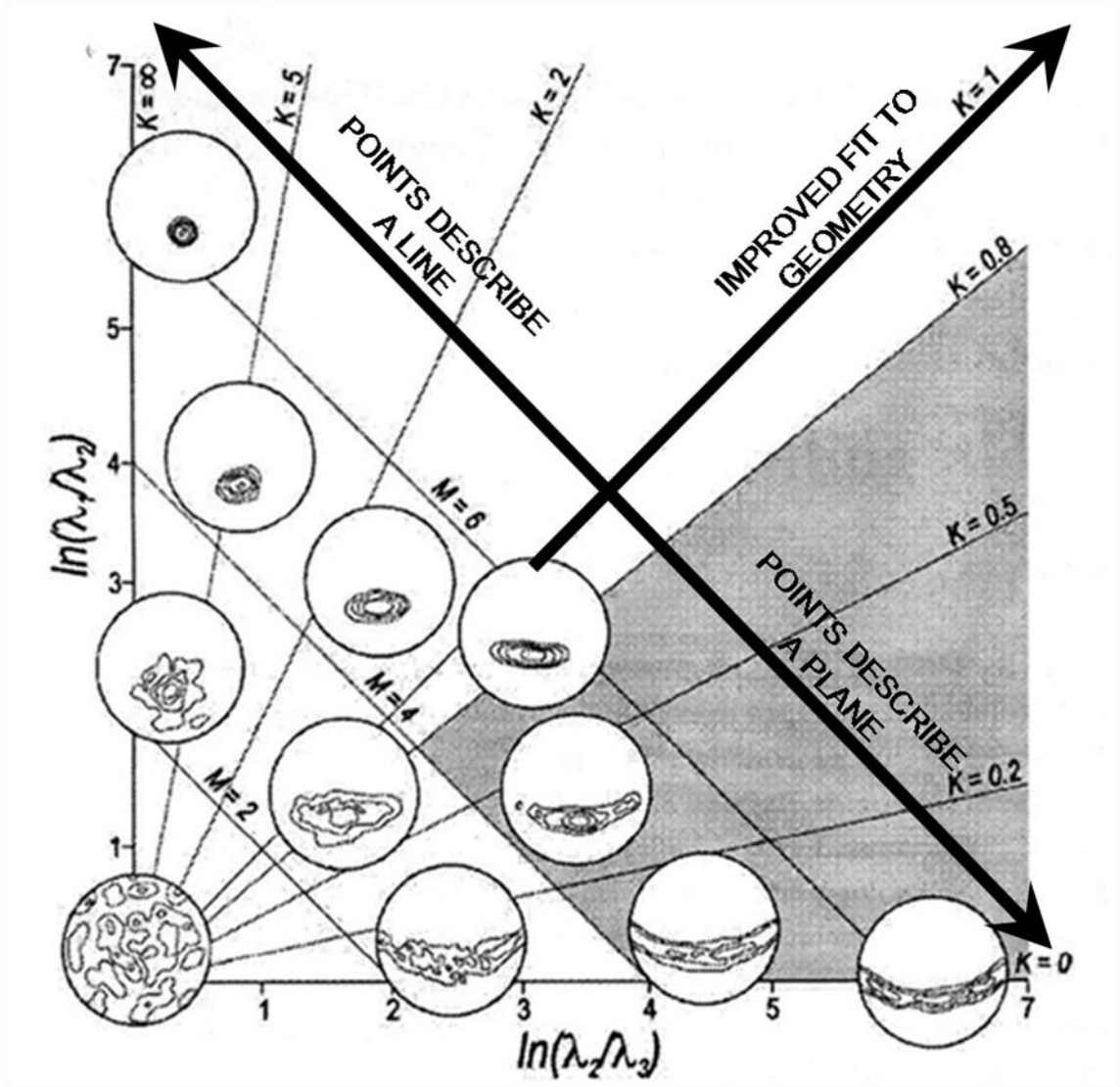

Figure 6.7 Graphic representation of M and K thresholds as proposed by Fernández (2005) and the spread of points used to determine best-fitting planes, modified from Woodcock (1977) in Fernández (2005)

6.3.1. Automating the MOI algorithm

Using python 2.6, the program PointsToPlane.py was written for estimating best-fit planes through 3D georeferenced points using the MOI procedure outlined in Fernández, (2005). PointsToPlane.py reads XBase (DBF) files (created through ArcGIS) containing points with associated feature identification attribute (ID) and x, y and z coordinates then outputs a Comma Separated Values (CSV) file that includes: feature ID; mean x, y and z coordinates of the estimated planes; M, K and RMSE values; coefficients for the calculated plane; and orientation of the plane in degrees of dip (from horizontal) and dip direction (orientation with respect to north). Conversion of the linear coefficients of the plane,

$$0 = ax + by + cz + d \qquad (6.4)$$

to the angles of dip and dip direction in geographic space was conducted using the following equations obtained from Vacher (2000):

$$\theta_{dip} = arctan\left(\sqrt{\left(\frac{a^2+b^2}{c^2}\right)}\right) \quad (6.5)$$

$$\theta_{dip\ direction} = \arctan(-a/b) \quad (6.6)$$

Note: Eq. 6.6 includes a quadrant correction formula.

A copy of the information file (README.txt) and code (PointToPlane.py) for estimating best-fit planes using 3D georeferenced points is provided in Appendix 3 and Appendix 4 respectively.

6.3.2. Evaluating MOI algorithm results

To test the best-fitting plane results obtained from the MOI algorithm, a synthetic DEM and series of "geological" planes with known dip and dip direction were created in ArcINFO 9.3 using information provided in ESRI (2001). The basic principle behind this validation exercise was to define the intersection between the DEM and each plane, then extract points tracing the DEM – plane intersection and associate x, y and z coordinate values for each point. 3D Point data could then be entered into the MOI algorithm program (PointsToPlane.py) and results cross-checked against the original orientation values. Figure 6.8 presents a diagram of the workflow procedure for the validation of the MOI algorithm. Boxes outlining the steps taken correspond to the sections presented below.

STEP 1 – Creating a synthetic DEM

A synthetic topography was created manually from digitising contours within a predefined extent of 500 m x 500 m and attributing elevation (*Zm*) values (to each contour). Coordinates for scene boundaries are analogous to Eastings (*Em* coordinates) and Northings (*Nm* coordinates) for northeast Tasmania. The DEM (5 m grid cell size) was generated by interpolating grid cell values from contour lines using the "Topo-to-DEM" function in 3D Analyst (ArcGIS).

STEP 2 – Converting dip and dip direction of planes to linear coefficients

Arbitrary orientations for synthetic geological planes were created so that a representative range of dip and dip directions from all four quadrants (including cardinal directions) were assessed. Conversion of plane orientations to linear coefficients was conducted using the following formulas modified from Frangos (2008):

$$a = -\tan(dip°) \times \sin(dip\ direction°) \quad (6.7)$$

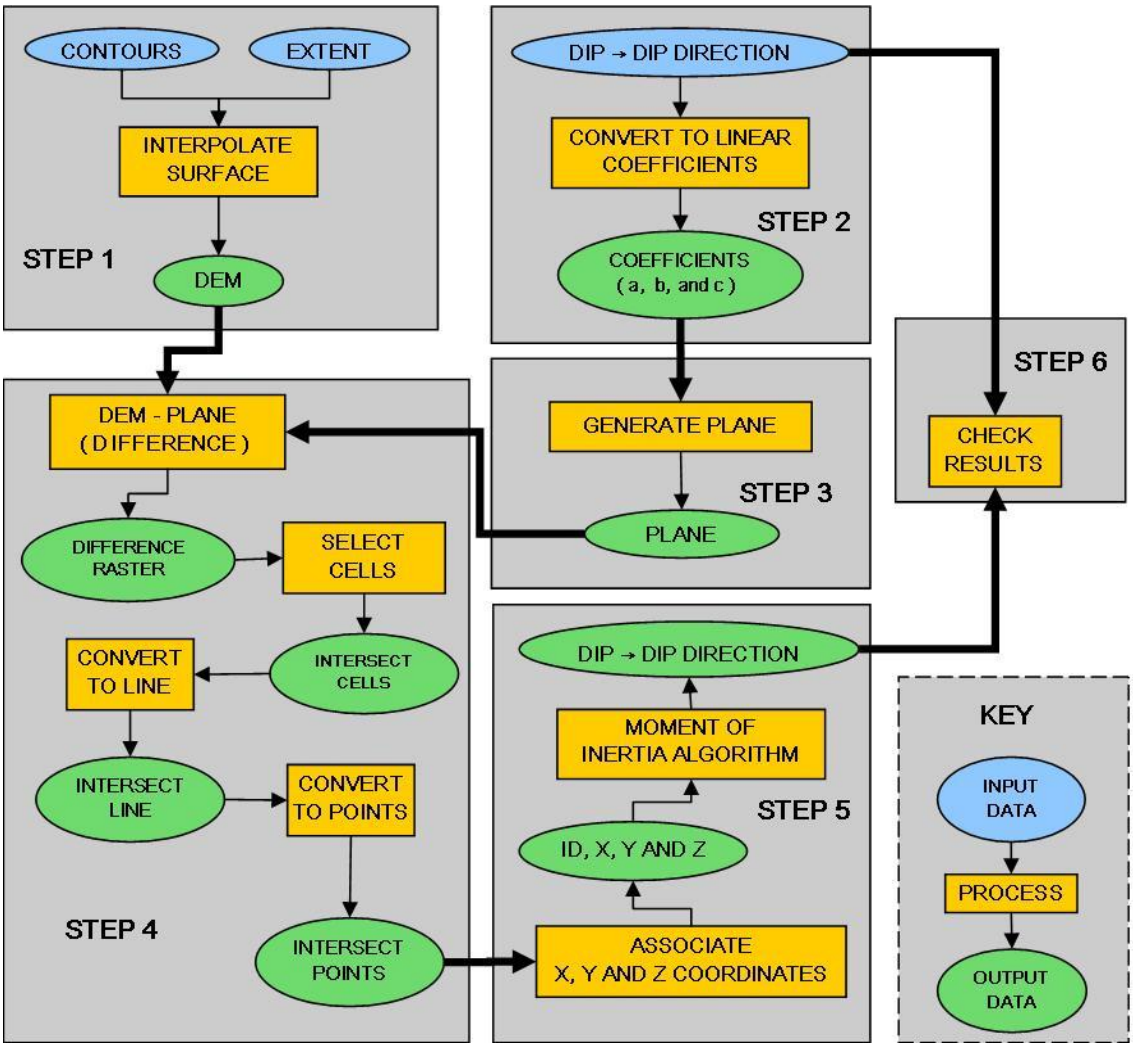

Figure 6.8 MOI algorithm result evaluation procedure work flow diagram

$$b = -\tan(dip°) \times \cos(dip\ direction°) \quad (6.8)$$

$$c = Zm - (a \times Em + b \times Nm) \quad (6.9)$$

Where *Em*, *Nm* and *Zm* are the x, y and z coordinates of a point within the extent respectively.

STEP 3 – Generating a raster surface of a "geological" plane

A script (xygrid.vbp), written in MS Visual Basic 6.0, was created to generate grid surfaces of x and y coordinates for the construction of synthetic geological planes using the linear coefficients created in Step 2. This script reads the header file information from the DEM extent and generates two ASCII grid text files containing x (x.asc) and y (y.asc) coordinate values (see Appendix 5 for a copy of xygrid.vbp). Using the command prompt based ArcINFO interface, both x.asc and y.asc files were converted to Arc grid files (GRD). Coefficients for synthetic planes were entered into the equation of a plane (Eq. 6.1) in ArcINFO to generate raster files representing

"geological" planes (see Appendix 6 for a copy of the ArcINFO commands used to generate synthetic "geological" planes).

STEP 4 – Converting "outcrop" intersection to a line and points

The DEM and plane surface created in Steps 1 and 3 (Figure 6.8 p. 52) are subtracted to define cells corresponding to their intersection and hence the "outcrop" of the plane (Figure 6.9a). Intersection cells (i.e. cell value = 0) are selected using a conditional expression (i.e. greater than and less than). Due to the resolution of the raster files (5 m x 5 m) it was necessary to adjust the selection expression to include cells that were close to zero, with the added benefit of introducing some noise into the synthetic model. Intersection cells are converted to a line feature (Figure 6.9b) followed by conversion of line nodes to point features (Figure 6.9c). Appendix 6 contains an excerpt log file of the commands executed in ArcINFO for this procedure.

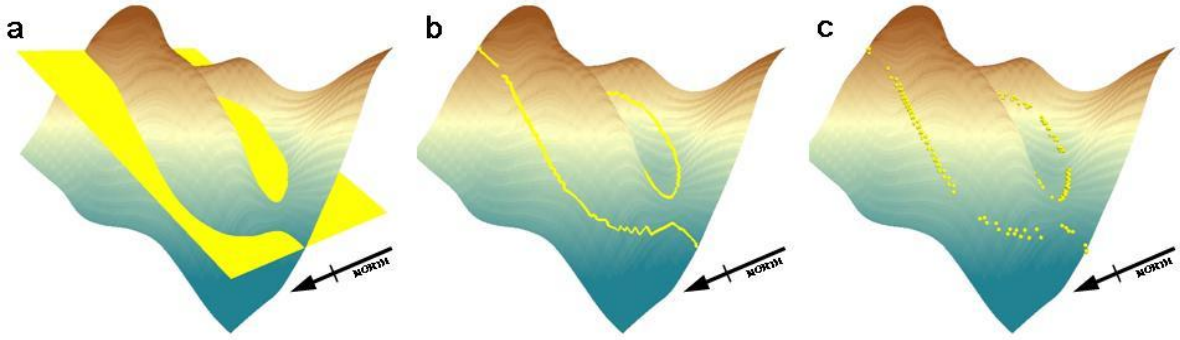

Figure 6.9 Surface to line intersection and points for plane surface orientation 32→270 (ID = 1), oblique view from the NW; a) "geological' plane and DEM intersection, b) "geological" plane and DEM intersection line, and c) intersection line nodes converted to points

STEP 5 – Associating 3D coordinates and feature ID to points

Using ArcGIS, *x*, *y* and z coordinates were associated with points generated in Step 4. The line Identification value (ID) was also attributed to individual points, an important step that allows for the MOI algorithm to identify all the points associated with an individual feature. The entire set of points generated in Step 4 were merged into a single shapefile and the resulting DBF was entered into the MOI algorithm for the calculation of best-fit plane orientation (i.e. dip and dip direction), degree-of-fit (M), solution reliability (K) and RMSE.

STEP 6 – Evaluating results

Table 6.1 provides the output MOI algorithm results and their differences from the original synthetic "geological" plane orientations. Yellow columns represent the resulting differences between the actual orientation of the synthetic "geological" planes and MOI plane orientations. Orange rows highlight calculated plane orientations that do not correctly estimate orientations. The mean x, y and z coordinates have been removed for clarity.

From the data in Table 6.1 it is apparent that 8 out of 11 measurements did not result in any errors (solved to exact integer values of dip and dip direction). This includes the "geological" plane with vertical dip (ID = 5), although the resulting dip direction is rotated 180° the feature has vertical dip and thus this value is acceptable. Calculated planes with errors are easily identified using the degree-of-fit (M) and solution reliability (K) thresholds proposed by Fernández (2005). The erroneous results can be attributed to a lack of points used in the best-fit calculation, resulting in a co-linear series of points used for the definition of best-fit planes. The best-fit plane with the largest error (ID = 2) corresponds to the intersection with the lowest number of attributed points (N_points = 8) and a high co-linearity value (K = 2.526) (Figure 6.10a and 6.10b). The resulting plane surface corresponds to the approximate slope (dip) and aspect (dip direction) of the DEM at the intersection point locations (Figure 6.10c). There are a reduced number of points due to the inadequate thresholds for the DEM and plane intersection procedure in Step 4.

Table 6.1 Output statistics for the Moment-of-Inertia algorithm evaluation dataset (includes error)

ID	N_points	M	K	RMSE (m)	A	B	C	D	Dip	Dipdir°	Actual Dip	Diff Dip	Actual Dipdir°	Diff Dipdir°
1	153	8.212	0.072	2.6	0.53	-0.001	-0.848	-291337	32	270	32	0	270	0
2	8	8.452	2.526	0.4	0.198	0.794	0.575	-4402261	55	14	75	-20	86	-72
3	87	8.196	0.186	2.8	0.043	-0.027	0.999	121275	3	122	3	0	121	1
4	56	8.033	0.474	3	-0.139	-0.314	0.939	1774039	20	204	20	0	204	0
5	51	8.572	0.276	2.1	0.242	-0.97	0.002	5111189	90	166	90	0	346	-180
6	64	8.281	0.17	2.2	0.003	-0.006	1	29994	0	0	0	0	0	0
7	80	8.143	0.227	2.9	0.15	-0.037	0.988	117526	9	104	9	0	104	0
8	46	8.95	0.503	2.1	-0.002	-0.787	0.617	4255072	52	180	52	0	180	0
9	30	9.405	0.626	1.7	0.208	0.977	-0.035	-5401419	88	192	88	0	192	0
10	11	4.999	4.145	2.1	-0.358	0.361	0.861	-1754113	31	315	42	-11	310	5
11	16	7.292	1.862	2.5	0.131	0.21	0.969	-1207801	14	32	15	-1	36	-4

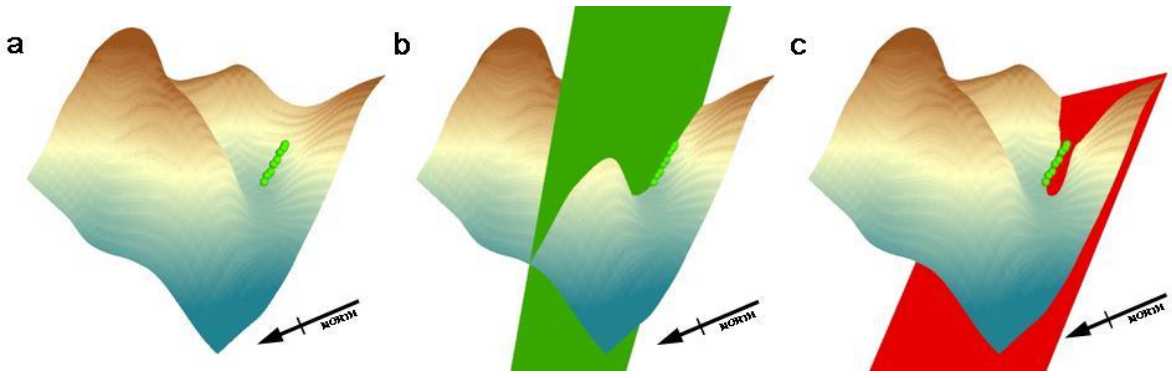

Figure 6.10 Moment of Inertia results for plane orientation 75→086 (ID=2) oblique view from the NW; a) points resulting from "geological" plane intersection, b) original "geological" plane (green), and c) resulting "geological" plane (red) 55→014

6.4. Field work

A total of six days were spent traversing four sites within the study area, each site was between 2 and 4 km^2. Sites were initially selected by identifying suspected geologically related landscape features in the DEM. The aims of the field work were to: collect geological structural data for comparison with structures produced from digitising lineaments/outcrops and MOI algorithm; and gain an understanding of the geomorphological expression, if any, of geological structures and lithologies in the field. In addition, the field data has provided a foundation for understanding the success of the MOI results.

During the course of the field work, standard meso-scale structural and lithological data was collected from outcrops, including; bedding (and facing if possible), cleavage, bedding cleavage intersections, quartz vein and fault orientations, and dominant lithologies. Photographs and sketches of outcrops, in conjunction with observations regarding the geomorphological expression of geological features were recorded with the aim of understanding the surface expression of structures and lithologies.

6.5. MOI algorithm results analysis

As this project has developed an experimental method for the measurement of geological structures using remote sensing data, it was also necessary to develop a technique to test these results. This has been achieved using both data point search functions and stereonets. Comparisons involved assessing the difference between the digitised MOI results and structures measured in the field, both from data publically available from MRT (McClenaghan (comp.), 2007) and the field measurements collected by the author. As a result, analysis of the digitised outcrop/lineament traces and MOI results is limited to areas that contain nearby field measurements.

3D geological structures are characterised by two angular measures; dip (with respect to horizontal) and dip direction (dip azimuth with respect to north). Therefore, comparisons between datasets have been conducted graphically using stereonets and statistically by calculating the dot product of poles-to-planes and assessing the differences between MOI result and field measurement dip and dip direction.

6.5.1. Stereonets

The use of stereonets to compare results is based on the visual assessment of poles-to-bedding clusters and resulting best-fit girdles and fold hinge plunge and trend. Structural domains were defined from the interpretive geological structure map (Section 7.8.3) and used to group data

from areas sharing common structural trends. MRT data and field measurements were plotted separately to MOI results using GEOrient 9.2 (unregistered version).

6.5.2. Automated search methods

This section outlines an alternative automated method to the reliability measures proposed by Fernández (2005) for assessing MOI results that compares dip and dip direction of planes. As the MOI algorithm is designed to extract bedding planes, only the bedding plane data from MRT and field work conducted by the author were compared. The comparison procedure was designed to search along strike an arbitrary distance either side of the mean x and y coordinates of a MOI result to locate field measured data points. Another search method was employed to compare the closest measured bedding dip and dip direction with the along strike search method. The nearest point search method was carried out using the ArcGIS "Point Distance" tool. The "Point Distance" tool defines a search radius (250 m in this case) to the nearest field measurement points from the digitised features. The distance to each point feature from the MOI result is calculated along with ID attributes and appended to a table. This allows for filtering and selection of the nearest point. Subsequent table joins have associated appropriate MOI structure data points with mapped data points using the feature ID attribute.

Along strike search

The basic idea behind selecting points along strike of a structural measurement was to define a search algorithm that identifies points located on the same fold limb as the original point (Figure 6.11). This is because if the nearest field data points are compared, subsequent analysis may incorporate measurements from across a fold hinge. Therefore, the results of the nearest point analysis will in some cases be comparing measurements that are dipping in opposing directions but are both valid measurements. This along strike search algorithm was semi-automated using both python and ArcGIS (ArcINFO and ArcMAP).

The script search_lines.py (Appendix 7) was written in python and reads the CSV file generated by the MOI algorithm. It then calculates strike (from dip direction) and establishes the start and end nodes of a line that passes through the mean x and y coordinates of an individual point. The position of the nodes can be defined as a given distance in metres either side of the original point location. Two search line lengths of 100 m and 200 m distance value were arbitrarily chosen to compare results. This file was output in a format compatible with the "Generate Lines" function in ArcINFO.

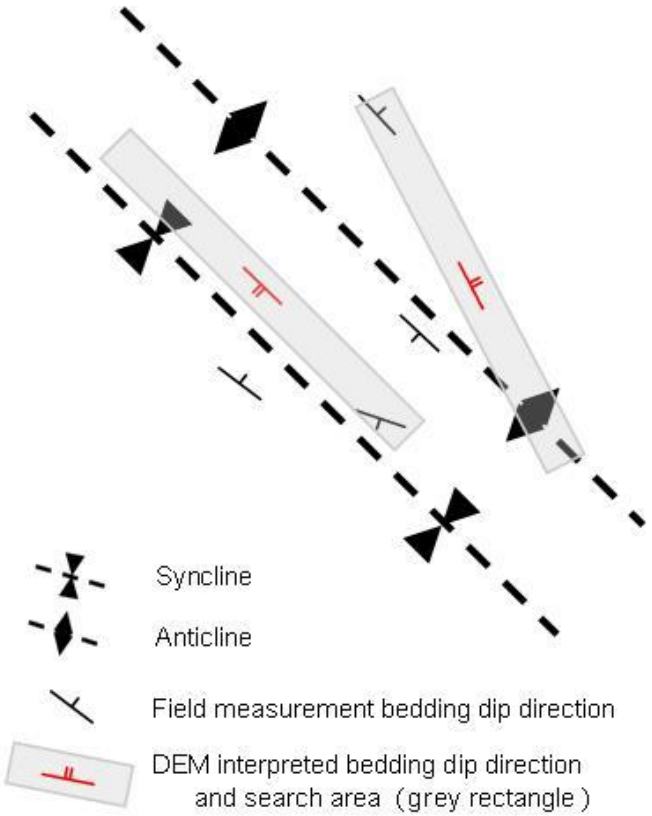

Figure 6.11 Elongate search areas with their long axis in the direction of strike; note that the search area is designed to compare measurements on an individual fold limb which may not necessarily be the closest measurement

Using ArcINFO and information in ESRI (2001) the point node file was converted to a line file using the workflow commands provided in Appendix 8. The resulting line file was then displayed in ArcMAP. A buffer was applied to the line file using ArcToolbox to create elongate rectangular polygons. The width of the polygon search area has been chosen based on a 1:5 aspect ratio (i.e. if length of search area is 100 m then its width is 20 m). The "Identity" tool in ArcGIS was used to append all the attributes of points within a given rectangular search area. Appended attributes include the original ID of the points to be compared and their dip and dip direction values. This table is then joined to the original manually digitised lineament file and related MOI results for analysis.

Dot product comparison

Once field measurements and digitised MOI structures have been grouped based on the search areas defined in the section above, the resulting data can then be compared based on the unit vectors normal to each plane. Cartesian coordinates of the vector normal to the plane were generated using the following equations modified from Stein & Wysession (2003):

x, y, z components respectively of the vector **a** = < a_1, a_2, a_3 > normal to a plane

$$a_1 = -\sin(dip°)\sin(dip\ direction°) \quad (6.10)$$

$$a_2 = -\sin(dip°)\cos(dip\ direction°) \quad (6.11)$$

$$a_3 = \cos(dip°) \quad (6.12)$$

Equations 6.10 – 6.12 produce vectors of both measured structures and MOI results with normalised lengths for comparison. The dot product of compared vectors (**a** = < a_1, a_2, a_3 > and **b** = < b_1, b_2, b_3 >) is calculated using (Stewart, 1999):

$$\mathbf{a} \bullet \mathbf{b} = a_1b_1 + a_2b_2 + a_3b_3 \quad (6.13)$$

The dot product generates a scalar number between -1 and 1 representing the angle cosθ between the two vectors. A result of 1 represents cosθ = 0° (i.e. poles-to-planes of compared measurements are parallel), a result of 0 represents cosθ = 90° (i.e. poles are at right angles to each other), and a result of -1 represents cosθ = 180° (i.e. poles are polar opposites). Table 6.2 presents differences in 5° increments of dip and dip direction and the resulting dot products. The "measured' plane has an orientation of 45→090 and the comparison planes increase in dip *and* dip direction from this plane to a maximum of 45°. The black line in Figure 6.12 graphically presents the data in Table 6.2. It is apparent from that dot products > ~0.95 correspond to differences in dip and dip direction of less than 15° and differences of less than 20° correspond to dot products of > 0.90.

The data presented in Table 6.2 only shows the dot product results for equal differences in dip and dip direction of the compared poles-to-planes. Dot product results will vary based on respective differences in dip and in dip direction. For example, if the difference in dip is 10° and the difference in dip direction is 70° then the resulting dot product is ~0.7. This dot product result is equivalent to the ~35° difference in both dip and dip direction. However, these results represent optimal comparisons. If for instance, the difference in dip between the compared points is 0° and the difference in dip direction increases by 5° increments, the dot product result is represented by the red line in Figure 6.12. This shows that a large difference in dip direction but 0° difference in dip will be represented by a seemingly more reasonable dot product result.

Table 6.2 Dot products for differences in dip and dip direction as compared with a plane orientated 45→090

dip	**45**	**50**	**55**	**60**	**65**	**70**	**75**	**80**	**85**	**90**
dip direction	90	95	100	105	110	115	120	125	130	135
absolute difference in dip	0	5	10	15	20	25	30	35	40	45
absolute difference in dip direction	0	5	10	15	20	25	30	35	40	45
dot product	1.000	0.994	0.976	0.945	0.901	0.844	0.775	0.693	0.601	0.500

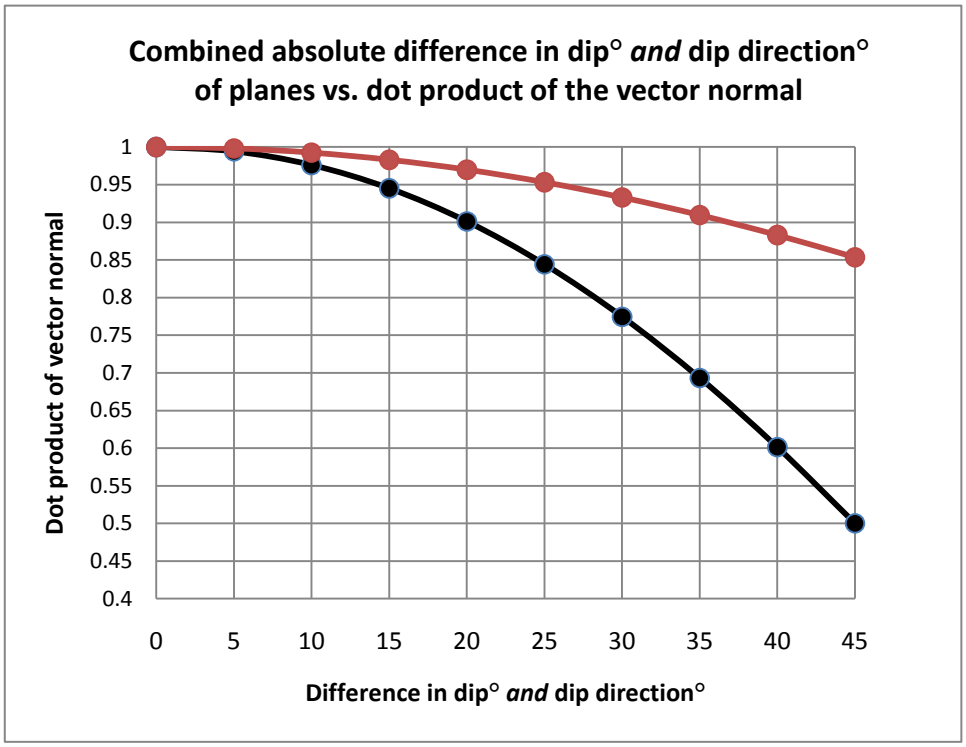

Figure 6.12 Graphic representation of the data presented in Table 6.2 of dot product results of poles- to-planes with increasing but equal differences in dip and dip direction, the red line represents dot product results where the difference in dip remains 0° and difference in dip direction increases incrementally by 5°

7. Results and interpretations

This chapter presents the findings obtained from the qualitative and quantitative comparisons between field structural measurements and the manually digitised outcrop/lineament Moment-of-Inertia (MOI) results. Qualitative and quantitative analyses are combined by assessing field observations, enhanced curvature image characteristics and geological structural cross-sections in conjunction with the degree-of-fit between field data and MOI results. From these initial findings it is apparent that the success of the MOI results is related to the complexity of geological structures observed. In addition, the majority of poor MOI structural results conform to the orientation of the topography (i.e. slope and aspect). Using the latter observation, MOI results have been filtered, removing those measurements that have similar orientations to the slope and aspect of the terrain.

Filtered MOI results are compared with un-filtered results to show the subsequent increase in their comparative reliability. The most substantial improvement in the MOI results is observed in the comparisons of dip direction. For example, prior to filtering the average difference in field measured dip direction to MOI dip direction is ~85°, whereas the filtered MOI structures average difference is ~50°. It is important to note that the search methods used to obtain points for comparison between the field measurements and MOI results appears in some cases to select points from opposing fold limbs. This is due to the highly folded nature of the geology within the study area. Therefore, the mean comparative difference in dip direction does not give a true representation of the reliability of the filtered MOI results.

An attempt has been made to quantify the percentage confidence limits by selecting 500 randomly sampled MOI results and assessing them with neighbouring field measurements. These results suggest that after filtering, ~40-50 % of MOI structures are within 20° of dip and ~70-80% are within 45° of dip direction (includes measurements suspected to represent opposing fold limbs, i.e. 180° difference in dip direction).

A qualitative assessment of MOI results is carried out using poles-to-bedding plotted on stereonets. The results of the stereonet comparisons show some very promising trends. For example, best-fit girdles of poles-to-bedding and resulting fold hinge plunge and trend are often within 5-10°. In addition, fold limbs show comparatively similar vergence geometry between field measurements and the MOI results.

This chapter concludes with several examples of geological structures that were measured observed during the field work and have also been identified using a combination of MOI results and enhanced curvature image manual pattern analysis. These examples are used to justify the interpretation of structures such as synclines, anticlines and faults in areas not covered by field observations. Interpreted structures have been used to develop a geological structural map and two cross-sections.

7.1. Field data

Over the course of six days, four focus areas of ~2km^2 were investigated south of Mathinna in northeast Tasmania. More than 350 structural measurements and basic lithological observations were collected during this period. GPS coordinates for each field site were combined with the field data in ArcGIS. Tables of field measurement location, structures and lithologies are provided in the accompanying DVD. Structural data collected in the field during the course of this project has been combined with pre-existing publically available structural data for the study area (McClenaghan (comp.), 2007) for comparison with the manually digitised features and best-fit planes obtained from the MOI algorithm.

7.2. Manually digitised features and MOI algorithm results

There were 1150 inferred geological features identified and manually digitised from the enhanced curvature image covering the extent of the study area. 3D georeferenced points spaced 2 m apart were generated along the length of each outcrop/lineament trace. The points extracted from these traces were imported into the PointsToPlane.py program (MOI algorithm) and the resulting dip and dip direction of best-fitting planes were plotted in ArcMAP. The 2D locations of the digitised structures are based on the mean x and y coordinate information generated during the MOI analysis.

A range of search functions were utilised to compare MOI results and field measurements as discussed in Section 6.5. The search results were compared using a combination of the difference between dip and dip direction, and dot product comparison of the pole to the MOI results and field measurement bedding planes. The MOI solution reliability parameters proposed by Fernández (2005) have not been investigated for data filtering and assessment. Preliminary results show that all MOI results have a value of $M > 4$, while only ~10% of results have values of $K < 0.8$. Filtering the MOI results based on these suggested thresholds (Fernández, 2005) would have reduced the number of data points to levels for unsuitable comparison. Therefore, comparisons have focussed on the absolute differences between field measurements and MOI

results. Nevertheless, very high M values predict that the bulk of MOI best-fit planes have a good degree-of-fit. Whereas, the large proportion high K values predict the majority of MOI results are defining lines, not planes.

7.3. Comparative assessment of MOI structures with field observations

Figure 7.1 show the frequency histogram and cumulative percentages obtained from the comparison of field measurement and MOI results for difference in dip, difference in dip direction and dot products of poles-to-planes. These results show that there is very little difference between the respective search methods. Difference in dip and dot product results are positively and negatively skewed respectively. This suggests that in general the MOI results are conforming to the dip of measured bedding planes. Conversely, dip direction differences show a wide spread of values with a slight bi-modal distribution, best observed in the 400 m x 80 m elongate search rectangle results. This bi-model distribution is likely to be from the comparison of measurements on opposing fold limbs.

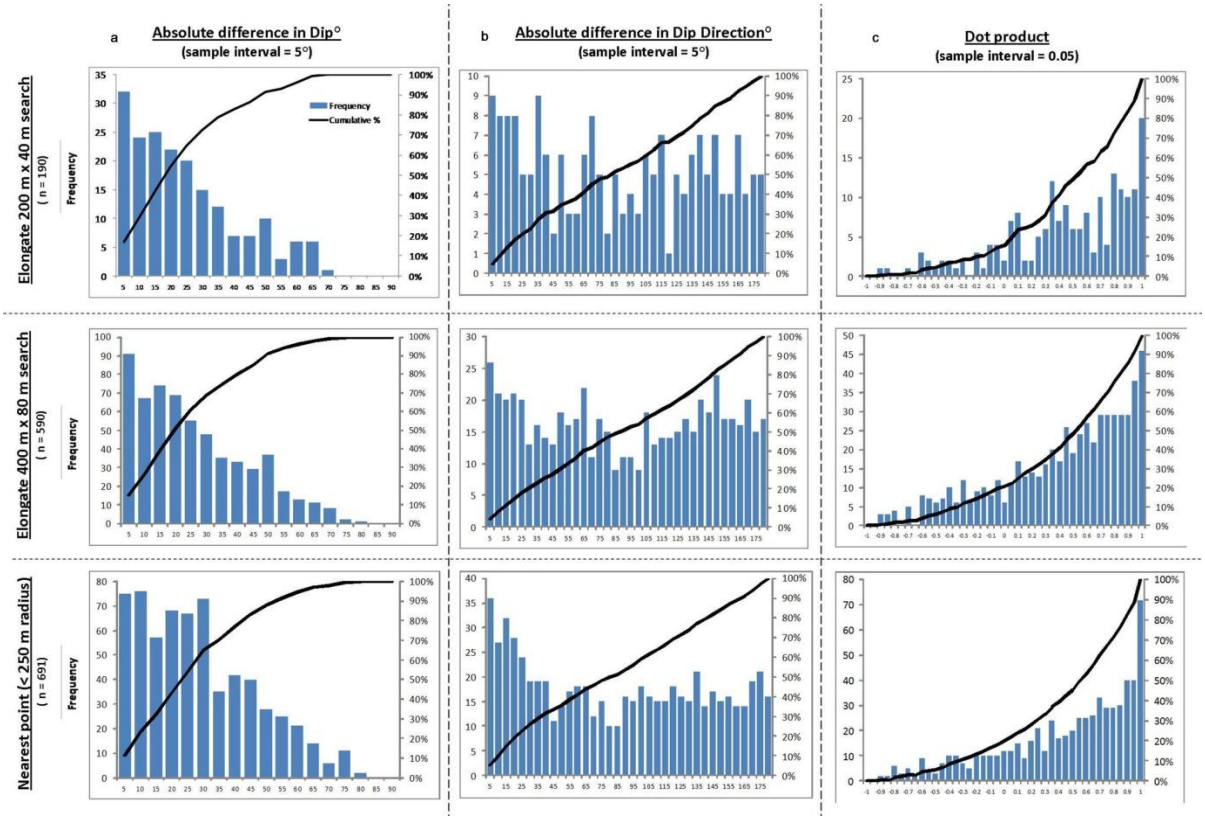

Figure 7.1 Frequency histograms and cumulative percentages for the MOI results and field measurement comparisons using elongate rectangular search areas and nearest point search methods, a) absolute difference in dip, b) absolute difference in dip direction and c) dot product of poles-to-planes

Table 7.1 provides a basic statistical comparison of the results presented in Figure 7.1. The mean difference between dip and dip direction are ~25° and ~85° respectively. The statistics for mean difference in dip direction should be viewed with some scepticism due to the bimodal distribution discussed above.

Table 7.1 Comparative statistics from the three different search methods employed to test the degree-of-fit between the digitised outcrop/lineaments MOI results and field measurements of bedding planes

	Absolute difference in Dip			Absolute difference in Dip direction			Dot Product		
	Elongate 200 x 40 m search	Elongate 400 x 80 m search	Nearest point (< 250 m radius)	Elongate 200 x 40 m search	Elongate 400 x 80 m search	Nearest point (< 250 m radius)	Elongate 200 x 40 m search	Elongate 400 x 80 m search	Nearest point (< 250 m radius)
Mean	22.49	23.90	26.47	84.96	88.89	82.59	0.4395	0.3979	0.4302
Median	19	20	24	82.5	89	81	0.5179	0.5189	0.5626
Mode	11	1	18	34	148	12	#N/A	#N/A	#N/A
Standard Deviation	17.35	17.61	18.24	55.30	55.06	56.01	0.4516	0.4803	0.4852
Kurtosis	-0.27	-0.35	-0.35	-1.35	-1.34	-1.33	0.07	-0.27	-0.17
Skewness	0.78	0.68	0.61	0.08	-0.01	0.13	-0.83	-0.79	-0.85
Range	66	78	79	177	180	179	1.9148	1.9396	1.9396
Minimum	0	0	0	2	0	0	-0.9156	-0.9399	-0.9399
Maximum	66	78	79	179	180	179	0.9991	0.9996	0.9996
Count	190	590	641	190	590	641	190	590	641

7.4. Field examples

Field examples of sites corresponding to a range comparison results have been selected in an attempt to graphically depict situations where the digitised outcrop/lineament MOI results have succeeded in defining bedding planes, and where it has failed. Figures 7.2 and 7.3 present this information using photographs, plan views of the digitised features as seen in the enhanced curvature images, cross-sections perpendicular to the digitised features of elevation (includes geological cross-sections) and surface curvature, and tables of comparison results. The degree-of-fit between the MOI structures and field measurements are divided into four colour coded categories (i.e. Blue (GOOD) <= 5°; Green (OK) <= 20°; Yellow (MODERATE) <= 45°; and Red (POOR) > 45°).

The majority of features digitised represent positive curvature. These in many cases conform to outcrops of sand rich lithologies. Conversely, shale rich beds in many cases form landscape depression and shallow channels. More than once in the field it was noted that interbedded sand and shale beds developed into landforms with discrete ridge and channel profiles.

GOOD (<=5°) TO OK (<=20°)

T327

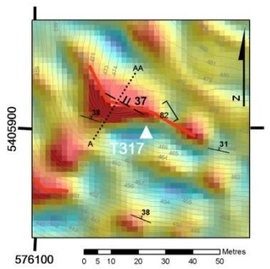

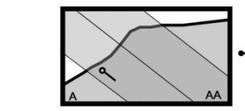

20 m

VE = 1

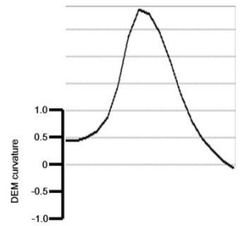

SITE	MOI ID	Confidence Level	MOI (Dip°→Dip Direction°)	So (Dip°→Dip Direction°)	Dot Product	Diff. Dip°	Diff. Dip Direction°	DEM (~Slope°→~Aspect°)	Diff. Slope°	Diff. Aspect°
T327	24	2	37→029	38→018	0.993	1	11	25→225	12	164
T327				38→022	0.997	1	7			
T327				31→012	0.981	6	17			

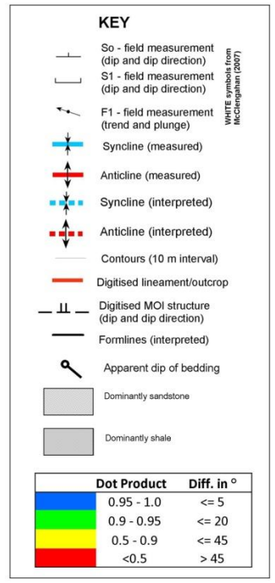

T618, T619 and T620

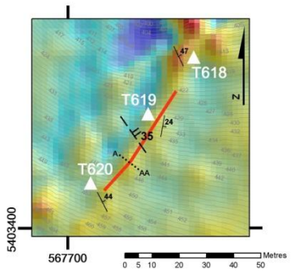

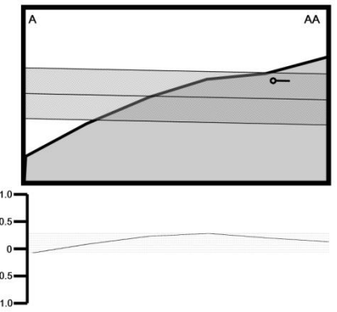

4 m

VE = 1

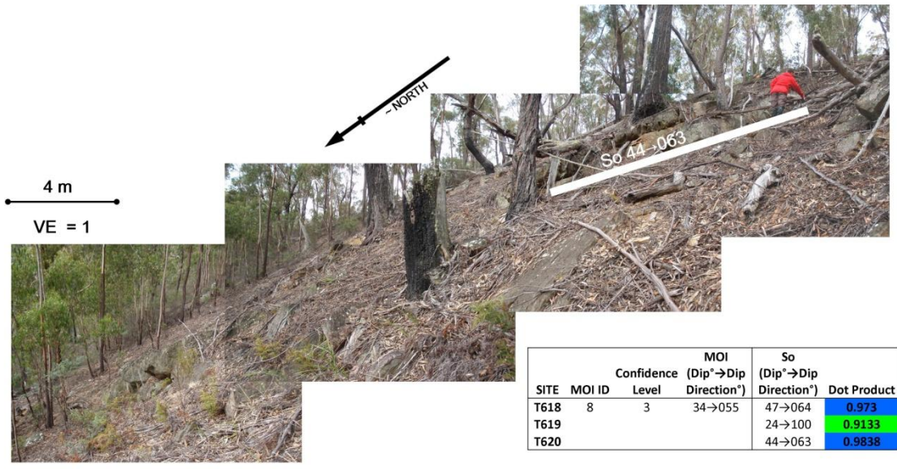

SITE	MOI ID	Confidence Level	MOI (Dip°→Dip Direction°)	So (Dip°→Dip Direction°)	Dot Product	Diff. Dip°	Diff. Dip Direction°	DEM (~Slope°→~Aspect°)	Diff. Slope°	Diff. Aspect°
T618	8	3	34→055	47→064	0.973	13	9	35→005	1	50
T619				24→100	0.9133	10	45			
T620				44→063	0.9838	10	8			

MODERATE (<=45°)

T410

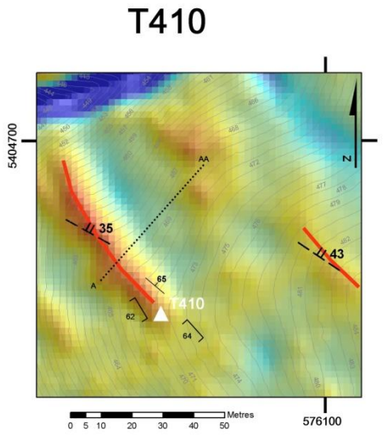

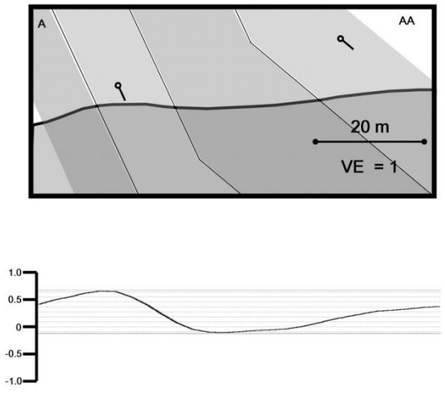

SITE	MOI ID	Confidence Level	MOI (Dip°→Dip Direction°)	So (Dip°→Dip Direction°)	Dot Product	Diff. Dip°	Diff. Dip Direction°	DEM (~Slope°→~Aspect°)	Diff. Slope°	Diff. Aspect°
T410	240	3	43→034	65→055	0.8861	22	21	12→315	31	79
T410	241		35→029	65→055	0.8134	30	26	20→295	15	94

Figure 7.2 Field observations and MOI results comparisons for Good (<= 5°), OK (<= 20°) and Moderate (<= 45°) differences in dip, dip direction and dot product results, included images are (from left to right): enhanced curvature image (see Figure 6.1 for colour scale) with overlayed field observations and MOI results; interpreted geological cross-section and curvature profile (zm/m^2); outcrop photographs with overlayed bedding planes; and table of comparison results, includes DEM (10 m) slope and aspect (example Confidence Levels can be found in Section 6.1.4)

MODERATE (<=45°) TO POOR (>45°)

T517, T518, T519 and T520

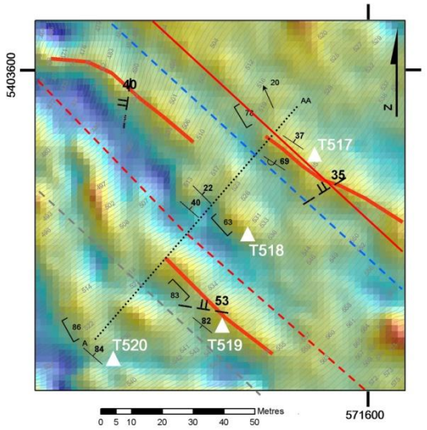

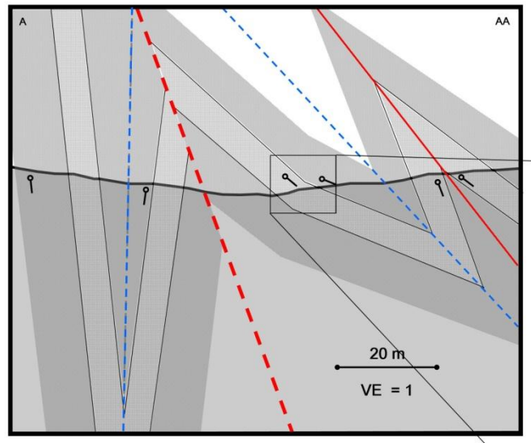

SITE	MOI ID	Confidence Level	MOI (Dip°→Dip Direction°)	So (Dip°→Dip Direction°)	Dot Product	Diff. Dip°	Diff. Dip Direction°	DEM (~Slope°→~Aspect°)	Diff. Slope°	Diff. Aspect°
T517	620	3	35→328	37→034	0.7946	2	66	32→305	3	23
T517				69→033	0.5199	34	65			
T517	621	3	40→278	37→034	0.4422	3	166	38→285	2	7
T517				69→033	0.0209	29	115			
T518				22→045	0.5654	18	127			
T519	588	3	53→009	82→219	-0.6012	29	150	35→320	18	49
T520				84→041	0.7365	31	32			

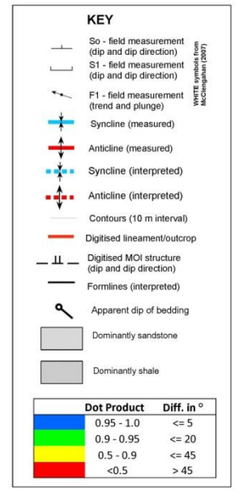

T608, T609, T610 and T611

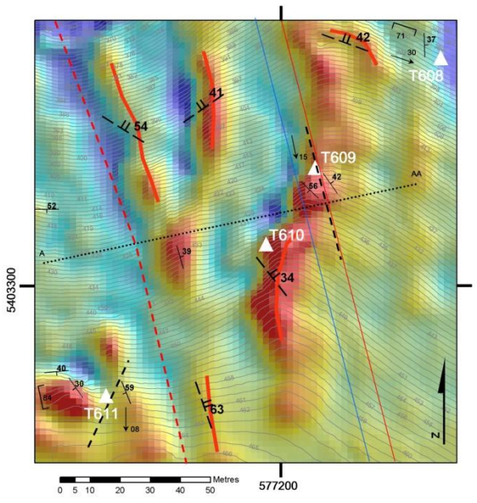

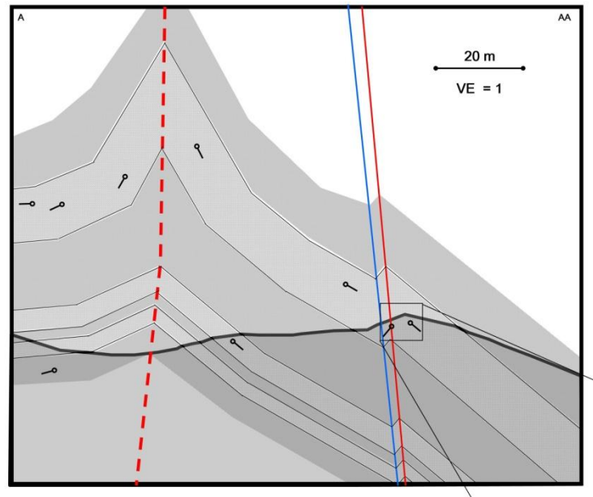

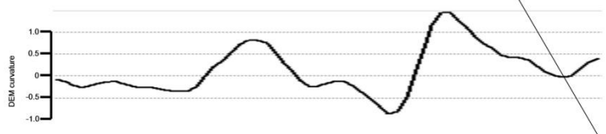

SITE	MOI ID	Confidence Level	MOI (Dip°→ Dip Direction°)	So (Dip°→ Dip Direction°)	Dot Product	Diff. Dip°	Diff. Dip Direction°	DEM (~Slope°→~Aspect°)	Diff. Slope°	Diff. Aspect°
T608	112	3	42→020	37→088	0.7444	5	68	35→012	7	8
T609				42→055	0.919	0	35			
T609				56→224	-0.0912	14	156			
T608	113	1	41→325	37→088	0.3877	4	123	38→330	3	5
T609				42→055	0.5609	1	90			
T609				56→224	0.3182	15	101			
T610				39→074	0.4521	2	109			
T609	110	2	34→052	42→055	0.9898	8	3	22→355	12	57
T609				56→224	0.0045	22	172			
T610				39→074	0.9706	5	22			
T610	108	3	54→032	39→074	0.8352	15	42	40→340	14	52
T610				52→180	-0.1788	2	148			
T611				59→248	-0.2583	5	144			
T611				30→235	0.1367	24	157			
T611				40→175	0.035	14	143			
T610	109	3	63→071	39→074	0.9128	24	3	20→352	43	79
T610				52→180	0.0509	11	109			
T611				59→248	-0.5289	4	177			
T611				30→235	-0.0351	33	164			
T611				40→175	0.2092	23	104			

Figure 7.3 Field observations and MOI results comparisons for Moderate (<= 45°) and Poor (> 45°) differences in dip, dip direction and dot product results, included images are (from left to right): enhanced curvature image (see Figure 6.1 for colour scale) with overlayed field observations and MOI results; interpreted geological cross-section and curvature profile (zm/m^2); outcrop photographs with overlayed bedding planes; and table of comparison results, includes DEM (10 m) slope and aspect (example Confidence Levels can be found in Section 6.1.4)

However, it was unlikely to actually observe shale outcropping in these situations as the only evidence was inferred from an increase in surface clasts of shale fragments (~5-10 cm long) in shallow depressions. All MOI results are presented as facing unknown because it is impossible to determine if a digitised structure represents an overturned bed or not. This is only possible using outcrop scale observations collected in the field.

Initial observations suggest that more complex geological structures produce less reliable MOI results. Poor results are seen where faulting and folding occurs in conjunction with reduced fold wavelengths. These structural complexities are more commonly observed in areas dominated by of shale rich lithologies. For instance, Figure 7.2 shows areas of uniformly dipping beds over scales of > ~50 m, whereas Figure 7.3 presents situations of reduced MOI result reliability in areas with fold wavelengths of <= ~50 m.

A high proportion of poor MOI results seemingly identify the slope and aspect of the terrain rather than the geological structures present. A good example of this is provided at sites T517 and T610 (Figure 7.3). In both cases, the difference between the MOI results dip and dip direction and the terrain slope and aspect is less than 5° and 10° respectively for poor MOI results.

Curvature cross-sections (along the same profile line as the structural cross-sections) suggest that features with curvature greater than ± 1.0 zm/m^2 produce better results than features where curvature is less than ± 0.5 zm/m^2. Locations with high curvature correspond to scarp faces, prominent ridges, valley floors and river channels.

Several iterations of the digitisation of outcrop/lineaments were used to obtain the MOI results, different results were produced from each iteration. This is due to issues of reproducibility of manually digitised features. Selection of features may be reasonably robust in that the observer making the selection generally chooses the same features. Nevertheless, the act of drawing a line across a feature will be different for every attempt, and thus small changes in the position of the digitised line will result in changes to the orientation of best-fit planes estimated by the MOI algorithm.

7.5. Filtering MOI results

The initial comparison of the MOI results with field measured bedding planes did not produce reliable results. However, it was observed that as the difference between the slope and aspect of the terrain and the dip and dip direction of the MOI results increased, there was a subsequent decrease in comparative error. Based on this observation, the MOI results have been filtered using the slope and aspect of the terrain.

A 10 m DEM was used to generate slope and aspect data for two reasons. Firstly, the conversion of gridded slope and aspect images to point (vector) data was computer processing intensive when using higher resolution images. Secondly, it was desirable to associate an average slope and aspect to the MOI points. This is because the point location for the MOI structures is defined by the mean x and y coordinates of the digitised outcrop/lineament used to generate the best-fit plane, and slope and aspect often varies across the length of this feature.

Slope and aspect of the terrain was converted from grid data to point data. The resulting point data is located at the centre of respective grid cells. The two separate point datasets (i.e. slope and aspect) were joined based on their IDs. Spatially coincident points shared the same ID as the conversion process from grid to point creates points sequentially in the same order (i.e. left to right, then top to bottom of an image). Once slope and aspect had been appended into a single dataset, it was possible to join this information to the MOI search comparison results. The resulting table was imported into MS Excel for statistical analysis and subsequent filtering based on the difference between terrain slope and aspect and dip and dip direction of the MOI results. Table 7.2 presents descriptive statistics for the difference in dip and terrain slope, and the difference between dip direction and terrain aspect. Features have been selected based on the 200 m x 40 m search method. The resulting filtering thresholds conform to the mean difference in MOI result dip to slope of ~20°, and dip direction to aspect of ~45°.

Table 7.2 Descriptive statistics for the difference in MOI result dip to DEM slope and MOI result dip direction and DEM aspect (obtained from the 200m x 40 m MOI results elongate search rectangle method)

	Difference in MOI dip and DEM slope°	Difference in MOI dip direction and DEM aspect°
Mean	20.2	44.2
Median	12.5	34.8
Mode	5.7	11.1
Standard Deviation	19.2	39.4
Range	82.7	174.8
Kurtosis	0.68	1.98
Skewness	1.22	1.46
Minimum	0.5	1.3
Maximum	83.2	176.1
Count	190	190

The following nested logic statement was used to select data for subsequent analysis:

Select data IF: "Diff. aspect and dip direction" >= 45°

OR "Diff. aspect and dip direction" < 45° AND "Diff. slope and dip" >= 20°

This statement selects all MOI results that have a difference > 45° from aspect and those that have < 45° difference in aspect and dip direction on the condition that the slope and dip difference is > 20°.

Obvious evidence regarding the improvement of MOI results after filtering is observed in the frequency histograms and cumulative percentages is presented in Figure 7.4. The slope and aspect filtering step has removed a large proportion of the MOI results displaying a 45°-135° difference in dip direction. In addition, the dot product comparison frequency histograms show a larger proportion of measurements with differences of 20° in dip and dip direction preserved after filtering. Filtered dip direction MOI results in Figure 7.4 show a bi-modal distribution, the first peak falling at ~20° and second at ~150°, providing encouraging evidence for the assumption that measurements from opposing fold limbs are being compared during analysis.

Table 7.3 presents the results of the difference in dip and dip direction, and dot product comparison of the filtered MOI results (using the terrain slope and aspect thresholds described above). These results suggest that the mean differences in dip and dip direction are ~21 ° and ~74° respectively and the dot product comparison mean difference is > 45°. This is not a vast improvement on the results provided in Table 7.1. However, once again the mean difference in dip direction results is likely to be reflecting comparisons of bedding on opposing fold limbs.

Table 7.3 Descriptive statistics of the comparison between filtered MOI results and field measured bedding planes using the 200 m x 40 m MOI results elongate search rectangle method

	Absolute difference in dip	Absolute difference in dip direction	Dot product of poles-to-planes
Mean	21.2	74.0	0.4130
Median	18	49	0.6215
Mode	6	17	#N/A
Standard Deviation	16.2	61.6	0.5547
Kurtosis	-0.17	-1.47	-0.71
Skewness	0.80	0.40	-0.72
Range	66	177	1.9148
Minimum	0	2	-0.9156
Maximum	66	179	0.9991
Count	95	95	95

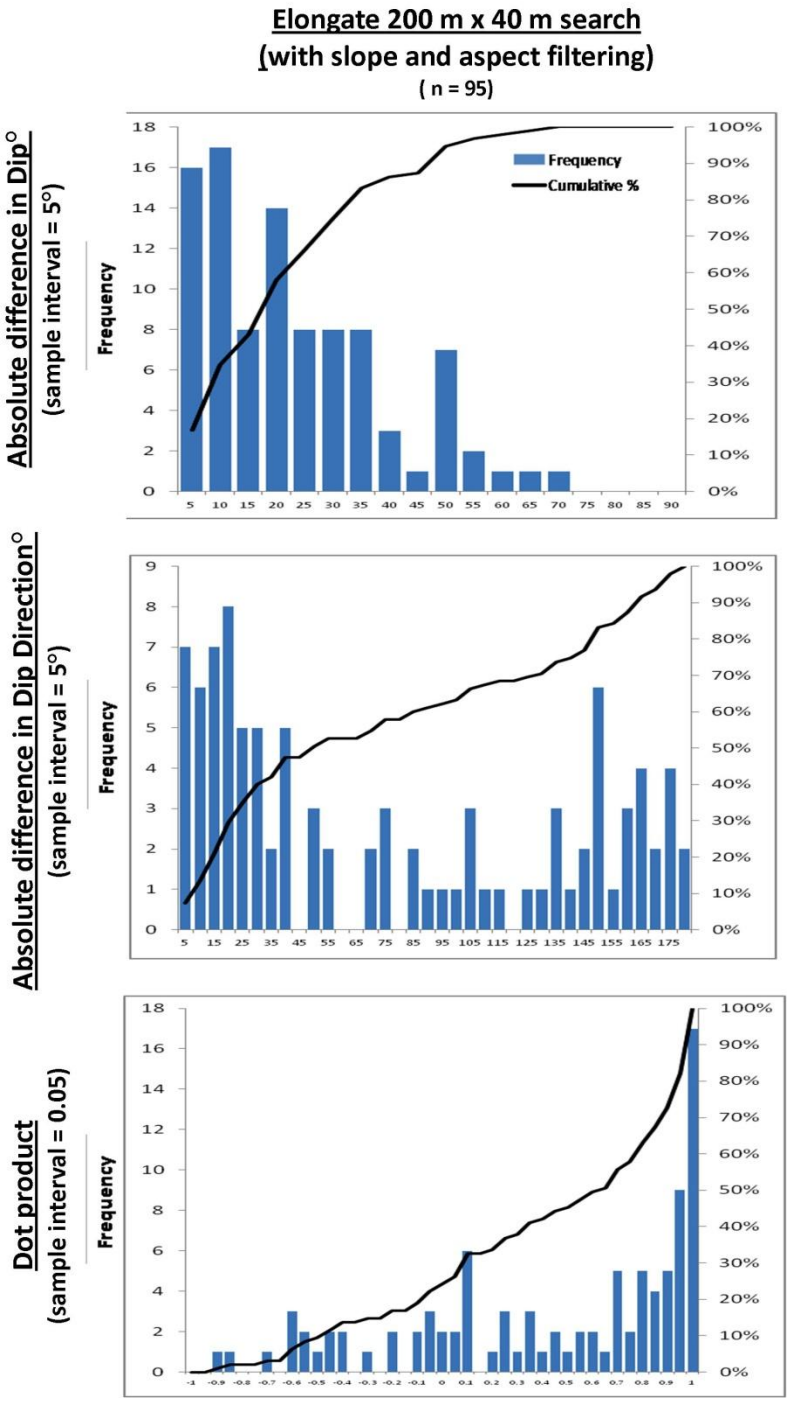

Figure 7.4 Frequency histograms showing the difference in dip, dip direction and dot product comparisons of filtered MOI results and field measure bedding planes obtained from the 200 x 40 m elongate rectangle search method

The origin of the bi-modal distribution of differences in dip direction between field measured bedding planes and the filtered MOI results is apparent in the scatter plots presented in Figure 7.5b. Measured dip direction versus the filtered MOI dip direction produces three distinct clusters of points. Two clusters fall within the zone of < 20° difference in dip direction. The first is centred on ~30°-45° and the second on ~225°. These orientations conform to the east and west limbs respectively of anticlines observed within the study area. The third distinct cluster of points is

centred on ~240° for measured dip direction and on ~30°-45° for the filtered MOI results relative dip direction. This relationship suggests that the third cluster of points is likely to be an artefact of the search method used to associate measurements for comparison, such that structures on opposing fold limbs are being compared. In contrast, the comparison between the dip of field measured bedding planes and filtered MOI results (Figure 7.5a) do not show any distinct clusters of points. The wide range of results in this scatter plot suggest that either it is difficult to establish actual dip angles using the MOI algorithm, or that the fold limbs in the study area are characterised by rapidly change dips.

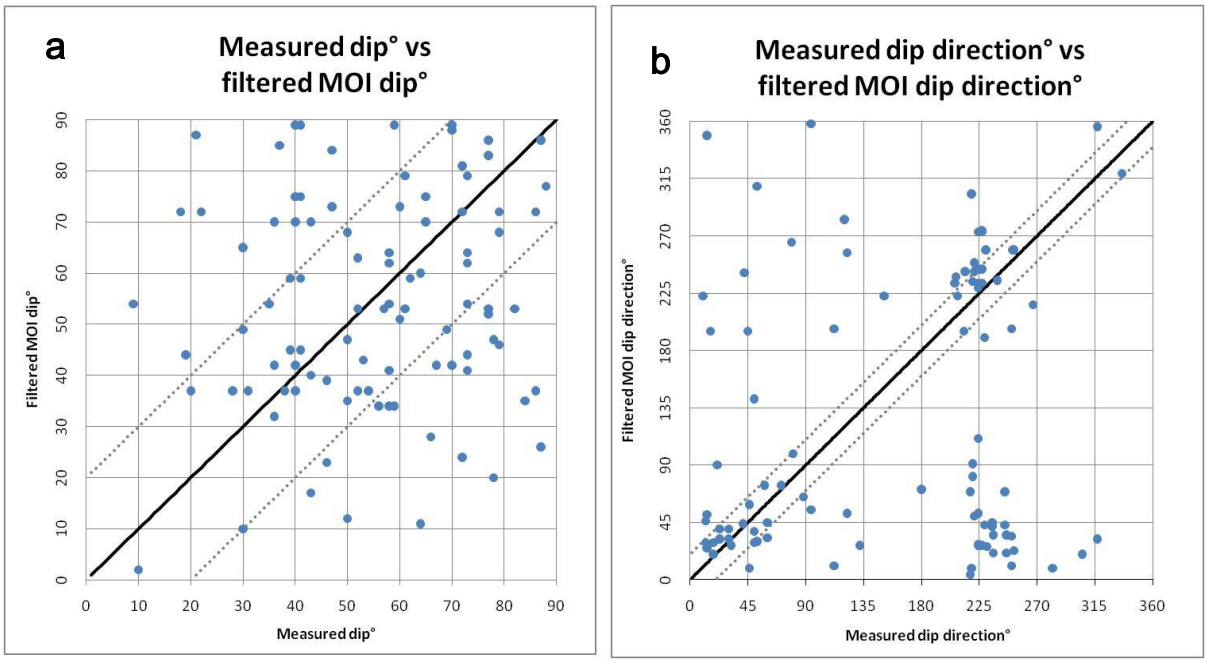

Figure 7.5 Scatter plots of the orientation of field measured bedding planes vs. filtered MOI results, a) dip and b) dip direction, black lines represent a 1 to 1 relationship while the dashed grey lines represent the ±20° difference threshold

7.6. MOI results percentage confidence limits

A total of 500 MOI results were randomly sampled to assess degree-of-fit percentage confidence limits. Field data was sampled using the nearest point search (to within 250 m) from the location of the included MOI results. Figure 7.6 presents this data graphically as discrete percentages and cumulative percentage of the degree-of-fit categories defined in Section 7.4. A table of results corresponding to the data shown in Figure 7.6 is provided in Appendix 9. The uncertain category in Figure 7.6a represents randomly sampled MOI results that did not have a comparable field measurement within a radius of 250 m. The differences in dip direction and dot product comparison percentages have been calculated by including polar opposite outliers. This has been carried out in an attempt to adequately categorise those comparisons of measurements on opposing fold limbs. For example, the <= 5° (GOOD) difference category includes both dip

direction differences <= 5° but also dip direction differences of >= 175°. This method has been based on the findings presented in Section 7.5.

The total sample statistics presented in Figure 7.6a show that ~42% of the MOI results could not be validated as there were no comparable field measurements within 250 m. After filtering, (Figure 7.6b) a subset of 147 points were analysed, this equates to ~30% of total samples or ~51% of comparable samples. Within the filtered sample subset ~45% of MOI results were within 20° and ~75% were within 45° of field measured dip and dip direction respectively. The slope and aspect filter rejected data was analysed to ascertain the potential for "correct" structures to be eliminated from the filtering method (Figure 7.6c). These results show that between ~10-30% of MOI structures rejected during the filtering process are within 20° of field measured structures, accounting for all comparisons. Despite this, the filtering method appears to reject a larger number of erroneous dip directions than dips, with > 50% of dip directions (and dot product comparisons) resulting in differences > 45°.

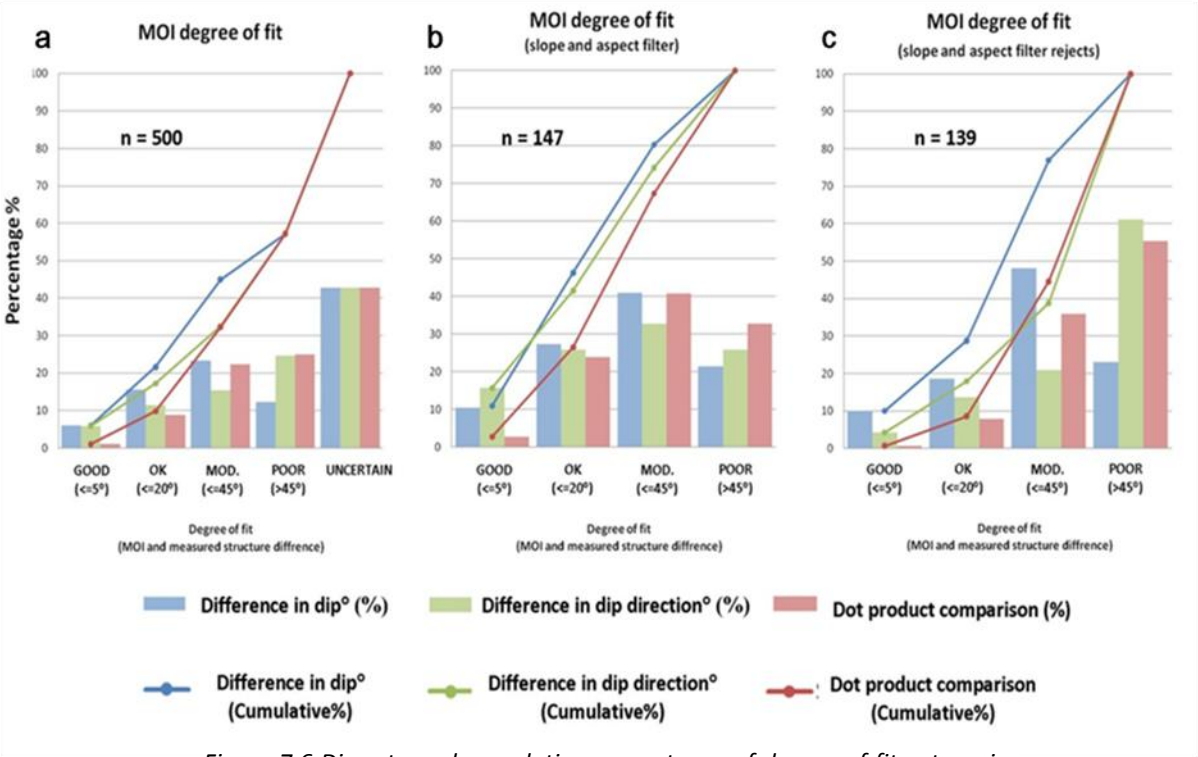

Figure 7.6 Discrete and cumulative percentages of degree of fit categories between measured bedding planes and MOI results, taken from 500 random samples of the nearest point (< 250 m) search method

7.7. Stereonet poles-to-bedding comparison

The study area was divided into generalised geological structural domains (Figure 7.7) based on the iterative analysis of field measurements and interpretive mapping results (see Section 7.8.3). From each domain, measured structures and MOI results were plotted as poles-to-bedding using

equal area stereonets. The stereonet comparison results for all domains are presented in Appendix 10. These include descriptive statistics for both field measurements and poles-to-bedding cluster analysis for each of the datasets. In many areas there were insufficient points available from the field measured data to be useful for comparison. In addition, the generalised domains are most likely crossing structural domain boundaries in several cases. Nevertheless, there are promising results from the stereonet comparisons. For example, plotted poles-to-bedding of field measurements for Domain B (Figure 7.8a) show two general clusters, the first represents bedding orientated ~60→230 and the second ~35→035. The resulting best-fit girdle is orientated 80→137 with a fold hinge plunge and trend (β axis) orientated 10→317. For comparison, the plotted poles-to-bedding of filtered MOI results (Figure 7.8b) again show two general clusters, the first representing orientations of ~60→235 and the second ~35→035. The resulting best-fit girdle for filtered MOI data is orientated 76→141 and with a fold hinge plunge and trend of 14→321. In this case, the field measurements and MOI results are within 5° of each other for all orientations. Figure 7.8c represents poles-to-bedding of the unfiltered MOI results, the best-fit girdles and plunge and trend of the fold axis are comparatively similar to the results of the field measurements and filtered MOI data. However, there is only one large cluster of poles-to-bedding in the unfiltered data suggesting a cylindrical fold geometry, thus obscuring the general contrast between the dip of the fold limbs and the angular geometry of folding in the study area.

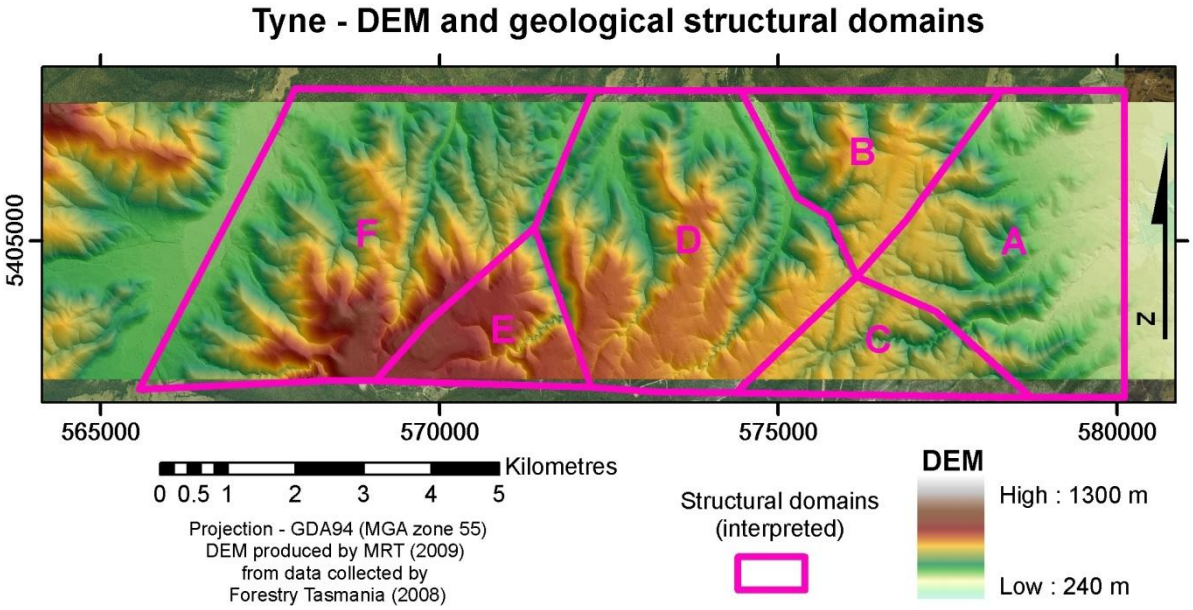

Figure 7.7 Study area DEM overlayed with generalised geological structural domains used for comparing poles to bedding using stereonets of filtered (and unfiltered where applicable) MOI results and field measured bedding planes

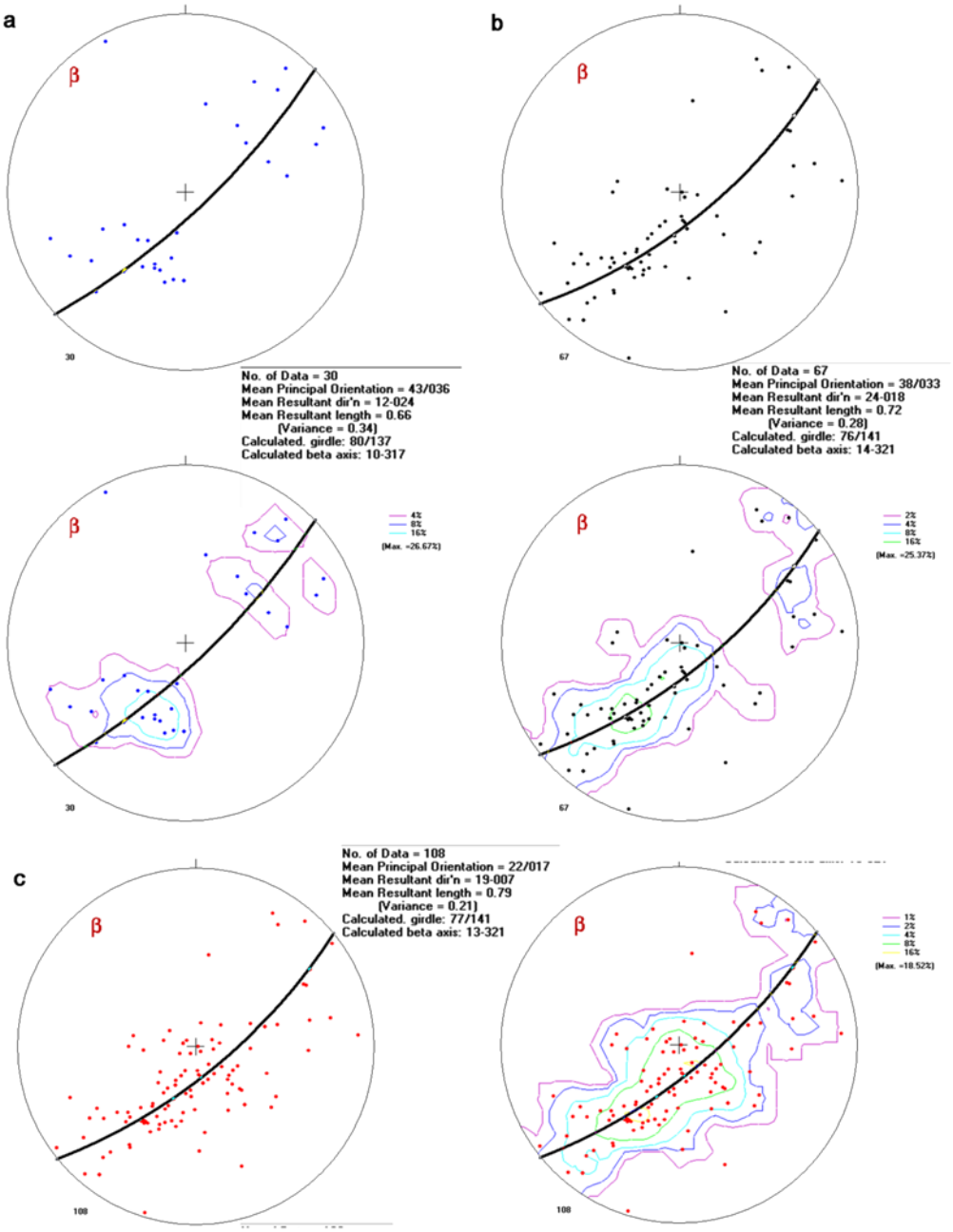

Figure 7.8 Domain B poles to bedding with best-fit girdles (black line), resulting fold hinge trend and plunge (beta axis (β)) and point density (%), a) combined MRT (McClenaghan (comp.), 2007) and field measurements, b) slope and aspect filtered digitised outcrop/lineament MOI results, and c) un-filtered digitised outcrop/lineament MOI results

Poles-to-bedding stereonet comparisons for Domain C presents field measured data showing two general clusters on planes orientated 50→215 and 35→065 (Figure 7.9a), with a best-fit fold hinge orientation of 15→135. In contrast, the filtered MOI results (Figure 7.9b) show a broad scatter of points with several clusters generating a best-fit fold hinge orientation of 14→149, which is not dissimilar to the measured data within the same domain. Despite this, it is visually apparent that either the filtered MOI results are responding to different structural domains not adequately measured in the field or spurious MOI results are being plotted.

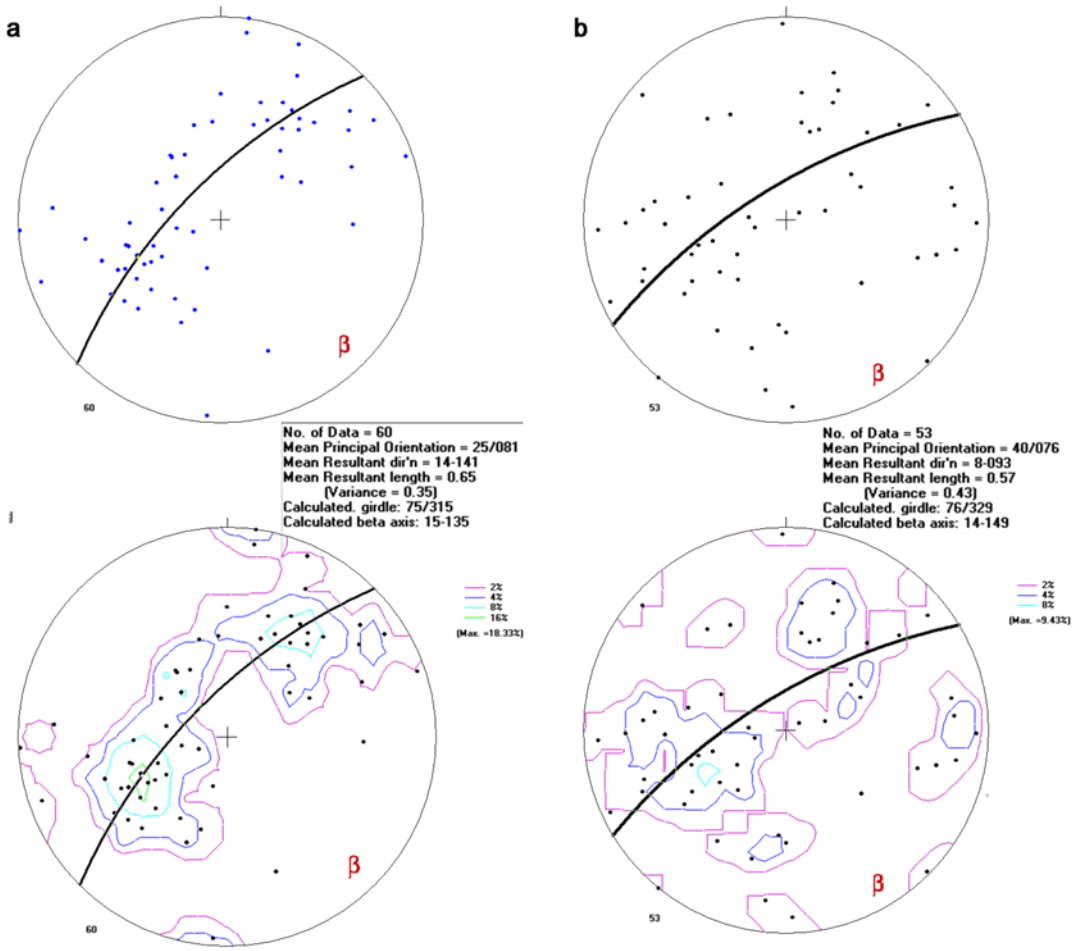

Figure 7.9 Domain C poles to bedding with best-fit girdles (black line), resulting fold hinge trend and plunge (beta axis (β)) and point density (%), a) combined MRT (McClenaghan (comp.), 2007) and field measurements, and b) slope and aspect filtered digitised outcrop/lineament MOI results

7.8. Interpreting geological structures

In many cases, there were insufficient field measured structural data for reliable comparisons with the filtered MOI results or for wider interpretation of geological structures. Nevertheless, after careful examination of structures traversed in the field, combined with an understanding of their expression in the enhanced curvature images, a series of "typical" geological structures have been identified within the study area. Examples of "typical" structures, such as anticlines, synclines and faults are presented in this section in an attempt to justify the wider interpretation of these structures in areas where field measurements are sparse.

7.8.1. Observed geological structures

Figure 7.10 graphically depicts a small area of field measurements, filtered MOI results and an enhanced curvature image representing an anticline and syncline. The corresponding interpreted

geological cross-section and profile of surface curvature accompanies the plan view. Using combined field measurements, plausible filtered MOI results and surface curvature, two open upright folds are evident. The most striking feature of the enhanced curvature image are the exposed sand rich beds (seen as positive/convex surface curvature) bending acutely as they cross fold axial traces. Several kinks in the eastern limb of the anticline are also evident, both from the outcrop traces (formlines) and structural data.

7.8.2. Interpreted geological structures

Figures 7.11a and 7.11b present syncline and anticline interpretations based on the subtle convergence (syncline) and divergence (anticline) of convex surface curvature features and filtered MOI results. It is important to take into account the dominant landforms represented when interpreting these structures. In the examples provided, hillcrest and ridge features are apparent, with their main axis parallel to the trend of the axial trace (i.e. NNW). If the outcrop traces were observed within a valley with its axis parallel to the trend of the axial trace then, convergent features would indicate an anticline and divergent features a syncline. The use of the terms anticline and syncline are conducted with an element of interpretive faith, based on the filtered MOI results and knowledge that the study area predominantly contains upright chevron fold geometries (Taheri & Findlay, 1992; Keele, 1994; Reed, 2004).

Figure 7.12 provides an example fault interpretation. This interpretation is partially based on the offset of fold axial traces, and on the presence of a clearly defined linear valley/channel landform. As discussed in Chapter 2, faults can be characterised by fracture zones and planes of weakness within rocks, encouraging the development of topographic lows. Not featured in Figure 7.12 are a series of adjacent parallel linear valley landforms to the north and south, which also display fold axial trace offset. Both Goscombe & Findlay (1989) and Reed (2004) have identified meso and mega-scale kinking offset throughout the study area trending in preferred orientations. Sinistral kink boundaries trend toward the N-NE and dextral kink boundaries toward the E-SE. Reed (2004) adds that the dextral kinking event appears to predate the sinistral event. Thus, the orientation of the main valley axis can be an indicator of the probable direction of fault displacement if obvious offset of outcrop/lineaments or fold axial traces are not identified.

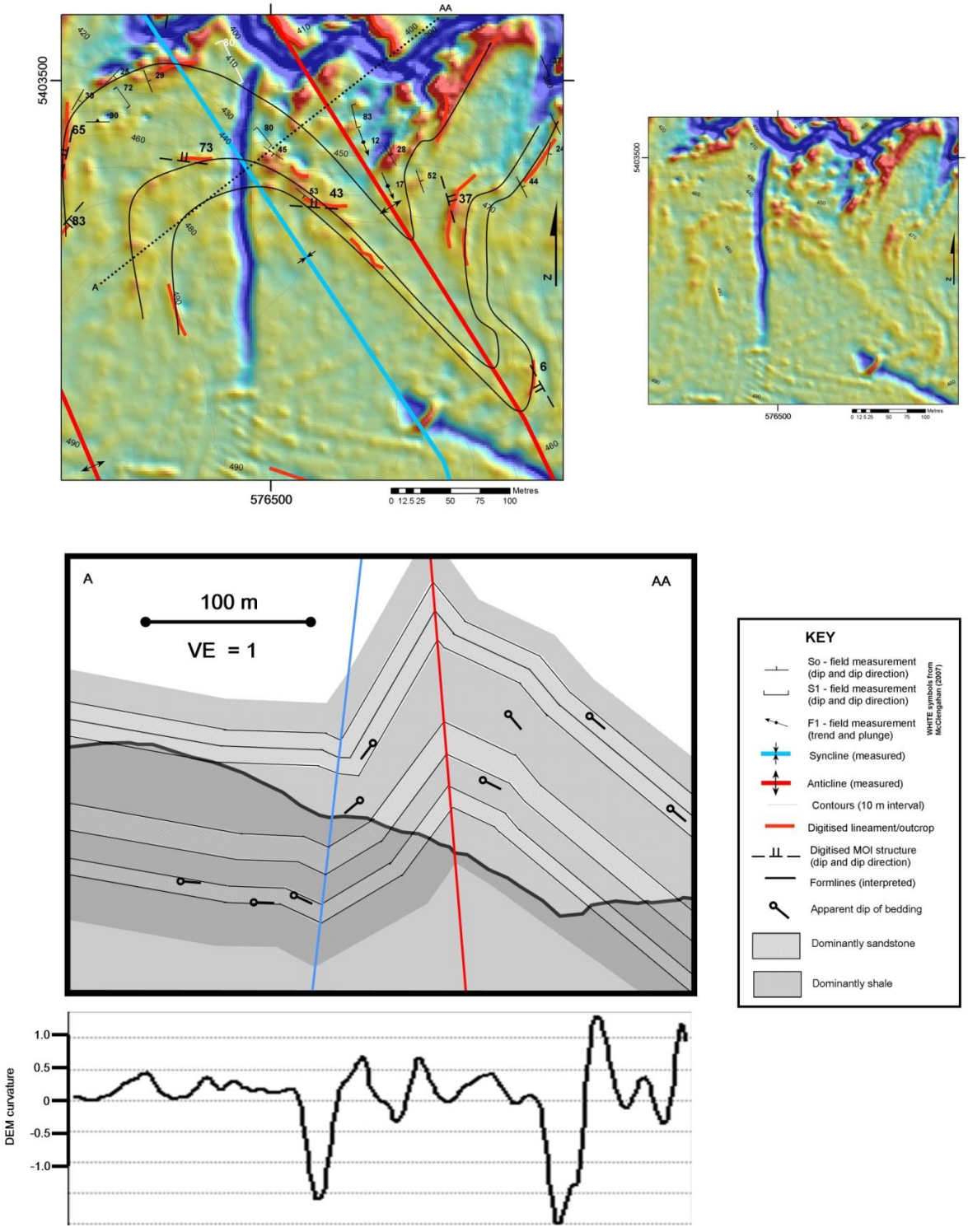

Figure 7.10 Combined field data, filtered MOI results and enhanced curvature image (zm/m2) representing observed anticline and syncline geological structures including interpreted geological cross-section and surface curvature profiles (zm/m2), the image on the right shows a "clean" version of the interpreted image

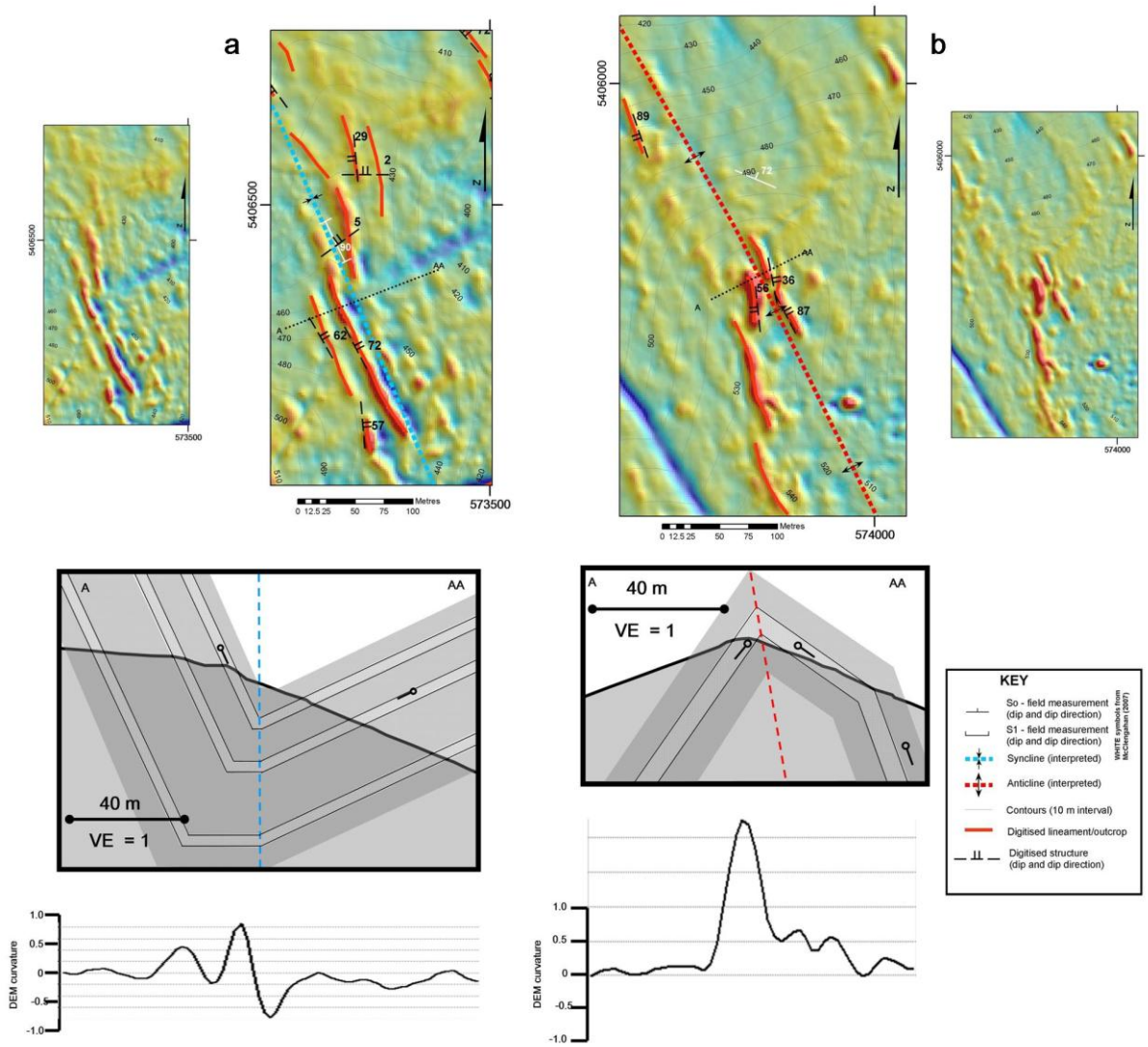

Figure 7.11 Interpreted axial traces and surfaces from a combination of filtered MOI results and features in the enhanced curvature images (zm/m2), a) syncline, and b) anticline, the smaller figures represent "clean" versions of interpreted images

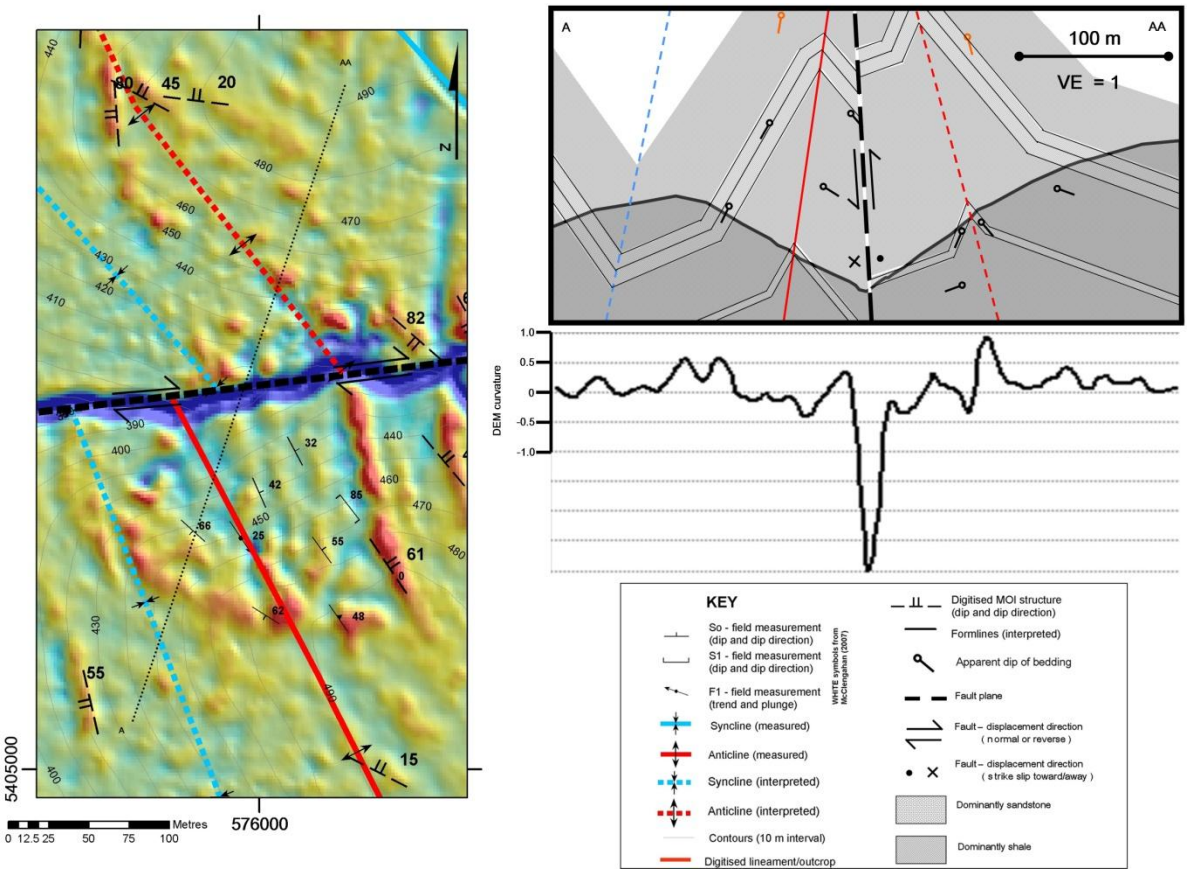

Figure 7.12 Interpretation of a dextral reverse fault, using a combination of measured field data, MOI results, fold axial trace offset and concave landform expression

7.8.3. Interpretive mapping

The interpretive examples presented in Section 7.8.2, have provided the basis for the construction of the interpretive geological structural map and two cross-sections covering the study area. The map has been divided into two parts, Tyne-west (Figure 7.13) and Tyne-east (Figure 7.14). These maps were drawn at a scale of 1:20,000. The cross-sections (Figure 7.15) have been generated using a combination of field measured structures, plausible MOI results and interpretations developed from the inferred relationship between landforms and geological phenomena.

There is a relationship between regional scale landscape geometry and geological structures. For example, the Main Slide fault displays dextral reverse movement (Reed, 2004) trends NNW and coincides with a prominent linear valley. East of the Main Slide, a fault with sinistral offset trends SW and is interpreted to converge with the Main Slide forming a wedge. Moving westward across the study area there are at least two or three more similar wedge shaped features, interpreted as analogous structures to the Main Slide based on their geometry (i.e. flanked by a dextral reverse fault to the west and sinistral fault the east). These structures have principally been identified from coincident linear drainage patterns trending NW. Dextral faults appear to be cross-cut by

generally NNE trending sinistral faults. This observation is in agreement with Keele (1994) and Reed (2004).

Interpreted fold axial traces have an average wavelength of ~100-200 m and trend in a NNW-NW orientation. However, as fold axes approach NW trending dextral reverse faults from the east their wavelengths decrease. This is in contrast to the abrupt decrease in fold wavelengths west of NW trending faults. In Tyne-east, NE verging folds change to SW verging folds across a regional scale syncline east of the Main Slide. West of the Main Slide, a complexly folded (refolded?) regional scale anticline defines another change in vergence; this time from SW to NE. Regional fold wavelength is ~2 km. In general, fold trends in the Tyne-east map are NNW oriented, while in Tyne-west folds trend increasing NW coinciding with an overall decrease in fold wavelength.

The geological cross sections contain inferred lithological boundaries between shale dominated and sand dominated units. The shale rich unit is inferred to be ~ 300 thick in cross section. Due to the lack of distinctive marker beds it was difficult to constrain lithological boundaries. Therefore, the inferred contacts are based on generalised lithological observations. It is unclear if the shale dominated unit depicted in both cross-sections are in actual fact the same unit. The post Carboniferous unconformity surface and overlying Permian sandstones have not been included in the cross-sections.

An attempt has been made to honour field measurements and selected MOI structural data. This includes the apparent dip of fold axes (taken from cleavage measurements) and apparent dip of bedding planes The dominant regional structures in the cross-sections are steeply dipping NE side up thrust faults. Although the dip of the thrust faults has been estimated from the curvilinearity of channel landforms. Despite this, these structures are coincident with the observations on fault geometry discussed previously. Maximum displacement across the thrust faults is ~500 m. However, due to the lack of lithological constraints it is unclear if the displacement observations are valid.

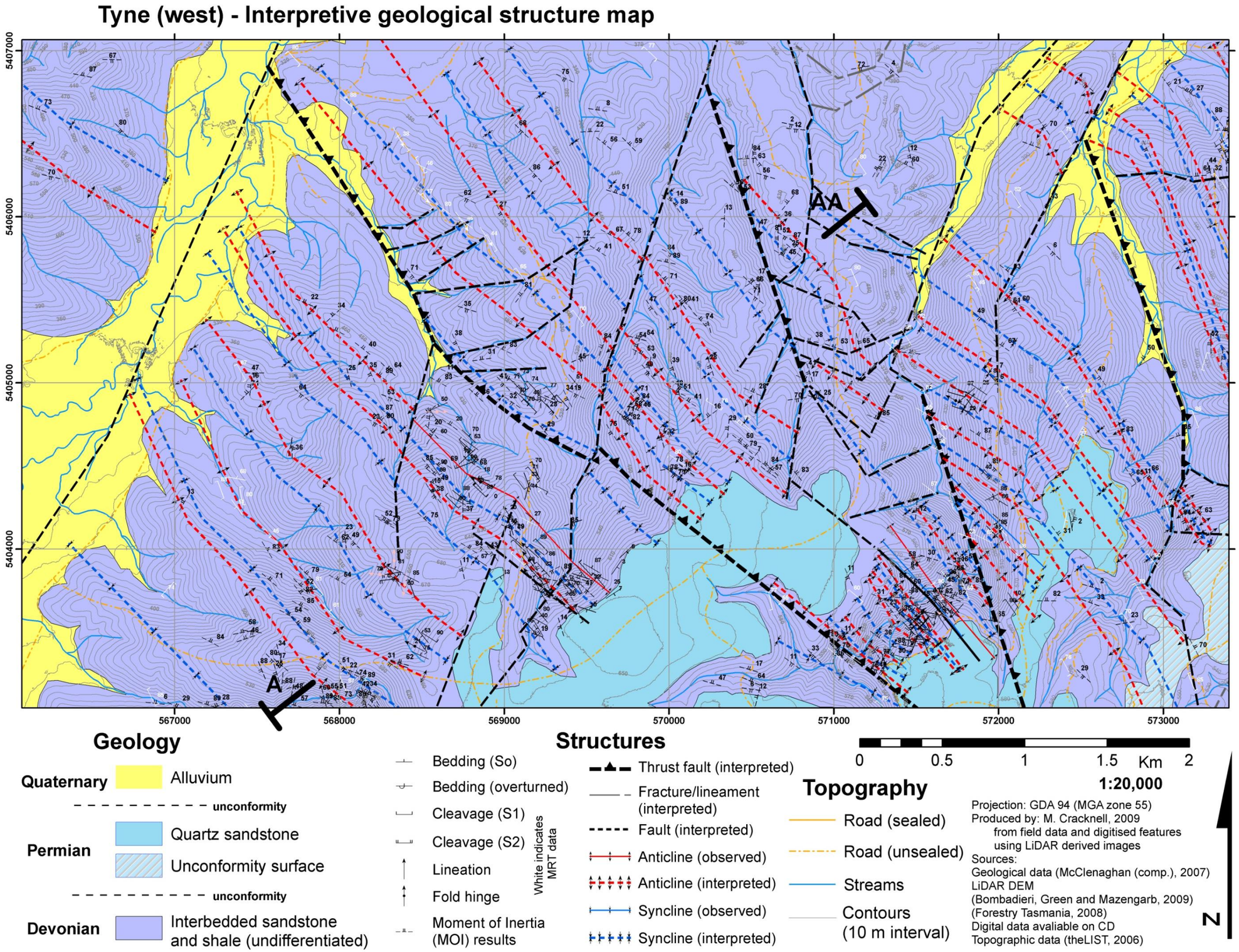

Figure 7.13 Tyne (west) – Interpretive geological structure map, see Figure 7.15 for cross-section A-AA

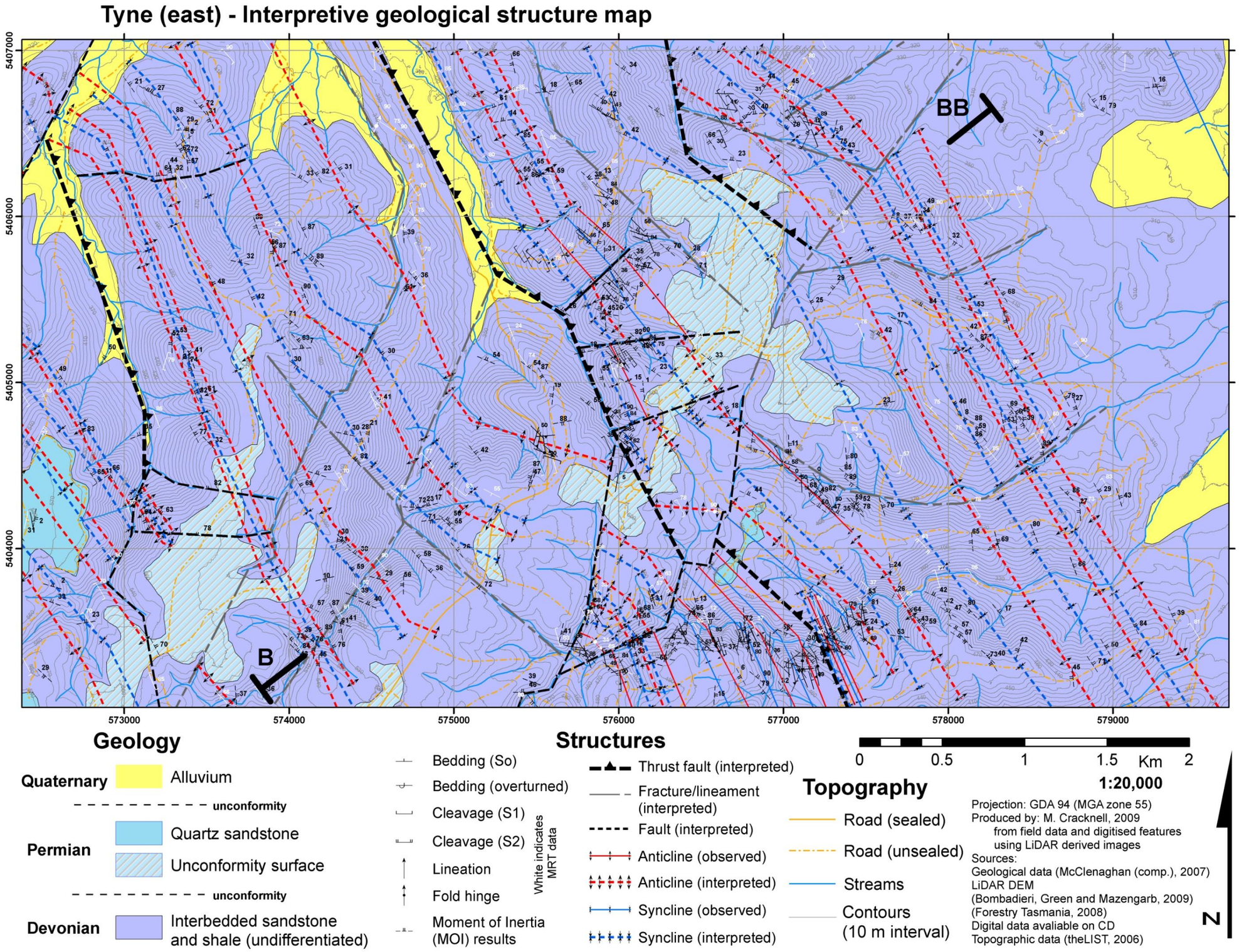

Figure 7.14 Tyne (east) – Interpretive geological structure map, see Figure 7.15 for cross-section B-BB

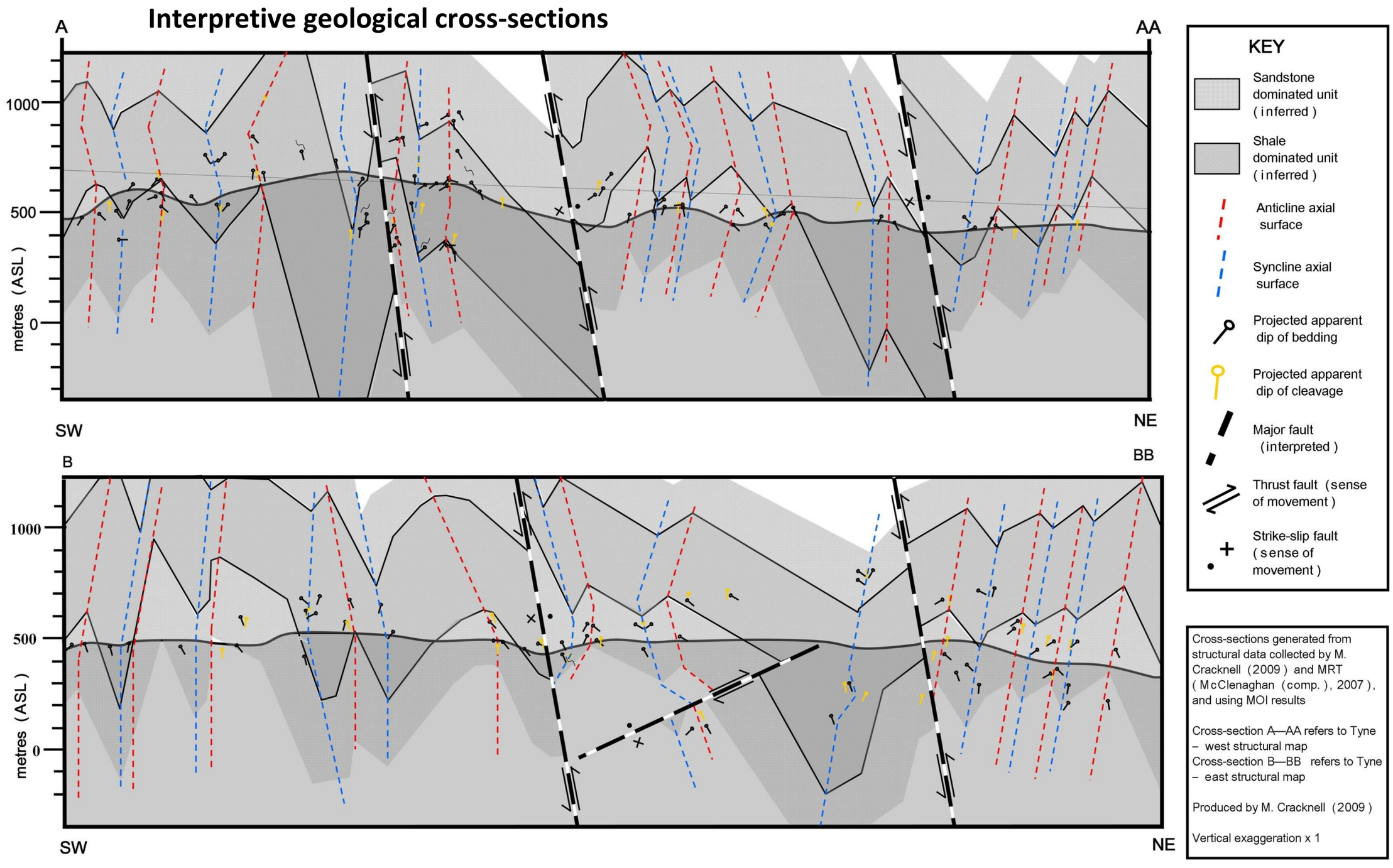

Figure 7.15 Interpretive geological cross-sections, refer to Figure 7.13 for location of section A-AA and Figure 7.14 for location of section B-BB

8. Review and discussion

The following discussion provides an assessment of the uses, advantages and limitations regarding the techniques presented and methods developed. In addition, avenues for future research are discussed. Focus is placed on: landforms and their relationships to geological phenomena; the perceived advantages and limitations regarding the use of LiDAR data; and an assessment of the methods developed to enhance, select and extract geological features from high resolution DEMs. This chapter closes with an appraisal of the MOI results and subsequent site specific geological structural interpretations.

8.1. Geological features and landforms

The majority of geological features manually identified within the study area were expressed as convex landforms (i.e. with positive curvature) in the enhanced curvature images. Convex landforms almost exclusively resulted from the exposure of sandstone dominant lithologies. Where discrete interbeds of less resistant shales accompanied more resistant quartz rich sandstones, geological features were most obvious. This scenario often created alternating concave and convex surface curvature perpendicular to the general strike of bedding. Field work observations, in conjunction with the MOI results suggest that interbedded sedimentary sequences, comprised of lithologies with contrasting resistance to the effects of weathering and erosion, hold the greatest potential for successful remote sensing of local scale bedding plane orientations.

Local scale concave landforms were often subtle in their expression, limited in their extent and therefore difficult to confidently identify. In contrast, regional scale drainage systems were expressed as obvious and continuous linear concave features. Regional concave features, have in many cases been interpreted as major fracture zones and faults, based primarily on the assumption that accelerated weathering and erosion of geological materials is spatially related to zones of brittle failure in rocks (Easterbrook, 1999; Wladis, 1999; Pluijm & Marshak, 2004; Nyborg, Berglund & Triumf, 2007). Despite this, careful consideration of the developmental controls on linear drainage patterns must be employed when interpreting faults, as these may not always represent structures present within the geology currently exposed at the Earth's surface. For example, superposed drainage initially develops within overlying stratigraphic sequences and continues to maintain its general location and orientation after erosion has exposed the underlying stratigraphy (Easterbrook, 1999). In addition, faults and fracture zones may not always

develop into concave landforms. For instance, quartz veins precipitated within faults and fractures are likely to produce resistant landforms expressed as convex features. The distinction between the two will be difficult to determine.

The Permian unconformity and overlying quartz rich sandstone within the study area was characterised by a distinctive horizontal plateau bounded with steep escarpments up to 10 m in height (Figure 8.1). The contrasting resistance to weathering and erosion between the overlying quartz sandstones and underlying interbedded lithic sandstones and shales has provided a means to identifying and interpreting this unconformable contact (Easterbrook, 1999; Maukisch *et al.*, 2007). In all cases, the MOI results predicted shallow dips of less than 5°and dip directions toward the east for the beds overlying the unconformity.

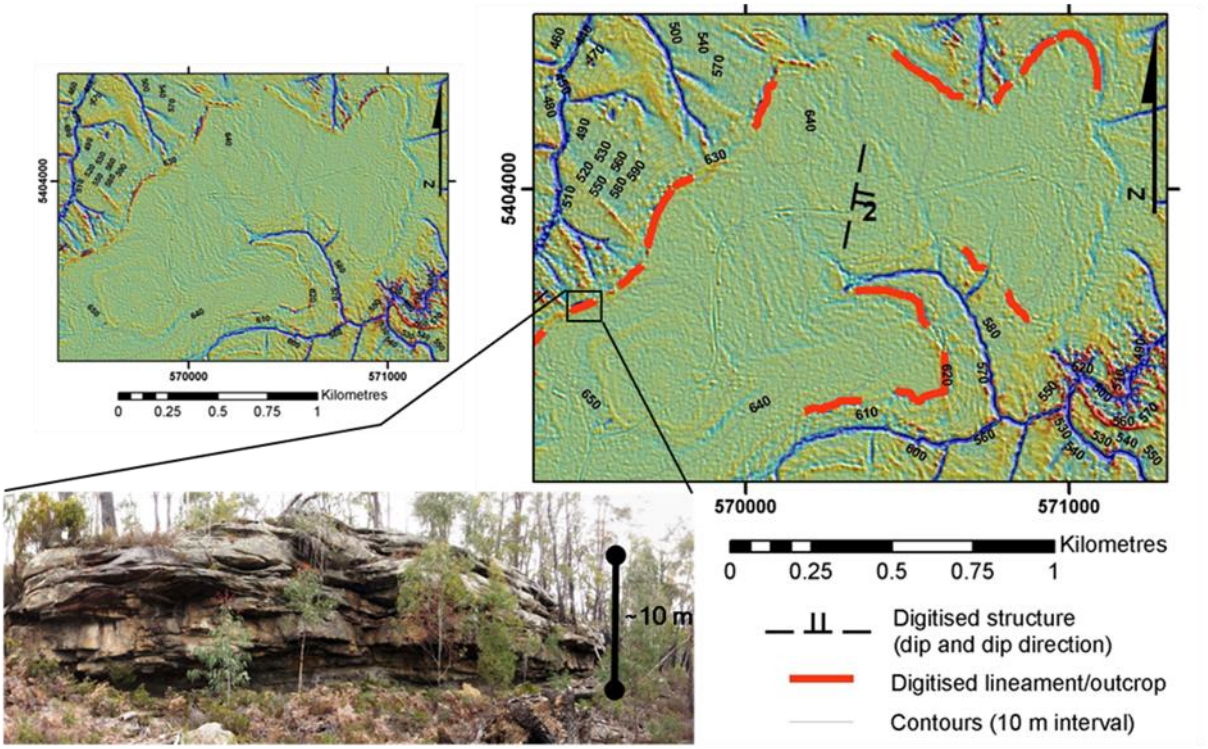

Figure 8.1 Enhanced curvature image and field example of an unconformity overlain by resistant quartz sandstones

The Earth's surface does not solely consist of bare rock surfaces but a combination of eroded rock materials deposited as sediments such as alluvium, or materials currently in transit such as colluvium (Easterbrook, 1999). Quaternary alluvial sediments predominantly fill valley floors posing problems for the approach used in this project as they totally obscure bedrock surfaces. It is highly unlikely that remote sensing local scale structural measurements in areas mantled by alluvial sediments can be achieved. This is also true of field observations, except where river channels have incised into unconsolidated sediments and exposed bedrock surfaces.

In the field, colluvium was usually observed as loose clasts situated immediately down slope from adjacent outcrops. Angular boulders and cobbles appeared to be sourced from more resistant lithologies, whereas small fragments and shards were derived from less resistant lithologies. Often outcrop was inferred from the existence of a linear alignment of angular boulders, interpreted to conceal exposures of sandstone. It is possible that in these situations, enhanced curvature images may provide a means of measuring the orientation of concealed bedrock exposures, based purely on subtle contrasts in the curvature of the landscape. Slight depressions between sandstone outcrops may also suggest that a change in lithology had occurred. Often these depressions contained small fragments and shards of shale providing evidence for this interpretation. It is feasible that subtle linear depressions can be digitised to obtain bedding orientations. Nevertheless, care must be taken when interpreting these results as the less resistant nature of the lithologies will most likely develop into features with reduced definition, often filled with slope derived materials.

8.2. LiDAR, high resolution DEMs and geological applications

LiDAR provides researchers with dense irregularly spaced high precision 3D point data for the production of high resolution elevation models for terrain analysis. As discussed in Chapter 3, the majority of previous earth science applications of LiDAR derived high resolution DEMs has investigated geological hazard mapping and assessment (Carter *et al.*, 2001; Haugerud *et al.*, 2003; Chan *et al.*, 2007). These studies have concentrated on geomorphological aspects of hazard mapping, such as the detection of landslides and active fault scarps. However, Carter *et al.* (2001), Haugerud *et al.* (2003) and Chan *et al.* (2007) all conclude that the ability of LiDAR systems to penetrate vegetation canopies and image bare Earth surfaces opens a wide range of possibilities for innovative earth science applications, not previously achievable using other remote sensing datasets such as aerial photography.

Unfortunately, the effects human induced landscape modifications and reduced penetration of laser pulses due to thick vegetation must be taken into consideration when using LiDAR data for geological applications. Roads, forestry operations and dam walls have all been identified within the study area from the DEM and enhanced curvature image. Artificial landscape features have been ignored when manually selecting geological features but can reduce an interpreter's ability to identify and select true geological phenomena (Haugerud *et al.*, 2003; Chan *et al.*, 2007). Thick vegetation can intercept the majority of laser energy before reaching the Earth's surface, resulting in a decreased ground return point density (Haugerud *et al.*, 2003; Jensen, 2007). In an attempt to limit the effect of vegetation on ground point density, Wallace, Morris & Howarth (2006) used

LiDAR data collected in the northern hemisphere during leaf-off conditions. However, very few species of trees in Tasmania are deciduous eliminating the possibility of collecting LiDAR data under such conditions. Preliminary observations of high resolution DEMs of areas in western Tasmania, where thick rainforest vegetation is abundant, suggest that both reduced point density and misclassified ground returns (i.e. vegetation returns classified as ground returns) will pose problems for the remote interpretation of local scale geological structures (D. Green pers. comm., Sept 2009).

Several issues, with respect to processing artefacts within the original raw LiDAR data, have been identified and their origins discussed. Low pass filtering and resampling of the original 0.5 m resolution DEM were carried out in an attempt to reduce the impact of artefacts when manually selecting geological features. The smoothing or resampling approach to artefact elimination has a negative effect on feature identification as it reduces the resolution of the DEM and thus limits the potential scale of observation. In an alternative approach, Blakely *et al.* (2004) marked any identified artefacts so that they were not considered further when identifying geological features. Processing artefacts will reduce the reliability of automated approaches to geological feature extraction.

As discussed in the literature review accompanying this thesis (Appendix 11), LiDAR reflection backscattered intensity may in the future prove to be useful for earth science applications. Laser backscatter intensity has the potential to assist the identification, selection and interpretation of geological features based on their reflectance characteristics.

8.3. Review of developmental methodology and results

The outcrop/lineament identification and selection methods presented have primarily been based on subjective interpretation of plausible geological features. As Raghavan, Wadatsumi & Masumoto (1993), Wladis (1999) and Argialas & Mavrantza (2004) point out, manual selection methods have the potential to introduce bias and create less reproducible results than automated or objective selection methods. Several iterations were performed when manually digitising geological features and different results were obtained every time. The difference in results using manual digital image interpretation methods highlights the issues described above and the apparent sensitivity of derived orientation data to small positional errors. The subjective approach presented was deemed necessary as the automated techniques investigated resulted in overall lineament trend directional bias. See Appendix 2 for a summary of the automated lineament detection methods developed and preliminary results

A python program was written that automates the estimation of best-fit planes from 3D georeferenced points using the methodology suggested by Fernández (2005) (Moment-of-Inertia (MOI) analysis). This program is efficient and accurate in its calculation of best-fit planes provided that points used to generate the planes are representative of the plane in question. Assessment of the automated plane extraction algorithm results (using synthetic data) showed that the reliability of this method diminished where outcrop traces were limited in their length. These findings are in agreement with the M and K thresholds proposed by Fernández (2005) for solution reliability. It is interesting that all the M values obtained from the MOI results presented in this thesis were within the advised threshold limits, suggesting that the points used to fit planes were co-planar resulting in high degree-of-fit. Contrast this with the majority of K values outside advised threshold limits (~90%); suggesting most points selected from a particular feature were effectively co-linear (i.e. they represent a line). From these observations it can be concluded that most of the features used to generate planes were of limited length and positioned across a single hillslope flanks (i.e. the digitised features did not cross drainage divides). This does not mean that the results presented are invalid, only that further investigations are required into the specific characteristics of landforms and their relationship to geological features within the study area.

The methods developed for digitising lineaments, obtaining best-fit planes and their analysis are separate stand-alone applications and time consuming to conduct. All features are initially selected in a GIS environment from an enhanced curvature image, exported and entered into the MOI algorithm, then imported into a GIS environment for analysis, filtering and display. Currently, there are no avenues for the “real time” interactive assessment of results as features are selected. However, as the MOI algorithm has been written in python code and ArcGIS command prompt functions also run via python code (ESRI, 2008) it may be possible to link the two via a Graphical User Interface (GUI), allowing the user to assess MOI results while selecting features. Advantages to this approach would include: a reduced reliance on the qualitative assessment of feature reliability; increased feature selection repeatability; and an improved interactive workflow environment.

8.4. Assessment of structural interpretations

The spatial relationships of bedding plane orientations (both observed in the field and remotely sensed) in conjunction with manually identified fold closures, have assisted in interpreting the location and trend of fold axial traces. However, an obvious limitation to structural mapping using the MOI results is the fact that only bedding planes have been quantified and facing cannot be determined. Also, the lack of cleavage and lineation measurements (i.e. bedding cleavage

intersections) limits the use of high resolution DEMs for structural mapping. Where fold hinge closures can be identified it may be possible to define the trend *and* plunge of a fold. To achieve this one must simply measure the locations and difference in elevation between two fold closures representing the same fold. This will enable the plunge and trend (with respect to north) of a line representing an axial trace to be calculated. Cleavage, unlike fold hinge trend and plunge is defined as a plane and requires at least three points to calculate its orientation.

Structural mapping is of vital importance to assist in the identification of prospective gold mineralisation in the vicinity of the study area (Reed, 2004). In general, outcrop exposures are poor throughout the Mathinna Group and most field data is collected from road cuttings and trenches (Richardson & Roach, 1994; Reed, 2004). Therefore, remotely sensed structural data has the potential to compliment field based observations and assist in developing models for the location of gold mineralisation. Despite this, it is still important to conduct field based observations for the collection of lithological observations, cleavage and other structural measurement, and to validate any MOI results.

9. Conclusions

An intimate relationship exists between the morphology of the landscape and near surface geological phenomena. Both lithological contrasts and geological structural features combine to influence the geometry of the Earth's surface. This project has shown that local topographic discontinuities (i.e. rapid changes in elevation) identified in high resolution Digital Elevation Models (DEMs) derived from Light Detection and Ranging (LiDAR) data can be used as a proxies for quantifying bedding plane orientations.

Both automated and manual methods were developed for the enhancement, selection, extraction and association of attributes to geological features from high resolution DEMs. Enhancement of topographic discontinuities was based on calculating the 2nd partial derivative (curvature) of a DEM and automated using LandSerf software. Automated methods for feature extraction were trialled but were ineffective and manual methods were used for the selection and extraction of geological features from curvature images within a GIS environment (ArcGIS). Best-fit planes have been calculated from three-dimensional (3D) georeferenced points representing selected geological features using the Moment of Inertia (MOI) algorithm developed by Fernández (2005). The MOI algorithm was automated using a script written in python. Although the methodology presented is effective, additional effort needs to be committed to automate the process within a single software environment to facilitate interactive data exploration

Comparisons between bedding plane field measurements and the MOI results show that bedding orientations can be remotely interpreted from LIDAR DEM data with a reasonable level of confidence in some structural domains. However, care must be taken when manually selecting and digitising target features. Small variations in the interpreted position of a feature can result in large changes in calculated orientation. The slope and aspect of the topography, not necessarily related to geological structures, is easily defined from selected features of limited length and those that do not cross drainage divides.

Field observations and the qualitative assessment of local and regional scale landform geometry have provided a foundation for the interpretation of geological structures. However, further work is required to validate the structural interpretations presented in this thesis, to apply these techniques to different geological terranes and to develop automated methods for the selection and extraction of geological features.

The use of the high resolution DEMs generated from LiDAR data to assist geological structural mapping is currently in its infancy. Despite this, the findings presented as part of this thesis suggest that remote sensing local scale geological structures compliments field based observations. This technology has the potential to provide geoscientists with innovative methods for improving our understanding of local scale geological phenomena.

References

Argialas, D. P. & Mavrantza, D. O., 2004: 'Comparison of edge detection and Hough Transform techniques for the extraction of geologic features', *The International Archives of the Photogrammetry, Remote Sensing and Spatial Information Sciences*, **Vol. 34, Part XXX**, p. 6.

Arnold, N. S., Rees, W. G., Devereux, B. J. & Amable, G. S., 2006: 'Evaluating the potential of high resolution airborne LiDAR data in glaciology', *International Journal of Remote Sensing*, **Vol. 27, no. 6**, pp. 1233-1251.

Baltsavias, E. P., 1999: 'Airborne laser scanning: basic relations and formulas', *ISPRS Journal of Photogrammetry and Remote Sensing*, **Vol. 54, no. 2-3**, pp. 199-214.

Bater, C. W. & Coops, N. C., 2009: 'Evaluating error associated with LiDAR-derived DEM interpolation', *Computers & Geosciences*, Vol. 35, no. 2, pp. 289-300.

Blakely, R. J., Sherrod, B. L., Wells, R. E., Weaver, C. S., McCormack, D. H., Troost, K. G. & Haugerud, R. A., 2004: *The Cottage Lake aeromagnetic lineament: A possible onshore extension of the Southern Whidbey Island Fault, Washington*, Open-File Report 2004-1204, U.S. Geological Survey, p. 60.

Bombadieri, D., Green, D. & Mazengarb, C. 2009: *Tyne – DEM 0.5 m resolution, 1:7000*, Mineral Resources Tasmania, Rosny Park, Tasmania.

Carter, W., Shrestha, R., Tuell, G., Bloomquist, D. & Sartori, M., 2001: 'Airborne laser swath mapping shines new light on Earth's topography', *Eos, Transactions, American Geophysical Union*, **Vol. 82, no. 46**, pp. 549-555.

Chan, Y. C., Chen, Y. G., Shih, T. Y. & Huang, C., 2007: 'Characterizing the Hsincheng active fault in northern Taiwan using airborne LiDAR data: Detailed geomorphic features and their structural implications', *Journal of Asian Earth Sciences*, **Vol. 31, no. 3**, pp. 303-316.

Charlton, M. E., Large, A. R. G. & Fuller, I. C., 2003: 'Application of airborne LiDAR in river environments: the River Coquet, Northumberland, UK', *Earth Surface Processes and Landforms*, **Vol. 28, no. 3**, pp. 299-306.

Chen, L. C., Teo, T. A., Kuo, C. Y. & Rau, J. Y., 2008: 'Shaping Polyhedral Buildings by the Fusion of Vector Maps and LiDAR Point Clouds', *Photogrammetric Engineering & Remote Sensing*, **Vol. 74, no. 9**, pp. 1147-1157.

Clark, C. D. & Wilson, C., 1994: 'Spatial analysis of lineaments', *Computers & Geoscience*, **Vol. 20, no. 7-8**, pp. 1237-1258.

Cooper, G. R. J., 2006: 'Obtaining dip and susceptibility information from Euler deconvolution using the Hough transform', *Computers & Geosciences*, **Vol. 32, no. 10**, pp. 1592-1599.

Easterbrook, D. J., 1999: *Surface Processes and Landforms*, 2nd edition, Prentice Hall, Upper Saddle River, New Jersey, p. 546.

Eaton, D. & Vasudevan, K., 2004: 'Skeletonization of aeromagnetic data', *Geophysics*, **Vol. 69, no. 2**, pp. 478-488.

Ekneligoda, T. C. & Henkel, H., 2006: 'The spacing calculator software-A Visual Basic program to calculate spatial properties of lineaments', *Computers & Geosciences*, **Vol. 32, no. 4**, pp. 542-553.

Environmental Systems Research Institute (cited as ESRI), 2001: *ARC/INFO Help*, Environmental Systems Research Institute, Inc.

Environmental Systems Research Institute (cited as ESRI), 2008: *ArcGIS Desktop Help*, 9.3, Environmental Systems Research Institute, Inc.

Evans, J. S. & Hudak, A. T., 2007: 'A Multiscale Curvature Algorithm for Classifying Discrete Return LiDAR in Forested Environments', *IEEE Transactions on Geoscience and Remote Sensing*, **Vol. 45, no. 4**, pp. 1029-1038.

Fernández, O., 2005: 'Obtaining a best-fitting plane through 3D georeferenced data', *Journal of Structural Geology*, **Vol. 27, no. 5**, pp. 855-858.

Fernández, O., Jones, S., Armstrong, N., Johnson, G., Ravaglia, A. & Munoz, J. A., 2009: 'Automated tools within workflows for 3D structural construction from surface and subsurface data', *Geoinformatica*, **Vol. 13, no. 3**, pp. 291-304.

Filin, S., 2004: 'Surface classification from airborne laser scanning data', *Computers & Geosciences*, **Vol. 30, no. 9-10**, pp. 1033-1041.

Filin, S. & Pfeifer, N., 2006: 'Segmentation of airborne laser scanning data using a slope adaptive neighborhood', *ISPRS Journal of Photogrammetry and Remote Sensing*, **Vol. 60, no. 2**, pp. 71-80.

Frangos, W., 2008: *Three-Point Problem by Simultaneous Linear Equations,* Science Education Resource Center, Carleton College, last updated 8 Aug 2008, viewed 13 May 2009, <http://serc.carleton.edu/quantskills/workshopactivities/three_point.html>.

French, J. R., 2003: 'Airborne LiDAR in support of geomorphological and hydraulic modelling', *Earth Surface Processes and Landforms*, **Vol. 28, no. 3**, pp. 321-335.

GahGah, M. M., Akhir, J. M., Rafek, A. G. M. & Abdullah, I., 2007: 'Correlation of geological discontinuities with remote sensing lineaments: case study from Cameron Highlands, Pahang-Gua Musang, Kelantan', *Proceedings of the 28th AARS Conference, November 12-16, 2007*, Asian Association on Remote Sensing, Kuala Lumpur, Malaysia, <www.aars-acrs.org/acrs/proceeding/ACRS2007/Papers/PS2.G6.3.pdf>.

Gloaguen, R., Marpu, P. R. & Niemeyer, I., 2007: 'Automatic extraction of faults and fractal analysis from remote sensing data', *Nonlinear Processes in Geophysics*, **Vol. 14,** pp. 131-138.

Goscombe, B. D. & Findlay, R. H., 1989: *Mega-kinking in the Mathinna Beds, north-east Tasmania*, 1989/42 (unpublished report), Tasmanian Department of Mines, Rosny Park, Tasmania, p. 21.

Goscombe, B. D., Findlay, R. H., McClenaghan, M. P. & Everard, J., 1994: 'Multi-scale kinking in northeast Tasmania: crustal shortening at shallow crustal levels', *Journal of Structural Geology*, **Vol. 16, no. 8**, pp. 1077-1092.

Goscombe, B. D., McClenaghan, M. P. & Everard, J. L., 1992: *Contact metamorphism of the Mathinna Beds and the depth of crustal residence during mega-kinking in northeast Tasmania*, 1992/34, Tasmanian Department of Mines, Rosny Park, Tasmania, p. 25.

Graniczny, M., Mizerski, W. & Piatkowska, A., 2005: 'Lineaments interpreted at the radar images and the digital elevation model within the Palaeozoic rocks of the Holy Cross Mts.' *Przeglad Geologiczny*, **Vol. 53, no. 10/2**, pp. 949-955.

Haugerud, R. A., Harding, D. J., Johnson, S. Y., Harless, J. L., Weaver, C. S. & Sherrod, B. L., 2003: 'High-Resolution LiDAR Topography of the Puget Lowland, Washington-A Bonanza for Earth Science', *GSA Today*, **Vol. 13, no. 6**, pp. 4-10.

Hodgson, M. E. & Bresnahan, P., 2004: 'Accuracy of Airborne LiDAR-Derived Elevation: Empirical Assessment and Error Budget', *Photogrammetric Engineering & Remote Sensing*, **Vol. 70, no. 3**, pp. 331-339.

Hopkinson, C., 2006: 'The Influence of LiDAR Acquisition Settings on Canopy Penetration and Laser Pulse Return Characteristics', Geoscience and Remote Sensing Symposium, 2006, IEEE International Conference, Denver, Colorado, July 2006, pp. 2420-2423.

Hyun-chong, C., Kampa, K. & Slatton, K. C., 2007: 'Morphological segmentation of LiDAR Digital Elevation Models to extract stream channels in forested terrain', Geoscience and Remote Sensing Symposium, 2007, IEEE International Conference, Barcelona, Spain, July 2007, pp. 3182-3185.

Ingenieur-Gesellschaft fuer Interfaces mbH (cited as IGI mbH), 2009: 'LiteMapper 5600 specifications', p. 2, <http://www.litemapper.eu/downloads/brochures/IGI_LiteMapper5600_specs.pdf>.

Isenburg, M. & Shewchuk, J. 2009: *Lastools*, <http://www.cs.unc.edu/~isenburg/lastools/>.

Jensen, J. R., 2007: *Remote Sensing of the Environment: An Earth Resources Perspective*, 2nd edition, Pearson Prentice Hall, Upper Saddle River, New Jersey, p. 592.

Karnieli, A., Meisels, A., Fisher, L. & Arkin, Y., 1996: 'Automatic Extraction and Evaluation of Geological Linear Features from Digital Remote Sensing Data Using a Hough Transform', *Photogrammetric Engineering & Remote Sensing*, **Vol. 62, no. 5**, pp. 525-531.

Keele, R. A., 1994: *Structure and veining in the Devonian-aged Mathinna-Alberton Gold Lineament, northeast Tasmania*, 1994/06, Centre for Ore Deposit and Exploration Studies, University of Tasmania and the Tasmanian Department of Mines, Rosny Park, Tasmania, p. 27.

Keele, R. A., Taylor, B. & Davidson, G. J., 1994: 'Relationships between Devonian thrusting and gold mineralisation in northeast Tasmania', D. R, Cooke and P. A. Kitto (eds.), Contentious issues in Tasmanian geology, Geological Society of Australia, Hobart, 1994, pp. 59-60.

Koike, K., Nagano, S. & Ohmi, M., 1995: 'Lineament analysis of satellite images using a Segment Tracing Algorithm (STA)', *Computers & Geosciences*, **Vol. 21, no. 9**, pp. 1091-1104.

Leaman, D. E., 2002: *The Rock which makes Tasmania*, Leaman Geophysics, Hobart, p. 208.

Lillesand, T. M., Kiefer, R. W. & Chipman, J. W., 2007: *Remote Sensing and Image Interpretation*, 6th edition, John Wiley & Sons Inc., Hoboken, New Jersey, p. 756.

Liu, X. Y., 2008: 'Airborne LiDAR for DEM generation: Some critical issues', *Progress in Physical Geography*, **Vol. 32, no. 1**, pp. 31-49.

Digital Mapping Australia Pty Ltd (cited as DiMap), 2009: *M2/12 Schedule 2*, p. 1.

Mallet, C. & Bretar, F., 2009: 'Full-waveform topographic LiDAR: State-of-the-art', *ISPRS Journal of Photogrammetry and Remote Sensing*, **Vol. 64, no. 1**, pp. 1-16.

Maukisch, M., Stötter, J., Petrini-Monteferri, F. & Rutzinger, M., 2007: 'Algorithms for the Extraction of Geologic Lineaments from Airborne Laser Scanning Data', Laserdata, p. 10, viewed 28 April 2009, <www.laserdata.at/data/Lineament%20extraction.pdf>.

Mavrantza, O. D. & Argialas, D. P., 2006: 'Object-oriented image analysis for the identification of geologic lineaments', S. Lang, T. Blaschke & E. Schöpfer (eds.), 1st International Conference on Object-based Image Analysis (OBIA 2006), ISPRS, July 2006 <http://www.commission4.isprs.org/obia06/Papers/19_Automated%20classification%20IC%20II%20%20Geology,%20Soil,%20Natural%20Resources/OBIA2006_Mavrantza_Argialas.pdf>.

McClenaghan, M. P. & Calver, C. R. (comp.), 1994: *Geological Atlas 1:250,000 digital series, Geology of Northeast Tasmania*, Tasmania Geological Survey.

McClenaghan, M. P. (comp.), 2007: *Digital geological atlas 1:25,000 series. Sheet 5640. Mathinna*, Mineral Resources Tasmania, Rosny Park, Tasmania.

McClenaghan, M. P. & Baillie, P. W., 1975: *Geological atlas 1: 250,000 series. Sheet SK-55/4. Launceston, Geological Survey Explanatory Report*, Tasmania Department of Mines, Rosny Park, Tasmania, p. 15.

McClenaghan, M. P., Turner, N. J. & Everard, J. L., 1992: *Geological atlas 1: 50,000 series. Sheet 41 (8515S). St Helens, Geological Survey Explanatory Report*, Tasmania Department of Mines Rosny Park, Tasmania, p. 70.

McKean, J. & Roering, J., 2004: 'Objective landslide detection and surface morphology mapping using high-resolution airborne laser altimetry', *Geomorphology*, **Vol. 57, no. 3-4**, pp. 331-351.

Mouton, A., 2005: 'Generating Stream Maps Using LiDAR Derived Digital Elevation Models and 10-m USGS DEM', unpublished Masters thesis, University of Washington, p.78.

Nyborg, M., Berglund, J. & Triumf, C.-A., 2007: 'Detection of lineaments using airborne laser scanning technology: Laxemar-Simpevarp, Sweden', *Hydrogeology Journal*, **Vol. 15, no. 1**, pp. 29-32.

O'Leary, D. W., Friedman, J. D. & Pohn, H. A., 1976: 'Lineament, linear, lineation: Some proposed new standards for old terms', *Geological Society of America Bulletin*, **Vol. 87, no. 10**, pp. 1463-1469.

Patison, N. L., Berry, R. F., Davidson, G. J., Taylor, B. P., Bottril, R. S., Manzi, B., Ryba, J. & Shepherd, R. E., 2001: 'Regional metamorphism of the Mathinna Supergroup, northeast Tasmania', *Australian Journal of Earth Sciences*, **Vol. 48, no. 2**, pp. 281-292.

Pluijm, B. A. & Marshak, S., 2004: *Earth Structure*, 2nd edition, W. W. Norton & Company, New York, p. 656.

Powell, C. M., 1992: 'New perspectives on Tasmanian geology', *Bulletin of the Geological Survey of Tasmania*, **Vol. 70,** pp. 177-187.

Powell, C. M., Baillie, P. W., Conaghan, P. J. & Turner, N. J., 1993: 'The Mid-Palaeozoic turbiditic Mathinna Group, northeast Tasmania', *Australian Journal of Earth Sciences*, **Vol. 40, no. 2**, pp. 169-196.

Prothero, D. R. & Schwab, F., 2004: *Sedimentary geology: an introduction to sedimentary rocks and stratigraphy*, 2nd edition, W. H. Freeman and Company, New York, p. 557.

Raghavan, V., Wadatsumi, K. & Masumoto, S., 1993: 'Automatic extraction of lineament information from satellite images using digital elevation data', *Natural Resources Research*, **Vol. 2, no. 2**, pp. 148-155.

Reed, A. R., 2001a: 'Pre-Tabberabberan deformation in eastern Tasmania: a southern extension of the Benambran Orogeny', *Australian Journal of Earth Sciences*, **Vol. 48, no. 6**, pp. 785-796.

Reed, A. R., 2001b: *Structure and setting of Proterozoic and Palaeozoic rocks in the Tamar region, northern Tasmania*, **Field Guide No. 9,** Geological Society of Australia Specialist Group in Tectonics and Structural Geology, Mineral Resources Tasmanian and Centre for Ore Deposit Research and the School of Earth Sciences, University of Tasmania, Ulverstone, Tasmania, p. 101.

Reed, A. R., 2004: *Gold mineralisation and the regional Palaeozoic structure of the Mathinna Supergroup, eastern Tasmania*, 2004/01, Mineral Resources Tasmania, Rosny Park, Tasmania, p. 46.

Reutebuch, S. E., Andersen, H.-E. & McGaughey, R. J., 2005: 'Light Detection and Ranging (LiDAR): An Emerging Tool for Multiple Resource Inventory', *Journal of Forestry*, **Vol. 103, no. 6**, pp. 286-292.

Rice, P. J., 1997: 'Topographic and hydrologic modelling applied to mineral exploration', unpublished Masters thesis, University of Tasmania, p.226.

Richardson, R. G. & Roach, M. J., 1994: *An interpretation of recent geophysical surveys, north eastern Tasmania*, 1994/08, p. 45.

Ronacella, R. & Forlani, G., 2005, *Extraction of planar patches from point clouds to retrieve dip and dip direction of rock discontinuities*, ISPRS WG III/3, III/4, V/3 Workshop "Laser scanning 2005", September 12-14, 2005, Enschede, Netherlands, pp.162 - 167.

Rutzinger, M., Maukisch, M., Petrini-Monteferri, F. & Stötter, J., 2007: 'Development of Algorithms for the Extraction of Linear Patterns (Lineaments) from Airborne Laser Scanning Data', Geomorphology for the Future, Obergurgl, Austria, 2007, p. 8.

Sarp, G. & Toprak, V., 2007: 'An Integrated Lineament Analysis From Satellite Images', in *Proceedings of the 28th Asian Conference on Remote Sensing*, Asian Association on Remote Sensing, Kuala Lumpur, Malaysia, Nov 2007 p. 6.

Seymour, D. B. & Calver, C. R., 1995: *Explanatory notes for the Time–Space Diagram and Stratotectonic Elements Map of Tasmania*, 1995/01, Mineral Resources Tasmania, Rosny Park, Tasmania, p. 62.

Seymour, D. B., Green, G. R. & Calver, C. R., 2006: *The Geology and Mineral Deposits of Tasmania: a summary, Geological Survey Bulletin*, Mineral Resources Tasmania, Rosny Park, Tasmania, p. 29.

Shrestha, R. L., Carter, W. E., Sartori, M., Luzum, B. J. & Slatton, K. C., 2005: 'Airborne Laser Swath Mapping: Quantifying changes in sandy beaches over time scales of weeks to years', *ISPRS Journal of Photogrammetry and Remote Sensing*, **Vol. 59, no. 4**, pp. 222-232.

Soininen, A., 2005: 'TerraScan User's Guide', Terrasolid, p. 169, <http://www.terrasolid.fi/system/files/tscan.pdf>.

Stein, S. & Wysession, M., 2003: *An introduction to seismology, earthquakes, and earth structure* Blackwell Publishing Ltd, Malden, Massachusetts, p. 498.

Stewart, J., 1999: *Calculus*, 4th edition, Brooks and Cole Publishing Company, Pacific Grove, California, p. 816-865.

Sun, W., Xu, G., Gong, P. & Liang, S., 2006: 'Fractal analysis of remotely sensed images: A review of methods and applications', *International Journal of Remote Sensing*, **Vol. 27, no. 22**, pp. 4963-4990.

Taheri, J. & Findlay, R. H., 1992: *Northeast Goldfields: A summary of the Tower Hill, Mathinna and Dans Rivulet Goldfields*, UR1992/10 (unpublished report), Tasmania Department of Mines, Rosny Park, Tasmania, p. 48.

theLIST 2006: *Vector data*, Information and Land Services, Department of Primary Industries and Water, Hobart, Tasmania.

Turner, N. J. & Calver, C. R., 1987: *Geological atlas 1: 50,000 series. Sheet 49 (8514N). St Marys, Geological Survey Explanatory Report,* Tasmania Department of Mines, Rosny Park, Tasmania, p. 159.

Vacher, H. L., 2000: 'Computational Geology 12: Cramer's Rule and the Three-Point Problem', *Journal of Geoscience Education*, **Vol. 48, no. 4**, pp. 522-532.

Wallace, J., Morris, B. & Howarth, P., 2006: 'Identifying structural trend with fractal dimension and topography', *Geology*, **Vol. 34, no. 11**, pp. 901-904.

Wehr, A. & Lohr, U., 1999: 'Airborne laser scanning-an introduction and overview', *ISPRS Journal of Photogrammetry and Remote Sensing*, **Vol. 54, no. 2-3**, pp. 68-82.

Wladis, D., 1999: 'Automatic lineament detection using digital elevation models with second derivative filters', *Photogrammetric Engineering & Remotes Sensing*, **Vol. 65, no. 4**, pp. 453-458.

Wood, J., 1996: 'The Geomorphological Characterisation of Digital Elevation Models', unpublished Ph. D. thesis, University of Leicester, p.185.

Wood, J., 2000: 'Constructing Weighted Surface Networks for the Representation and Analysis of Surface Topology', Presentation given at the 5th International Conference on GeoComputation*, September 23-25th, 2000*, Chatham, UK.

Wood, J., 2009: *LandSerf-GIS*, last updated 22 Apr 2009, viewed 29 Apr 2009 <http://www.landserf.org/>.

Woodcock, N. H., 1977: 'Specification of fabric shapes using an eigenvalue method', *Geological Society of America Bulletin*, **Vol. 88, no. 9**, pp. 1231-1236.

Appendices

Appendix 1. DEM_Derivatives.lsc

```
# DEM_derivatives.lsc
# This script runs image processing tasks for generating DEM derivatives
# New surface extents are calculated to eliminate NoData cells
# created images are saved in the working directory in the following format:
# 'Directory'\'DEM file name'_'calculated surface'_'kernel size'_'distance decay'.asc

# Changes can be made to:       -DTM input file and location
#                               -convolution filter window size (Kernel)
#                               -and the distance decay function (DD)
# Lines where changes can be made are preceded with
#                   #### CHANGE PARAMETER #######
# M. Cracknell (2009)
# This program has been created with information provided in:
# Wood, J., 2009: 'LandScript-Controlling LandSerf by scripting',
#         <http://www.soi.city.ac.uk/~jwo/landserf/landserf230/doc/landscript/index.html>

version(1.0);

# OPEN DTM FILE-------------------------------------------------
#### CHANGE PARAMETER #######
baseDir="C:\LiDAR\TYNE_FINAL\SITES\E\";
#### CHANGE PARAMETER #######
file="site_e_dtm05";
##############################
dtm=open(baseDir&file&".asc");
echo("-----DTM OPENED-----");

#-------------------------------------------------------------
#-------------------------------------------------------------

# convolution filter parameters-----------------------------
#### CHANGE PARAMETER #######
kernel=21;
##############################
DD=0;

# Low Pass filter dtm
smoother=surfparam(dtm,"elev",kernel,DD);
echo("-----SMOOTH DTM SURFACE CALCULATED-----");
save(smoother,baseDir&"temp_dtm.srf");

# fractal dimension-----------------
frac=surfparam(dtm,"fractal",kernel,DD);
echo("-----FRACTAL SURFACE CALCULATED-----");
save(frac,baseDir&"temp_frac.srf");
```

```
# slope-----------------------------
sloper=surfparam(dtm,"slope",kernel,DD);
echo("-----SLOPE SURFACE CALCULATED-----");
save(sloper,baseDir&"temp_slope.srf");

# aspect-----------------------------
aspects=surfparam(dtm,"aspect",kernel,DD);
echo("-----ASPECT SURFACE CALCULATED-----");
save(aspects,baseDir&"temp_aspect.srf");

# curvature--------------------------
DD = 2;
curv=surfparam(dtm,"meanc",kernel,DD);
echo("-----CURVATURE SURFACE CALCULATED-----");
save(curv,baseDir&"temp_curv.srf");

#---------------------------------------------------------------

# TEMP EXTENT-----------------------------------------------------
# get image parameters
west=info(curv,"W");
south=info(curv,"S");
x=info(curv,"numCols");
y=info(curv,"numRows");
grid=info(curv,"xRes");

# calculate new parameters for extent
Nwest=west+(((kernel-1)/2)*grid);
Nsouth=south+(((kernel-1)/2)*grid);
Nx=x-(kernel-1);
Ny=y-(kernel-1);

# new extent
extent=newraster(Nwest,Nsouth,grid,grid,Ny,Nx);
echo("-----NEW EXTENT CREATED-----");
winsize=grid*kernel;
echo("-----All images processed with "&winsize&" m kernel-----");

#---------------------------------------------------------------
#---------------------------------------------------------------

# add curvature to SMOOTH DTM--------
added=newraster(Nwest,Nsouth,grid,grid,Ny,Nx);
added=smoother+curv;
echo("-----SMOOTHED SURFACE ADDED TO DTM-----");
save(added,baseDir&"temp_addDTM_curv.srf");

# net feature------------------------
net2=surfparam(added,"netfeature",kernel,DD);
echo("-----NET FEATURE SURFACE CALCULATED-----");
```

```
save(net2,baseDir&"temp_net_addDTM_curv.srf");

#-----------------------------------------------------------------
#-----------------------------------------------------------

# FINAL EXTENT-----------------------------------------------
# get image parameters
west=info(net2,"W");
south=info(net2,"S");
x=info(net2,"numCols");
y=info(net2,"numRows");
grid=info(net2,"xRes");

# calculate new parameters for extent
Nwest=west+(((kernel-1)/2)*grid);
Nsouth=south+(((kernel-1)/2)*grid);
Nx=x-(kernel-1);
Ny=y-(kernel-1);

# final extent
fextent=newraster(Nwest,Nsouth,grid,grid,Ny,Nx);
echo("-----NEW EXTENT CREATED-----");

#-----------------------------------------------------------------
#-----------------------------------------------------------------

DD = 0;
# save files with final extent NoData eliminated

temper=open(baseDir&"temp_dtm.srf");
fextent=temper;
save(fextent,baseDir&file&"_smooth_"&kernel&"-"&DD&".asc","arcgridtext");
echo("-----SMOOTH DTM SURFACE SAVED-----");
freqdist(fextent,baseDir&file&"_histo_smooth_"&kernel&"-"&DD&".txt",0,1);
echo("-----SMOOTH DTM SURFACE HISTOGRAM SAVED-----");

fextent=newraster(Nwest,Nsouth,grid,grid,Ny,Nx);
temper=open(baseDir&"temp_frac.srf");
fextent=temper;
save(fextent,baseDir&file&"_fractal_"&kernel&"-"&DD&".asc","arcgridtext");
echo("-----FRACTAL SURFACE SAVED-----");
freqdist(fextent,baseDir&file&"_histo_fractal_"&kernel&"-"&DD&".txt",2,0.004);
echo("-----FRACTAL SURFACE HISTOGRAM SAVED-----");

fextent=newraster(Nwest,Nsouth,grid,grid,Ny,Nx);
temper=open(baseDir&"temp_slope.srf");
fextent=temper;
save(fextent,baseDir&file&"_slope_"&kernel&"-"&DD&".asc","arcgridtext");
echo("-----SLOPE SURFACE SAVED-----");
freqdist(fextent,baseDir&file&"_histo_slope_"&kernel&"-"&DD&".txt",0,1);
echo("-----SLOPE SURFACE HISTOGRAM SAVED-----");
```

```
fextent=newraster(Nwest,Nsouth,grid,grid,Ny,Nx);
temper=open(baseDir&"temp_aspect.srf");
fextent=temper;
save(fextent,baseDir&file&"_aspect_"&kernel&"-"&DD&".asc","arcgridtext");
echo("-----ASPECT SURFACE SAVED-----");
freqdist(fextent,baseDir&file&"_histo_aspect_"&kernel&"-"&DD&".txt",0,1);
echo("-----ASPECT SURFACE HISTOGRAM SAVED-----");

#-------------------------------------------------------------------------
fextent=newraster(Nwest,Nsouth,grid,grid,Ny,Nx);
temper=open(baseDir&"temp_addDTM_curv.srf");
fextent=temper;
save(fextent,baseDir&file&"_"&kernel&"-"&DD&"_curv_DTMadd.asc","arcgridtext");
echo("-----DTM + SMOOTHED SURFACE SAVED-----");

fextent=newraster(Nwest,Nsouth,grid,grid,Ny,Nx);
temper=open(baseDir&"temp_net_addDTM_curv.srf");
fextent=temper;
save(fextent,baseDir&file&"_netfeature_"&kernel&"-"&DD&"_curv_DTMadd.asc","arcgridtext");
echo("-----NET FEATURE SURFACE SAVED-----");
freqdist(fextent,baseDir&file&"_histo_netfeature_"&kernel&"-"&DD&"_curv_DTMadd.txt",0,1);
echo("-----NET FEATURE SURFACE HISTOGRAM SAVED-----");


#-----------------------------------------------------------------
fextent=newraster(Nwest,Nsouth,grid,grid,Ny,Nx);
temper=open(baseDir&"temp_curv.srf");
fextent=temper;
DD = 2;
save(fextent,baseDir&file&"_curvature_"&kernel&"-"&DD&".asc","arcgridtext");
echo("-----CURVATURE SURFACE SAVED-----");
freqdist(fextent,baseDir&file&"_histo_curvature_"&kernel&"-"&DD&".txt",-10,0.01);
echo("-----CURVATURE SURFACE HISTOGRAM SAVED-----");
```

Appendix 2. Automated lineament detection: methods and preliminary results

This brief report provides a summary of the automated methods developed in an attempt to enhance, select and extract geological lineaments from high resolution Digital Elevation Models (DEMs). Details of the general theory for automated lineament detection methods and their sources are provided in Chapter 4 of the accompanying thesis. Details of the methods carried out to generate the DEMs used in the following summary are provided in Chapter 3.

Software

Two different Geographic Information System (GIS) applications have been principally used to carry out the processing described in this summary, they are as follows:

- LandSerf 2.3. (open source software and code available from, http://www.landserf.org/)
- ArcGIS (licensed software available from Environmental Systems Research Institute)

In addition, python code has been written to convert 3D points representing extracted lineaments to 3D planes (i.e. dip and dip direction). The theory behind the conversion of3D points to planes using a Moment-of-Inertia (MOI) algorithm (Fernández, 2005) is described in Chapter 4. A copy of this code is presented in Appendix 4 and the code file (PointsToPlane.py) is provided in the accompanying DVD. Python code has also been written to plot rose diagrams of lineament trends.

Methods

DEMs were initially processed in LandSerf using LandScript a Java based programming language. A copy of this code (DEM_Derivatives.lsc) is provided in Appendix 1. This code generates a range of DEM derivatives and feature images some of which are described below. Two main processes were investigated. The first uses a morphological filtering function to generate surfaces representing geomorphic features then converts neighbouring pixels of either ridge or channel classes to lines. The second used DEM 2nd derivative surfaces to enhance topographic discontinuities then clips LiDAR point data based on pixel areas defined by numeric thresholds. A variety of ArcGIS geoprocessing tools were combined in Modelbuilder to facilitate experimentation and automate the lineament selection methods described in this section (ESRI, 2008). The Modelbuilder tools have been provided in the accompanying DVD.

Before conversion to lines in ArcGIS, a road line layer was manually digitised using the 2m DEM. This file was created in order to prevent roads being converted to “lineaments” in the final images and generated lineament vector files.

Morphological filters

In LandSerf, DEM curvature surfaces were generated and then added to the original DEM, thus accentuating topographic discontinuities. The "Feature Network Extraction" function in Landserf was used to generate pixels representing one of the six morphological feature classes (ridge, channel, peak, pit, pass and plane (Wood, 1996)) from the DEM/curvature combination image. Various scales of observation were simulated using a range of convolution filter kernels and DEM resolutions. The resulting scale of observation can be determined by calculating the product of the DEM grid cell size and the filter kernel dimensions. All image files were saved in ASCII grid text format. The Feature Network Extraction image was then imported into ArcGIS for refinement of feature image pixels and conversion to vector data format (i.e. lines representing the features). For reasons unknown, only horizontal lines were obtained using LandSerfs' inbuilt "Feature Network to Vector" function.

Figure 1 presents the Modelbuilder workflow for the initial conversion of Network Features. This file is located in the LINEAMENTS.tbx → Network To Line (1) Modelbuilder file. A description of the Network To Line (1) workflow and parameters is provided in Table 1. The basic principle of the method is to convert the Network Features to lines for extraction of attributes. Landserf documentation provides information on the representative feature classes contained within the Network Feature Extraction output image that have been used to select ridges (i.e. ridge and peak classes) and channels (i.e. channels and pit classes) (Wood, 2009). However, forestry operations and river channels are also identified therefore an attempt to eliminate them from the processing is achieved by filtering out slopes less than 5°. This value was arbitrarily chosen because most of human activity and alluvial sediments incised by rivers are can be found on flat terrain. Other artificial features such as roads were initially digitised as lines then eliminated from the output feature files using the buffer tool.

Extraction of features attributes such as mean orientation, length, and location including and 3D points was conducted within ArcGIS via Network To Line (2) Modelbuilder (Figure 2). The details of processing steps are given in Table 2. Line outputs can be displayed and/or analysed based on their attributes; length and orientation being the most relevant. 3D points generated from this process have been input into PointsToPlane.py for the estimation of best-fit planes.

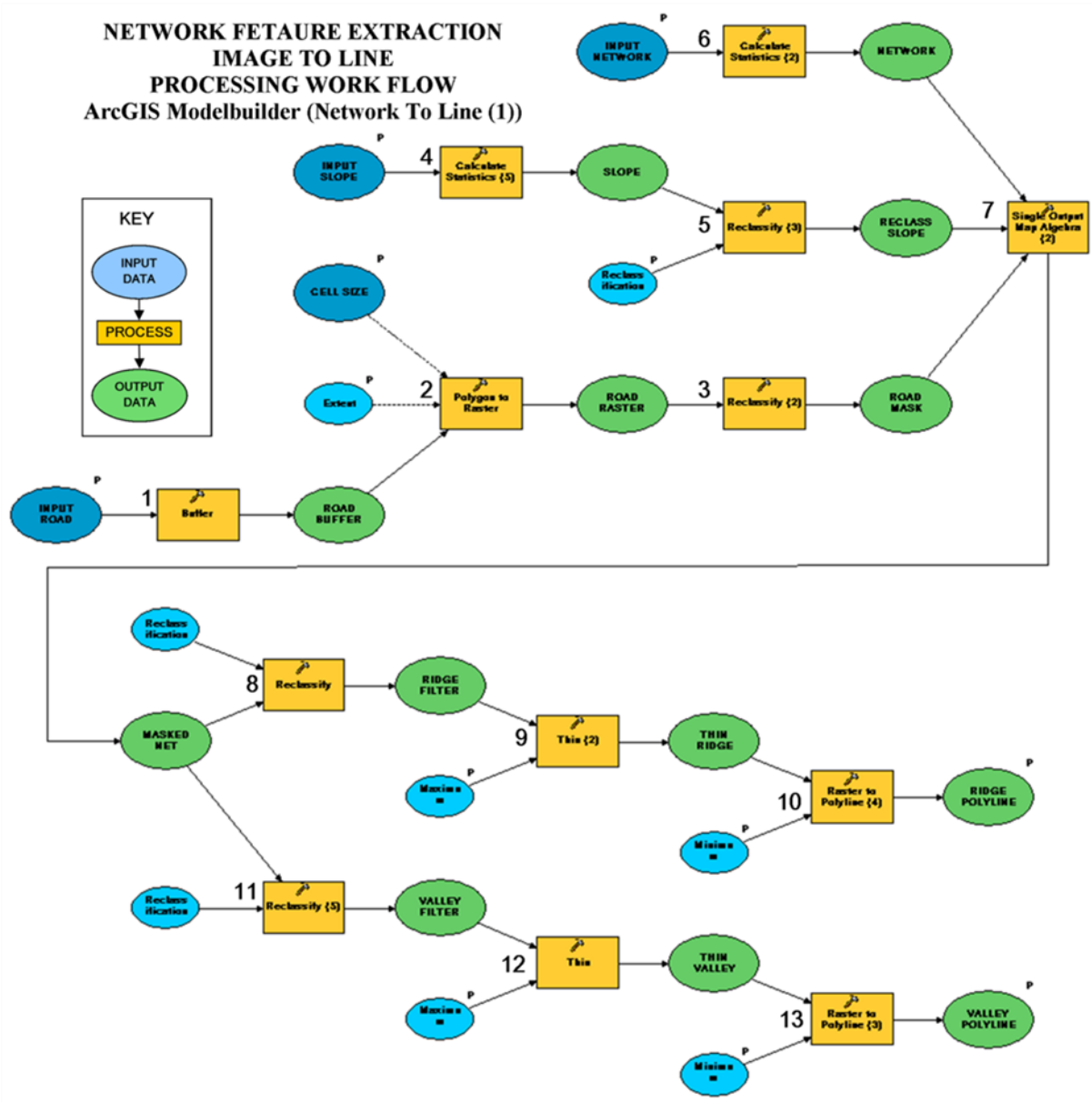

Figure 1 Network To Line (1) work flow in Modelbuilder input and output files including processing tools and parameters details can be found in Table 1, generates lines from Feature Network image

A selection of results from the two processes described above are presented as frequency rose diagrams and scatter plots. These have been chosen to highlight the spurious results obtained. A series of strike (obtained from the mean orientation process) frequency rose diagrams showing data processed at different scales of observation are presented in Figure 3 and Figure 4 for ridge and channel features respectively. Both plots show the highest frequency of strike trends are consistently aligned east-west (i.e. toward 90°). This is s most apparent in the highest resolution datasets (i.e. scale of 10.5 m and resolution of 0.5 m) with reducing bias orientations (i.e. east-west) as scales of observation increase. Strikes of north-south, northeast-southwest and northwest-southeast are also predominantly represented as high frequency trends for both ridge and channel features.

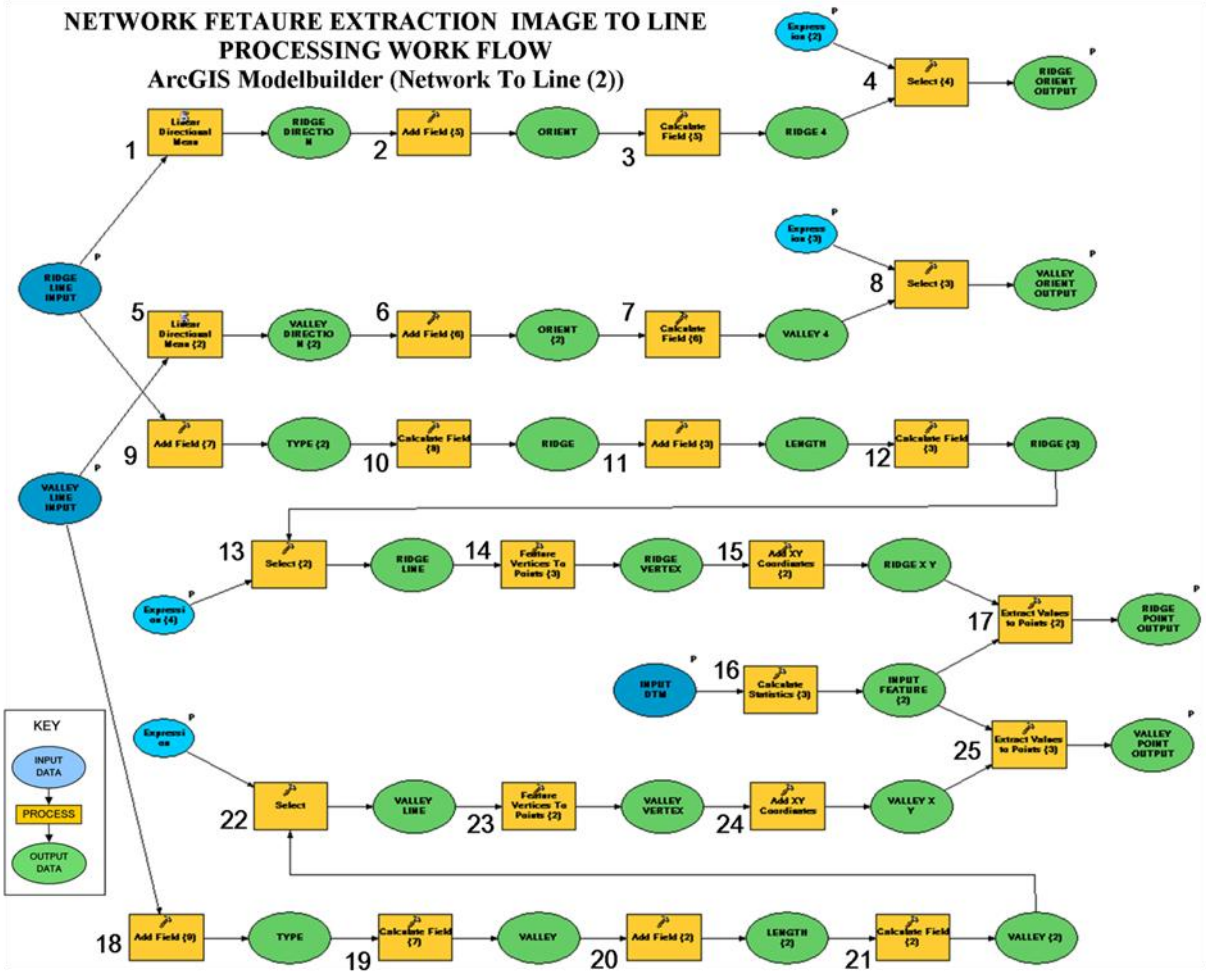

Figure 2 Network To Line (2) work flow in Modelbuilder input and output file including processing tools and parameters details can be found in Table 2, generates lines with mean orientation, length and location attributes and also converts lines to 3D points for input into PointsToPlane.py

The bias seen in the strike trends is clearly defined in Figure 5b, which presents a rose scatter plot of the log of length (m) vs. strike (°) for channel features. Shorter features are more likely to trend in one of the eight cardinal directions. I suspect that directional bias is created from one of more of the processing steps for the conversion of gridded data into vector data carried out in Network to Line (1) (i.e. Figure 1). For example, when joining points representing the centre of adjacent grid cells to create a line, there are only 8 directions that the line can be drawn in due to the inherent square geometry of a grid cell and its spatial relationship to neighbouring cells. Therefore, the shorter a feature is the more likely it will display a mean orientation that corresponds to one of the 8 directions that connects adjacent grid cells.

Table 1 Network To Line (1) workflow (see Figure 1), converts ridges and valleys form network raster to polylines (feature classes from LandSerf)

STEP	INPUT	PROCESS	PARAMETERS	OUTPUT	COMMENTS
1	road.shp (polyline)	Buffer	Distance = 10 m	road_buffer.shp (polygon)	creates a buffer around road layer
2	road_buffer.shp (polygon)	Polygon to Raster	Extent = Network.asc Cell Size = n m	road_raster.grd	converts road buffer to grid based on Network image extent and cells size (must be defined)
3	road_raster.grd	Reclassify	Cell value = 0 NoData = 1	road_mask.grd	converts road_raster buffer cells to 0 and NoData to 1
4	slope.asc	Calculate Statistics		slope.grd	enable ArcGIS to read image file
5	slope.grd	Reclassify	slope < 5 = 0 slope >5 and < 90 = 1	reclass_slope.grd	filter low slope values to eliminate forestry operations and river channels
6	network.asc	Calculate Statistics		network.grd	enable ArcGIS to read image file
7	road_mask.grd reclass_slope.grd network.grd	Map Algebra	product of inputs	masked_network.grd	create network image with low slope and roads given values of 0
8	masked_network.grd	Reclassify	0 → NoData 1 → NoData 2 → NoData 3 → 2 4 → 2 5 → NoData 6 → NoData	ridge_filter.grd	extracts ridge features (3 = peak and 4 = ridge) and isolates from other pixels in image
9	ridge_filter.grd	Thin	Background Value = NoData Max thickness of features = grid cell size * filter kernel size	thin_ridge.grd	reduces ridge pixels (i.e. cell value = 2) to a linear feature 1 pixel wide, max. thickness of features parameter based on the scale of observation for generating network.asc (i.e. grid cell size * filter kernel size) in an attempt to define elongate linear features
10	thin_ridge.grd	Raster to Polyline	Min. dangle length = grid cell size * filter kernel size Simplify Lines = UNCHECKED	ridge_polylines.shp (polyline)	converts thinned ridge pixels to line, min. dangle length eliminates lines less than scale of observation (see above)
11-13	masked_network.grd			valley_polylines.shp	same process as for ridges (steps 8-10) but coverts channel features to lines ((1 = pit and 2 = channel)

Table 2 Network To Line (2) workflow (see Figure 2), converts ridge and valley polylines to lines representing mean orientation for analysis, and to points for input into PointsToPlane.py

STEP	INPUT	PROCESS	PARAMETERS	OUTPUT	COMMENTS
1	ridge_polylines.shp (polyline)	Linear Directional Mean		ridge_directional_mean.shp (polyline)	calculates mean orientation of polylines (based on end nodes), length and mean location, output is a straight line characterising calculated attributes
2	ridge_directional_mean.shp (polyline)	Add Field	Field Name = ORIENT Field Type = DOUBLE	ridge_directional_mean.shp (polyline)	

3	ridge_directional_mean.shp (polyline)	Calculate Field	EXPRESSION =
			Dim dblOrient as double
			If [CompassA] > 180 Then
			dblOrient = [CompassA]-180
			
			else
			dblOrient = [CompassA]
			end if
				ridge_directional_mean.shp (polyline)	calculates strike orientation of line feature (with respect to grid north) with values between 0-180° using Visual Basic and populates new field created in previous step

4	ridge_directional_mean.shp (polyline)	Select	EXPRESSION = "AveLen" > n (m)	ridge_orient_filter.shp (polyline)	filters features based on length, length threshold based on the scale of observation for generating network.asc (i.e. grid cell size * filter kernel size)
5-8	valley_polylines.shp (polyline)			valley_orient_filter.shp (polyline)	same process as for ridges (steps 1-4) but calculates mean orientation etc. for channel features then filters results
9	ridge_polylines.shp (polyline)	Add Field	Field Name = TYPE Field Type = TEXT	ridge_polylines.shp (polyline)	
10	ridge_polylines.shp (polyline)	Calculate Field	EXPRESSION = "ridge"	ridge_polylines.shp (polyline)	associates text attribute defining type of feature (i.e. ridge)
11	ridge_polylines.shp (polyline)	Add Field	Field Name = LENGTH Field Type = DOUBLE	ridge_polylines.shp (polyline)	
12	ridge_polylines.shp (polyline)	Calculate Field	EXPRESSION = Dim dblLength as double Dim pCurve as ICurve Set pCurve = [shape] dblLength = pCurve.Length	ridge_polylines.shp (polyline)	calculates length (m) of input polyline features using Visual Basic code
13	ridge_polylines.shp (polyline)	Select	EXPRESSION = "LENGTH" > n (m)	ridge_polylines _filter.shp (polyline)	filters features based on length, length threshold based on the scale of observation for generating network.asc (i.e. grid cell size * filter kernel size)
14	ridge_polylines _filter.shp	Feature Vertices to Points	PointType = ALL	ridge_vertex.shp	converts all polyline vertices to points
15	ridge_vertex.shp	Add XY Coordinates		ridge_vertex.shp	associates x and y coordinates to points
16	DEM.asc	Calculate Statistics		DEM.grd	enable ArcGIS to read image file
17	DEM.grd ridge_vertex.shp	Extract Values to Points	Interpolate = UNCHECKED	Extract_ridge_point.shp	associates z coordinate to points from DEM, now points have 3D georeferenced coordinates for input into PointsTo_Plane.py
18-25	valley_polylines.shp (polyline)			Extract_valley_point.shp	same process as for ridges (steps 9-17) but associates 3D coordinates to points representing channel features

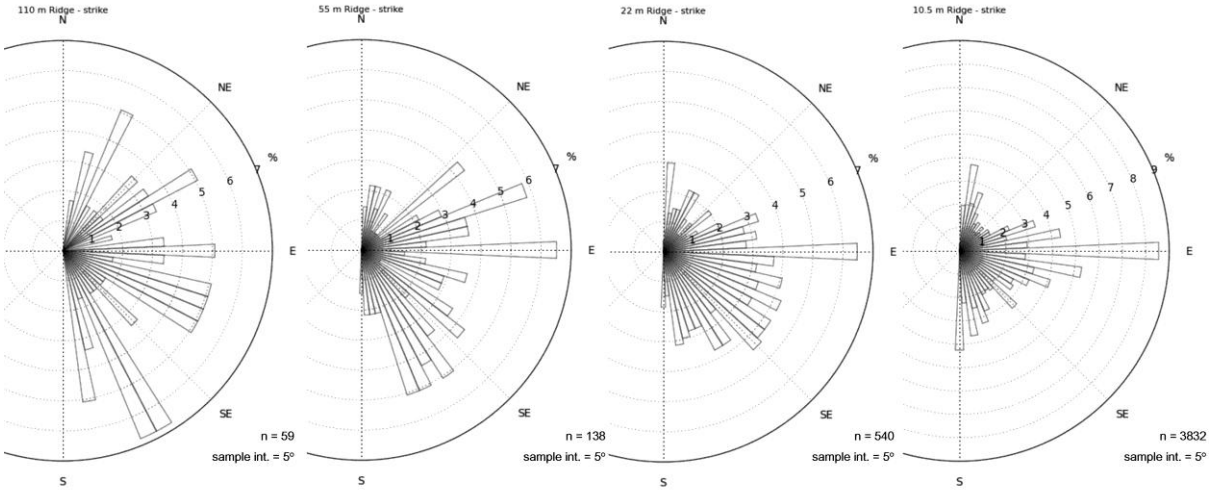

Figure 3 Ridge strike (from mean orientation data) frequency rose diagrams for different scales of observation

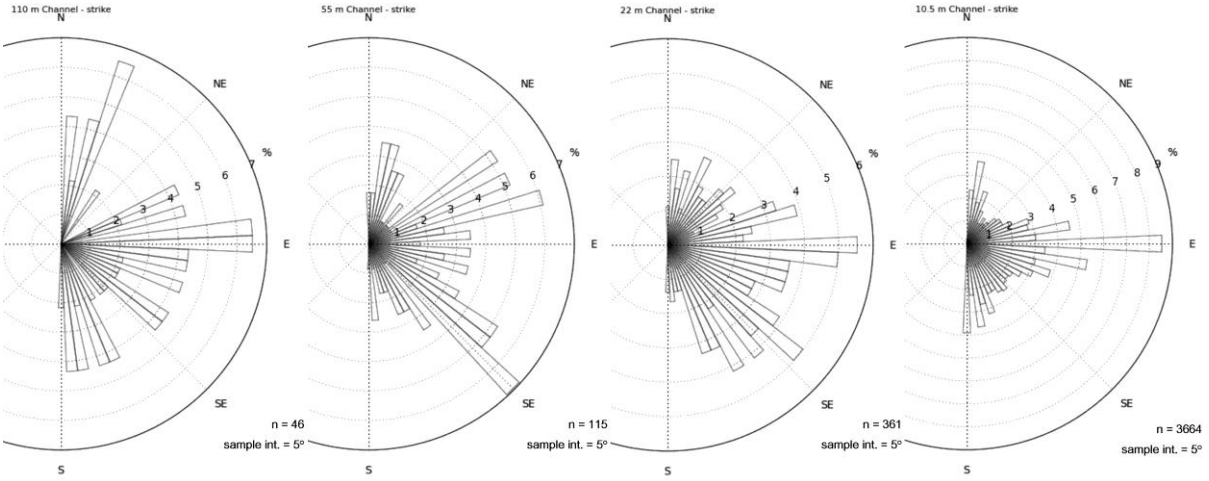

Figure 4 Channel strike (from mean orientation data) frequency rose diagrams for different scales of observation

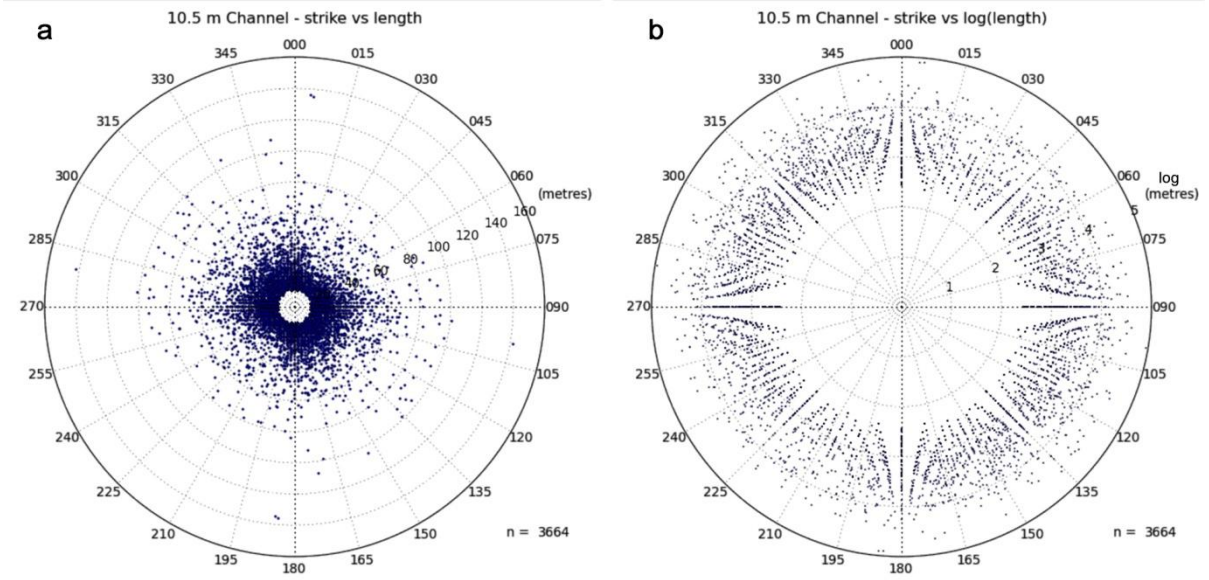

Figure 5 Channel length (radius) vs. strike (from mean orientation data) scatter rose diagrams, a) length (m) vs. strike and b) log (length) vs. strike, note strike data from 0-180° has been plotted on both sides of rose diagram

Extracted 3D georeferenced points from the process conducted via Network To Line (2) have been imported into the PointsToPlane.py program. The frequency rose diagrams dip direction results from the best-fit planes calculated via the MOI algorithm for ridge (Figure 6a) and channel (Figure 6b) features show remarkable similarity to the frequency distribution of the 0.5 m DEM aspect derivative (Figure 6c). Further investigations into these results confirmed that the best-fit planes did not represent geological phenomena, but conformed to the slope and aspect of the topography.

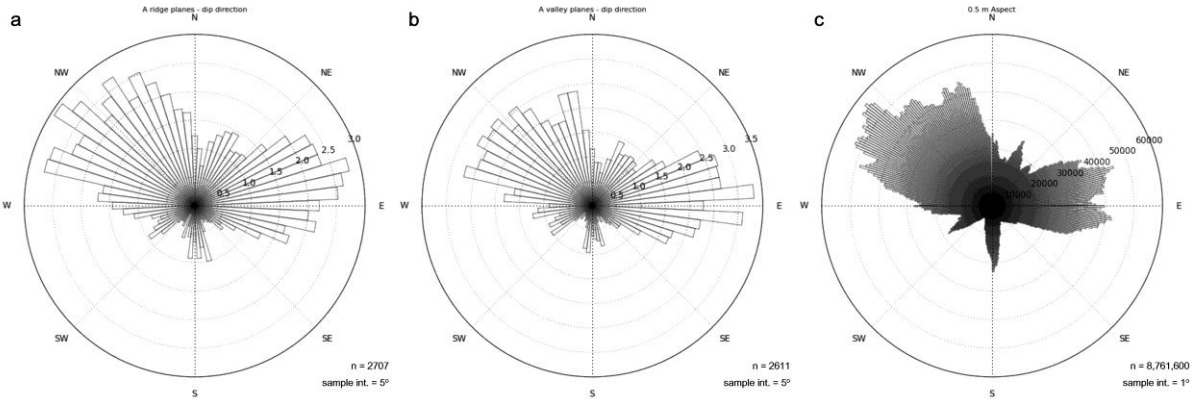

Figure 6 Frequency rose diagrams of MOI results (i.e. PointsToPlane.py) and DEM derivatives, a) ridge dip direction (%), b) channel dip direction (%) and c) aspect (total count)

Curvature surface threshold for 3D point extraction

In an attempt to eliminate the trend bias seen in the morphological filter to line method described above, a process was developed that extracted 3D georeferenced point data from either a DEM or the original LiDAR point datasets (LAS file format). Figure 7 presents the Modelbuilder workflow for the Edge to Points process. Table 3 provides detailed descriptions of the processing steps and their parameters.

The Edge To Points process takes the 2nd derivative (curvature) surfaces generated via LandSerf and defines areas of high positive (convex = ridge) and low (concave = channel) curvature. Thresholds in this case are based on the mean and standard deviation statistics calculated from the curvature image. These thresholds can be altered in the future is so desired. Output points are taken from either the DEM or the original LAS file (post-processed LiDAR dataset). If using a LAS file, several steps including, point merging, ground return filtering and text file export must be carried out first. Lastools (Isenburg, & Shewchuk, 2009) is an efficient open source command prompt based software package that can complete these tasks. The 3D points are given polygon feature ID attributes so that the PointToPlane.py algorithm can group points based on an individual feature.

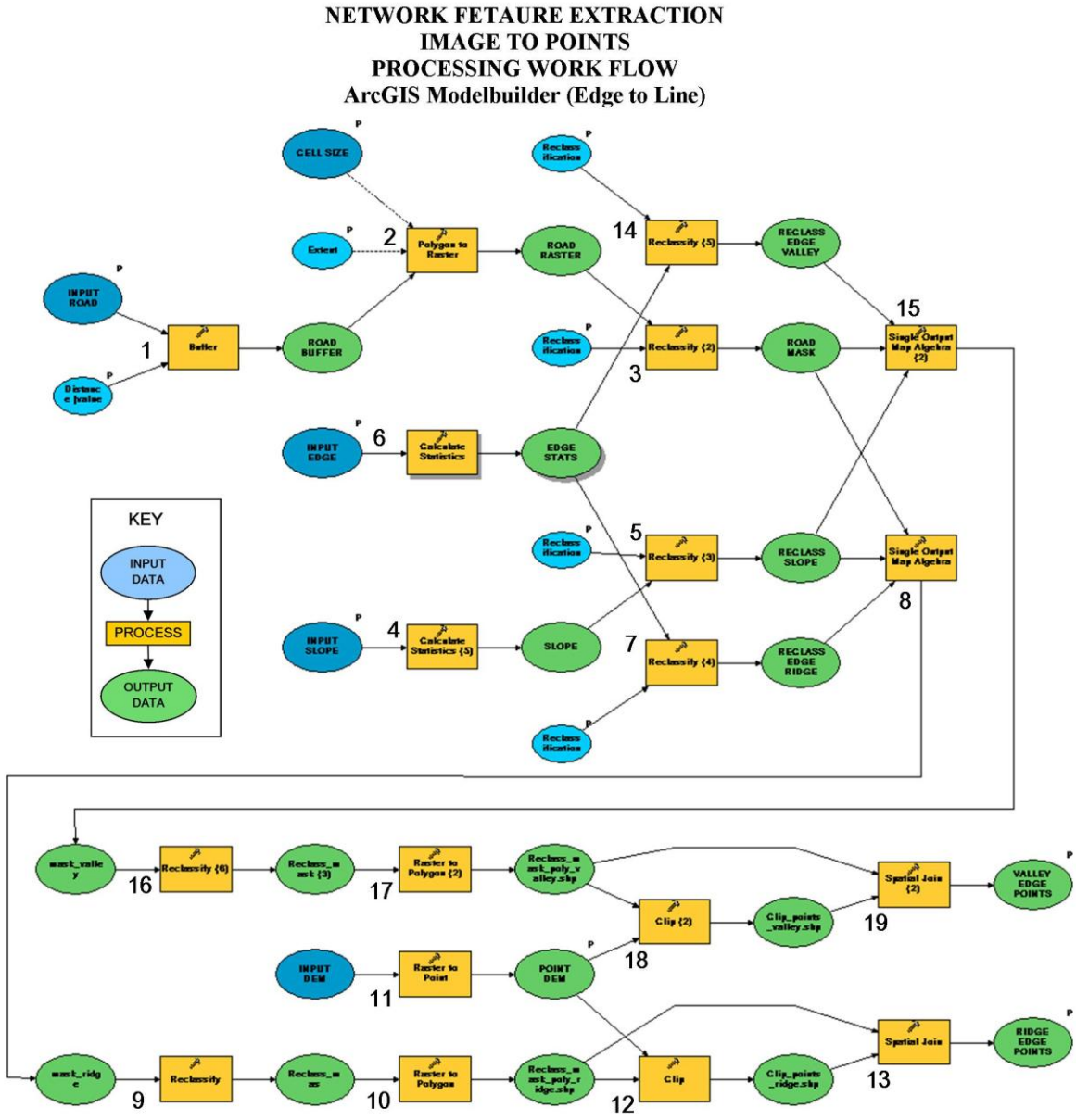

Figure 7 Edge To Points work flow in Modelbuilder input and output files including processing tools and parameters details can be found in Table 3, extracts 3D points based on curvature thresholds for input into PointsToPlane.py

Results similar to the Network To Line (2) process were obtained from the Edge To Points process regarding the orientation of best-fit planes (i.e. describing the slope and aspect of the topography). No further processing of points was carried out due to time constraints. However, I suspect that once the LAS points have been extracted, representing target features, then the identification of edges should proceed on these points. This will be achieved using similar point cloud analysis techniques as described by Filin & Pfeifer (2006), Chen *et al.* (2008) and Ronacella & Forlani (2005) (see Chapter 4 for more details).

Table 3 Edge To Points (2) workflow (see Figure 7), extracts 3D points (from either DEM or LAS file) for input into PointsToPlane.py based on curvature thresholds

STEP	INPUT	PROCESS	PARAMETERS	OUTPUT	COMMENTS
1-3	road.shp (polyline)			road_mask.grd	converts road layer (polylines) to grid mask for eliminating roads from processing (see Table 1 for more details)
4-5	slope.asc			reclass_slope.grd	converts slope layer (grid) to mask for eliminating low slopes (i.e. human activity and river channels) from processing (see Table 1 for more details)
6	DEM_curvature.asc	Calculate Stats.		curvature.grd	enable ArcGIS to read image file
7	curvature.grd	Reclassify	-100-curvMEAN + curv1STDev → 0 curvMEAN + curv1STDev → 1	reclass_ridge.grd	extracts positive curvature pixels (i.e. convex features = ridge) features and isolates from other pixels in image based on the curvature image statistics
8	road_mask.grd reclass_slope.grd reclass_ridge.grd	Map Algebra	product of inputs	mask_ridge.grd	isolates high positive curvature with low slope and roads given values of 0
9	mask_ridge.grd	Reclassify	0 → NoData 0-1 → 1 NoData → NoData	ridge.grd	converts non-target pixels to NoData
10	ridge.grd	Raster to Polygon	Simplify polygons = CHECKED	ridge_poly.shp (polygon)	converts target pixels to polygons
11	DEM.asc	Raster to Point		DEM_points.shp (point)	converts DEM grid cells to points with elevation attribute (this step can be omitted if using the original LAS point file
12	DEM_points.shp (point) OR LAS_points,shp (point) AND ridge_poly.shp (polygon)	Clip		clip_points_ridge.shp (point)	clip target points based on polygon extents
13	clip_points_ridge.shp (point) ridge_poly.shp (polygon)	Spatial Join	Target Features = Clip_points_ridge.shp Join_Features = ridge_poly.shp Join Operation = JOIN_ONE_TO_ONE	extract_ridge_points.shp (points)	associate polygon ID attribute to points for input into PointsToPlane.py
14-19	curvature.grd			extract_valley_points.shp (points)	same process as for ridges (steps 7-13) but 3D points representing channel features, changes made to initial reclassification thresholds in this case defined by curvMEAN-curv1STDev
NOTE	LASfile	Convert to shapefile			to use the LAS point file in ArcGIS the following steps must be carried out Using Lastools (Isenburg & Shewchuk, 2009): -select image extent and clip LAS points -filter non-ground returns -export to txt with (Xm, Ym, Zm coordinates-can include other attributes i.e. intensity) In ArcGIS -import txt file and display XY coordinates -convert to LAS_points.shp (point)

References

Chen, L. C., Teo, T. A., Kuo, C. Y. & Rau, J. Y., 2008: 'Shaping Polyhedral Buildings by the Fusion of Vector Maps and LiDAR Point Clouds', *Photogrammetric Engineering & Remote Sensing*, **Vol. 74, no. 9**, pp. 1147-1157.

Filin, S. & Pfeifer, N., 2006: 'Segmentation of airborne laser scanning data using a slope adaptive neighborhood', *ISPRS Journal of Photogrammetry and Remote Sensing*, **Vol. 60, no. 2**, pp. 71-80.

Fernández, O., 2005: 'Obtaining a best-fitting plane through 3D georeferenced data', *Journal of Structural Geology*, **Vol. 27, no. 5**, pp. 855-858.

Isenburg, M. & Shewchuk, J. 2009: *Lastools*, <http://www.cs.unc.edu/~isenburg/lastools/>.

Ronacella, R. & Forlani, G., 2005: *Extraction of planar patches from point clouds to retrieve dip and dip direction of rock discontinuities*, ISPRS WG III/3, III/4, V/3 Workshop "Laser scanning 2005", September 12-14, 2005, Enschede, Netherlands, 162-167.

Wood, J., 1996: 'The Geomorphological Characterisation of Digital Elevation Models', unpublished Ph. D. thesis, University of Leicester, p.185.

Wood, J., 2009: *LandSerf-GIS*, last updated 22 Apr 2009, viewed 29 Apr 2009 <http://www.landserf.org/>.

Appendix 3. README.txt information file for PointsToPlane.py

<README.txt>

-----Information for the setup and running of PointsToPlane.py-----
M. Cracknell (2009)
With many thanks to:
J. O'Farrell-for help with Classes and Dictionaries
D. Green for making sure that the output was correct
L. Graham-for compiling vector.pyc

The following modules must be installed to run this program:
python 2.6-available at <http://www.python.org/download/>
NumPy 1.3.0-available at <http://www.scipy.org/Download>
SciPy 0.7.0available at <http://www.scipy.org/Download>
dbfpy-available at <http://dbfpy.sourceforge.net/>

The following must be located in the directory containing PointToPlane.py:
vector.pyc supplied with this program
vector.py supplied with this program or available through pyformex-0.5.tar.gz
<http://developer.berlios.de/project/showfiles.php?group_id=2717>

This program has been written in python 2.6 and has used information provided in:
python Community, 2009: 'python 2.x documentation', <http://www.python.org/doc/>
NumPy Community, 2009: 'NumPy Reference, Release 1.4.0dev7026',
<http://docs.scipy.org/doc/>
SciPy Community, 2009: 'SciPy Reference Guide, Release 0.8dev', <http://docs.scipy.org/doc/>
Kunce, J. and Fiby, H., n.d.: 'python Modules for accessing .dbf (xBase) files',
<http://dbfpy.sourceforge.net>
Vacher, H. L., 2000: 'Computational Geology 12: Cramer's Rule and the Three-Point Problem',
Journal of Geoscience Education, Vol. 48, no. 4, pp. 522-532.

Appendix 4. PointsToPlane.py

```
#  PointsToPlane.py- M. Cracknell, 2009,. version: python 2.6
#  aims:       import dbf file
#              extract data from dbf file
#              select points and group based on ArcID Field
#              calculate plane parameters and residual fit data
# Program outputs: -.csv file of plane coefficients with best-fit parameters
#                     and dip and dip direction of planes
#               -also outputs .csv of x,y,z, coords of plane bounding
#                     box for polygon shapefile creation
# for more information please view README.txt

# import modules
from dbfpy import dbf
import csv
from math import *
import numpy as np
from numpy import *
import scipy as sp
from scipy import linalg
# must have vector.py and associated module vector.pyc installed in working directory
import vector
#--------------------functions and classes for program-----------------
class Coord:
      def __init__(self, x, y, z):
            self.Xm = round(x,1)
            self.Ym = round(y,1)
            self.Zm = round(z,1)

class Diff:
      def __init__(self, x, y, z):
            self.Xdiff = x
            self.Ydiff = y
            self.Zdiff = z

class OutData:
      def __init__(self):
            self.ID = None
            self.N_points = None
            self.Xmean = None
            self.Ymean = None
            self.Zmean = None
            self.M = None
            self.K = None
            self.A = None
            self.B = None
            self.C = None
            self.D = None
            self.RMSE = None
            self.Dip = None
            self.Dipdir = None

class Record:
      def __init__(self, newID):
            self.recID = newID
```

```
        self.coords = []
        self.diffs = []
        self.output = OutData()


    def average(self):
        xvals = 0.0
        yvals = 0.0
        zvals = 0.0
        count = 0
        for c in self.coords:
            xvals = c.Xm + xvals
            yvals = c.Ym + yvals
            zvals = c.Zm + zvals
            count = count + 1

        if count > 2:
            self.output.Xmean = xvals / count
            self.output.Ymean = yvals / count
            self.output.Zmean = zvals / count
            self.output.N_points = count
            self.output.ID = self.recID

            for c in self.coords:
                xvals = c.Xm - self.output.Xmean
                self.Xdiff = xvals
                yvals = c.Ym - self.output.Ymean
                self.Ydiff = yvals
                zvals = c.Zm - self.output.Zmean
                self.Zdiff = zvals
                self.diffs.append(Diff(self.Xdiff,self.Ydiff,self.Zdiff))
        else:
            self.output.Xmean = -9999
            self.output.Ymean = -9999
            self.output.Zmean = -9999
            self.output.N_points = count
            self.output.ID = self.recID

            for c in self.coords:
                self.diffs.append(Diff(-9999,-9999,-9999))

    def plane_calc(self):
        v11 = []
        v12 = []
        v13 = []
        v22 = []
        v23 = []
        v33 = []
        for p in self.diffs:
            a = p.Xdiff
            b = p.Ydiff
            c = p.Zdiff
            temp11 = a**2
            v11.append(temp11)
            temp12 = a * b
            v12.append(temp12)
            temp13 = a * c
```

```
        v13.append(temp13)
        temp22 = b**2
        v22.append(temp22)
        temp23 = b * c
        v23.append(temp23)
        temp33 = c**2
        v33.append(temp33)
sum11 = sum(v11)
sum12 = sum(v12)
sum13 = sum(v13)
sum22 = sum(v22)
sum23 = sum(v23)
sum33 = sum(v33)
matrix1 = [sum11, sum12, sum13]
matrix2 =  [sum12, sum22, sum23]
matrix3 = [sum13, sum23, sum33]
la,v = linalg.eig([matrix1, matrix2, matrix3])
l1, l2, l3 = la
Eigenvalues = []
Eigenvalues.append(l1.real)
Eigenvalues.append(l2.real)
Eigenvalues.append(l3.real)
eigen3 = np.amin(Eigenvalues)
posi = Eigenvalues.index(eigen3)
v1, v2, v3 = v
vec = [v1[posi],v2[posi],v3[posi]]
Eigval = []
if l1.real < l2.real and l2.real < l3.real:
        eig1 = l3.real
        eig2 = l2.real
        eig3 = l1.real
        Eigval = [eig1,eig2,eig3]
elif l1.real < l2.real and l2.real > l3.real and l1.real > l3.real:
        eig1 = l2.real
        eig2 = l1.real
        eig3 = l3.real
        Eigval = [eig1,eig2,eig3]
elif l1.real < l2.real and l2.real > l3.real and l1.real < l3.real:
        eig1 = l2.real
        eig2 = l3.real
        eig3 = l1.real
        Eigval = [eig1,eig2,eig3]
elif l1.real > l2.real and l2.real < l3.real and l1.real < l3.real:
        eig1 = l3.real
        eig2 = l1.real
        eig3 = l2.real
        Eigval = [eig1,eig2,eig3]
elif l1.real > l2.real and l2.real < l3.real and l1.real > l3.real:
        eig1 = l1.real
        eig2 = l3.real
        eig3 = l2.real
        Eigval = [eig1,eig2,eig3]
else:
        eig1 = l1.real
        eig2 = l2.real
        eig3 = l3.real
        Eigval = [eig1,eig2,eig3]
```

```
            self.output.M = np.log(Eigval[0] / Eigval[2])
            self.output.K = np.log(Eigval[0] / Eigval[1]) / np.log(Eigval[1] / Eigval[2])
            A, B, C, D = vector.plane([self.output.Xmean, self.output.Ymean, self.output.Zmean], vec)
            print "A=", A
            print "B=", B
            print "C=", C
            print "D=", D
            self.output.A = A
            self.output.B = B
            self.output.C = C
            self.output.D = D

# from Stewart, 1999 p. 851 (find the perpendicular distance
        def RMSE(self):
            RMS = []
            for p in self.coords:
                num = (self.output.A * p.Xm) + (self.output.B * p.Ym) + (self.output.C * p.Zm) + self.output.D
                den = sqrt((self.output.A ** 2) + (self.output.B ** 2) + (self.output.C ** 2))
                distance = num / den
                RMS.append(distance**2)
            RMSError = sqrt(sum(RMS) / len(RMS))
            print "Line=",self.output.ID
            self.output.RMSE = RMSError

# equations from Vacher (2000)
        def orientation(self):
            # strike orientation (Eq. #26)
            if self.output.A == 0 or self.output.B == 0 or self.output.C == 0:
                self.output.Dip = -9999
                self.output.Dipdir = -9999
            else:
            ##      # dip section (Eq. #27)
                dipdir = atan(-self.output.A/self.output.B)
                dipdir = round(dipdir * 180 / np.pi,0)

                # dip angle (Eq. #30)
                dip = atan(sqrt((self.output.A**2 + self.output.B**2)/self.output.C**2))
                dip = round(dip * 180 / np.pi,0)
                self.output.Dip = dip

        ## set up partial derivatives to establish dip direction
                # (comments on p. 33)
                dzdx = -self.output.A/self.output.C
                dzdy = -self.output.B/self.output.C
                if dzdx < -0.01 and dzdy > 0:
                    dipdir = 180 - abs(dipdir)
                    self.output.Dipdir = dipdir
                elif dzdx > 0 and dzdy > 0:
                    dipdir = 180 + abs(dipdir)
                    self.output.Dipdir = dipdir
                elif dzdx > 0 and dzdy < 0:
                    dipdir = 360 - abs(dipdir)
                    self.output.Dipdir = dipdir
                elif dzdx < 0 and dzdy < 0:
                    if dipdir < 0:
                        dipdir = 0 + abs(dipdir)
```

```
                else:
                    dipdir = 90 - dipdir
                self.output.Dipdir = dipdir
            elif dzdx < 0.01 and dzdx > -0.01 and dzdy > 0:
                dipdir = 180
            elif dzdx == 0 and dzdy < 0:
                dipdir = 0
            elif dzdx > 0 and dzdy == 0:
                dipdir = 270
            else: #dzdx < 0 and dzdy == 0:
                dipdir = 90

    def writer(self,outfile):
        outfile.writerow([self.output.ID, self.output.N_points, round(self.output.Xmean,1),
                          round(self.output.Ymean,1), round(self.output.Zmean,1),
                          round(self.output.M,3), round(self.output.K,3), round(self.output.RMSE,1),
                          round(self.output.A,3), round(self.output.B,3), round(self.output.C,3),
                          round(self.output.D,0), self.output.Dip, self.output.Dipdir])

    def out_coord(self,outfile):
        tempx = []
        tempy = []
        for c in self.coords:
            tempx.append(c.Xm)
            tempy.append(c.Ym)

        xmin = np.amin(tempx)
        xmax = np.amax(tempx)
        ymin = np.amin(tempy)
        ymax = np.amax(tempy)
    # calculate linear coefficients
        if self.output.A == 0 or self.output.B == 0 or self.output.C == 0:
            Z1 = -9999
            Z2 = -9999
            Z3 = -9999
            Z4 = -9999
        else:
            a = self.output.A / -self.output.C
            b = self.output.B / -self.output.C
            c = self.output.D / -self.output.C
        # Z1 = Xmin, Ymin
        # Z2 = Xmin, Ymax
        # Z3 = Xmax, Ymin
        # Z4 = Xmax, Ymax
            Z1 = a * xmin + b * ymin + c
            Z2 = a * xmin + b * ymax + c
            Z3 = a * xmax + b * ymin + c
            Z4 = a * xmax + b * ymax + c

        outfile.writerow([self.output.ID, round(xmin,1), round(ymin,1), round(Z1,1)])
        outfile.writerow([self.output.ID, round(xmin,1), round(ymax,1), round(Z2,1)])
        outfile.writerow([self.output.ID, round(xmax,1), round(ymin,1), round(Z3,1)])
        outfile.writerow([self.output.ID, round(xmax,1), round(ymax,1), round(Z4,1)])

#---------------------------program starts here-----------------
def PointsToPlane():
```

```
# read input file
    filein=raw_input("Enter .dbf input file name(and extension): ")
    infile = dbf.Dbf(open(filein, 'r'))
# establish column information
    IDcol = raw_input("What column are the ID values in? ")
    IDcol = eval(IDcol)
    IDcol = IDcol - 1
    Xcol = raw_input("What column are the X coordinate values in? ")
    Xcol = eval(Xcol)
    Xcol = Xcol - 1
    Ycol = raw_input("What column are the Y coordinate values in? ")
    Ycol = eval(Ycol)
    Ycol = Ycol - 1
    Zcol = raw_input("What column are the Z coordinate values in? ")
    Zcol = eval(Zcol)
    Zcol = Zcol - 1
# establish output file names and locations
    outfile1 = raw_input("Enter .csv plane output file name(and extension): ")
    outfile2 = raw_input("Enter .csv bounding points output file name(and extension): ")
    fileout = csv.writer(open(outfile1, 'wb'))
    fileout.writerow(['ID', 'N_points', 'Xmean', 'Ymean', 'Zmean', 'M',
                'K', 'RMSE', 'A', 'B', 'C', 'D', 'Dip', 'Dipdir'])

    out_3D = csv.writer(open(outfile2, 'wb'))
    out_3D.writerow(['ID','X_coord','Y_coord','Z_coord'])

    Xm = []
    Ym = []
    Zm = []
    Xdiff = []
    Ydiff = []
    Zdiff = []

# create table of values
    MainDict = {}

    for rec in infile:
        if not rec[IDcol] in MainDict:
            #MainDict.append(rec[0], Record(rec[0])).
            MainDict[rec[IDcol]] = Record(rec[IDcol])

        currentRec = MainDict[rec[IDcol]]
        currentRec.coords.append(Coord(rec[Xcol], rec[Ycol], rec[Zcol]))
    print "LINE ID = ", MainDict.keys()

    for recKey in MainDict.keys():
        rec = MainDict[recKey]
        rec.average()
        rec.plane_calc()
        rec.RMSE()
        rec.orientation()
        rec.writer(fileout)
        rec.out_coord(out_3D)

    infile.close()

PointsToPlane()
```

Appendix 5. xygrid.vbp

```
<xygrid.vbp>
### Script for reading header files (header.txt) information
### and generating x grid and y grid (as ASCII grid text files)
### for the calculation of raster plane surfaces
### M. Roach (2009)

Private Sub Command1_Click()
Dim hed(10)

Open "C:\LiDAR\test_ground\plane_test\header.txt" For Input As #1
Open "C:\LiDAR\test_ground\plane_test\x.asc" For Output As #2
Open "C:\LiDAR\test_ground\plane_test\y.asc" For Output As #3
n = 0

Do While Not EOF(1)
   n = n + 1
   Line Input #1, a$
   hed(n) = Val(Mid$(a$, 15, 10))
   Print #2, a$
   Print #3, a$
Loop
Close #1

topy = hed(4) + hed(5) * hed(2)

For i = 1 To hed(2)
   For j = 1 To hed(1)
      x = hed(3) + j * hed(5) - 0.5 * hed(5)
      y = topy - i * hed(5) + 0.5 * hed(5)
      Print #2, x
      Print #3, y

   Next j
Next i

Close
End
```

Appendix 6. ArcINFO workflow for synthetic "geological" planes

workflow log file for converting coefficients of plane to raster surface
calculating DEM and plane intersect
converting intersection cells to line
convert line nodes to points

ARC 9.3 (Wed Apr 30 14:02:08 PDT 2008)

additional comments

---------- workflow starts here ----------

convert ASCII to float raster
Arc: asciigrid x.asc x float
Arc: asciigrid y.asc y float
enter grid workspace

Arc: grid

GRID 9.3 (Wed Apr 30 14:02:08 PDT 2008)

set up grid display extent and check x y grid files
Grid: disp 9999
Grid: mape x
Grid: image x
Grid: image y

enter linear coefficients and calculate z values for plane
Grid: 32-270 = 0.6249 * x + 0 * y - 348989.4285
Running...

###check result
Grid: image 32-270

calculate difference raster (i.e. intersection of DEM and plane = 0)
Grid: int = test_dem5 - 32-270
Running...

extract intersection cells (i.e. -5 > out < 5)
Grid: out = (int le 5) * (int ge -5)
Running...

check result
Grid: image out

quit grid

```
Grid: q
Leaving GRID...

### convert grid in out to line
Arc: gridline out intersect
Converting GRID out to Coverage intersect
Thinning...
Vectorizing...
Generalized coverage C:\LIDAR\TEST_GROUND\PLANE_TEST\XX03428000
From: 300 Vertices and 4 Arcs
To: 153 Vertices and 4 Arcs
Removing dangling arcs...
7 unique nodes built for C:\LIDAR\TEST_GROUND\PLANE_TEST\XX03428000
Eliminating pseudo nodes...
Number of Arcs     (Input,Output) = 4 4

### convert line nodes to points
Arc: arcpoint intersect points line 1
Weed tolerance set to 0.000...
Loading arcs from coverage intersect...
Constructing point coverage...

### quit program
Arc: q
Leaving ARC ...
---------- workflow ends here ----------
```

Appendix 7. search_lines.py

```
# search_lines.py created by  M. Cracknell, 2009
# script for generating start and end nodes for lines with orientation based on strike of digitised feature
# centre node based on input file coords

import math
import numpy as np
import csv

def search_lines():
   # establish input parameters from user
   print "This program will output a line file for use in ArcINFO using data generated in from
planesToPoints.py"
   data = raw_input("Structure point file path and extension: ")
   length = raw_input("What is the search length parallel to strike (either side of point)? ")
   length = int(length)
   fileout = raw_input("Output line file path and extension: ")

   data = csv.reader(open(data,'rb'))
   data.next() # skip header

   fileout = csv.writer(open(fileout, 'wb'))

   for row in data:
      dipdir = float(row[13])
      strike = dipdir + 90
      if strike >= 360:
         strike = strike - 360
      else:
         strike = strike
      if strike > 180:
         strike = strike - 180
      else:
         strike = float(strike)

      adj = length * (math.cos(strike * np.pi / 180))
      opp = length * (math.sin(strike * np.pi / 180))

      xmean = float(row[2])
      ymean = float(row[3])

      x1 = round(xmean + opp, 1)
      y1 = round(ymean + adj, 1)
      x2 = round(xmean - opp, 1)
      y2 = round(ymean - adj, 1)

      ID = row[0]
      fileout.writerow([ID])
      fileout.writerow([x1,y1])
      fileout.writerow([x2,y2])
      fileout.writerow(["end"])

   fileout.writerow(["end"])

search_lines()
```

Appendix 8. ArcINFO workflow for converting nodes to line

workflow log file for generating lines

ARC 9.3 (Wed Apr 30 14:02:08 PDT 2008)
additional comments

---------- workflow starts here----------
specify arc output file
Arc: generate search_lines

GENERATE 9.3 (Wed Apr 30 14:02:08 PDT 2008)

generate lines from node file
Generate: input line_nodes.txt
Generate: lines
Creating Lines with coordinates loaded from lines_nodes.txt
Generate: q

Externalling BND and TIC...
build lines
Arc: build search_lines arc
Building lines...
Arc: q

----------workflow ends here----------

Appendix 9. Percentage confidence limits for filtered MOI results

MOI results (degree-of-fit from random sampling)

n = 500	GOOD (<=5°)	OK (<=20°)	MODERATE (<=45°)	POOR (>45°)	UNCERTAIN
No. points difference in dip	30	78	117	61	214
%	6	15.6	23.4	12.2	42.8
Cumulative %	6	21.6	45	57.2	100
No. of points difference in dip direction	29	57	77	123	214
%	5.8	11.4	15.4	24.6	42.8
Cumulative %	5.8	17.2	32.6	57.2	100
No. of points dot product comparison	5	44	112	125	214
%	1	8.8	22.4	25	42.8
Cumulative %	1	9.8	32.2	57.2	100

MOI results after slope and aspect filtering (degree-of-fit from random sampling)

n = 147 (% of total = 29.4)	GOOD (<=5°)	OK (<=20°)	MODERATE (<=45°)	POOR (>45°)
No. points difference in dip	16	52	50	29
%	10.9	35.4	34.0	19.7
Cumulative %	10.9	46.3	80.3	100.0
No. of points difference in dip direction	23	38	48	38
%	15.6	25.9	32.7	25.9
Cumulative %	15.6	41.5	74.1	100.0
No. of points dot product comparison	4	35	60	48
%	2.7	23.8	40.8	32.7
Cumulative %	2.7	26.5	67.3	100.0

MOI results slope and aspect filter rejects (degree-of-fit from random sampling)

n = 139 (% of total = 27.8)	GOOD (<=5°)	OK (<=20°)	MODERATE (<=45°)	POOR (>45°)
No. of points difference in dip	14	26	67	32
%	10.1	18.7	48.2	23.0
Cumulative %	10.1	28.8	77.0	100.0
No. of points difference in dip direction	6	19	29	85
%	4.3	13.7	20.9	61.2
Cumulative %	4.3	18.0	38.8	100.0
No. of points dot product comparison	1	11	50	77
%	0.7	7.9	36.0	55.4
Cumulative %	0.7	8.6	44.6	100.0

Appendix 10. Stereonet comparisons of poles-to-bedding

Note: a) field measured poles-to-bedding (includes MRT data (McClenaghan (comp.), 2007)

b) MOI results poles-to-bedding

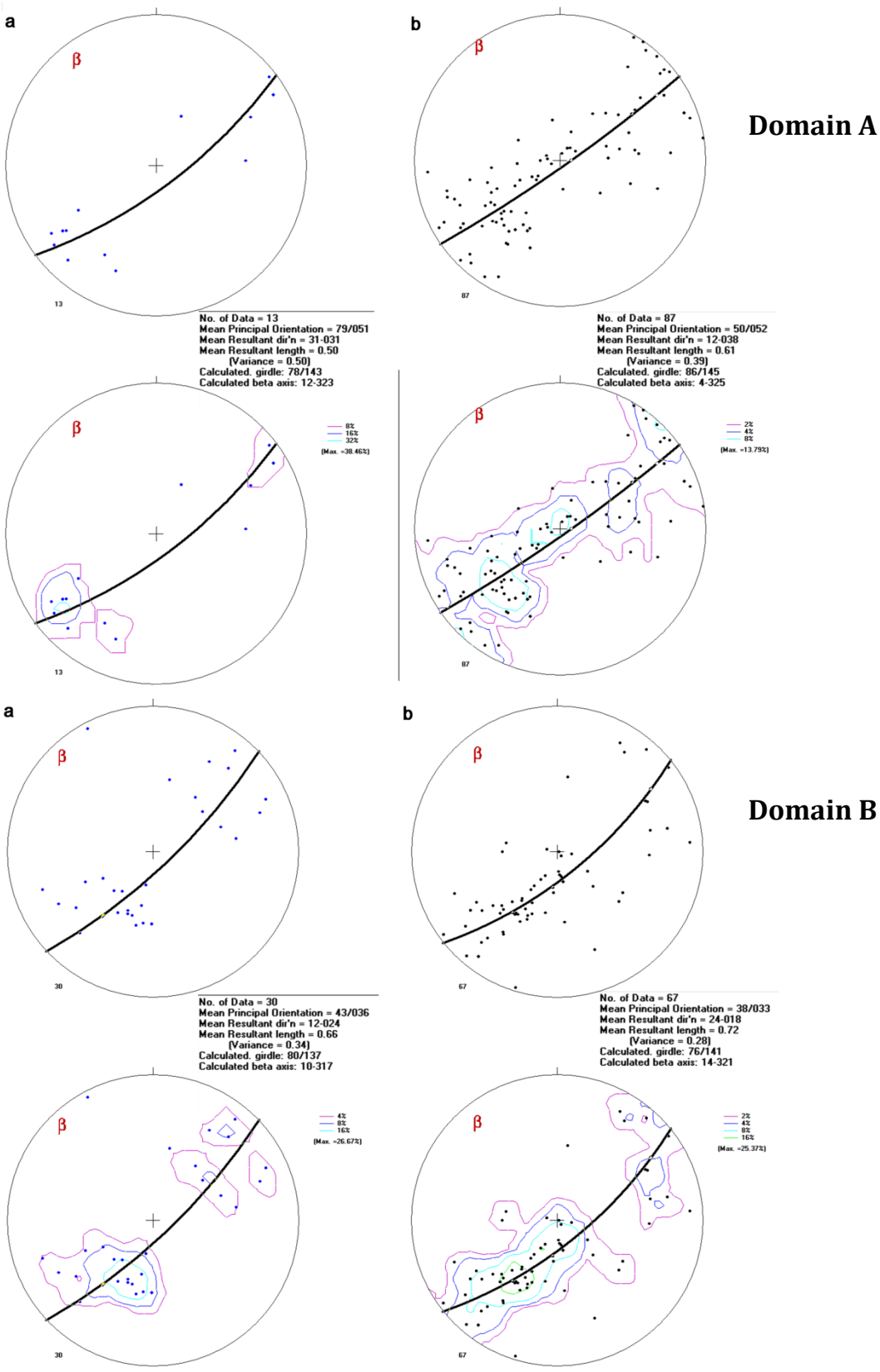

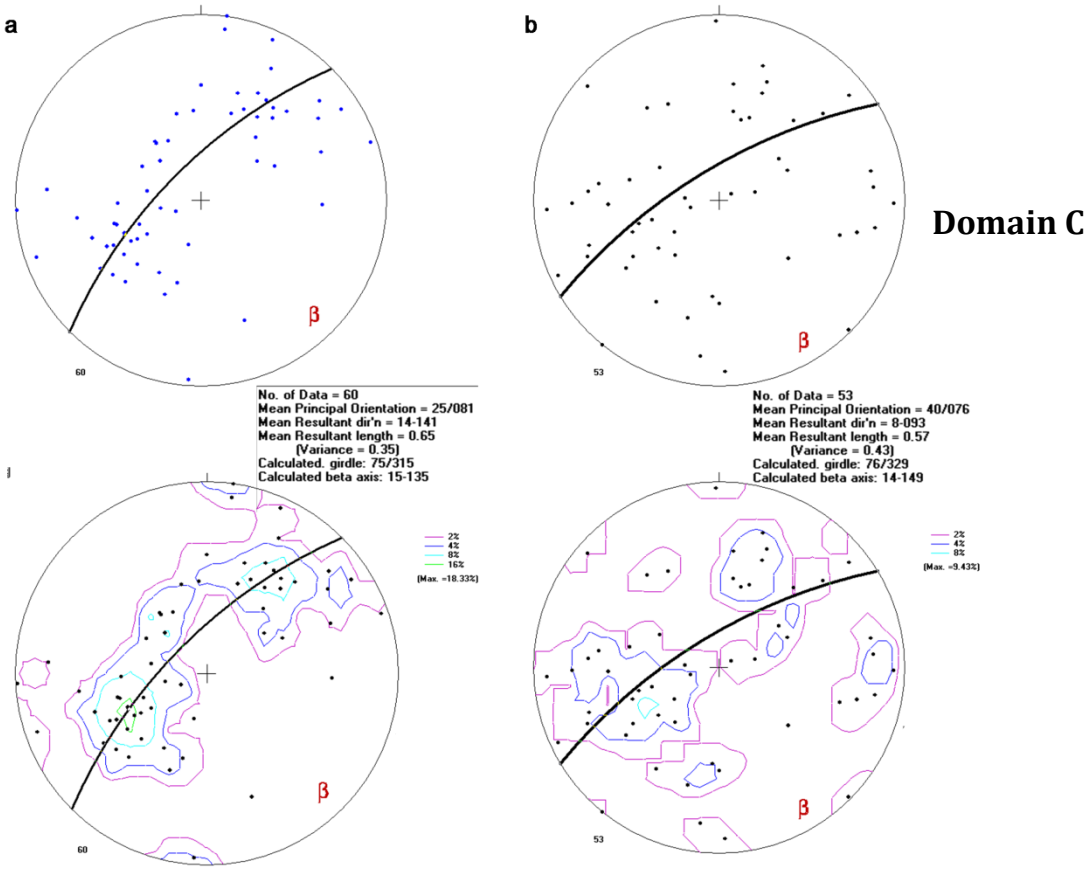

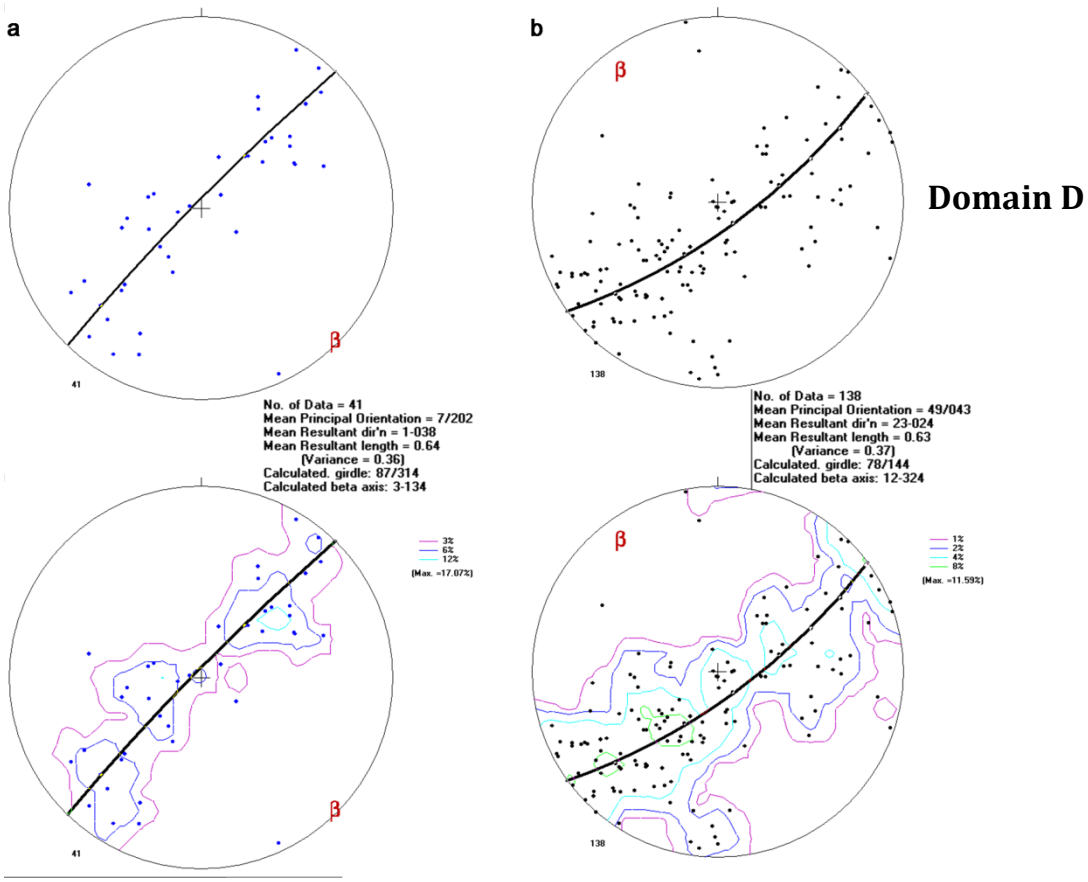

Appendix 10. Stereonet comparisons of poles-to-bedding

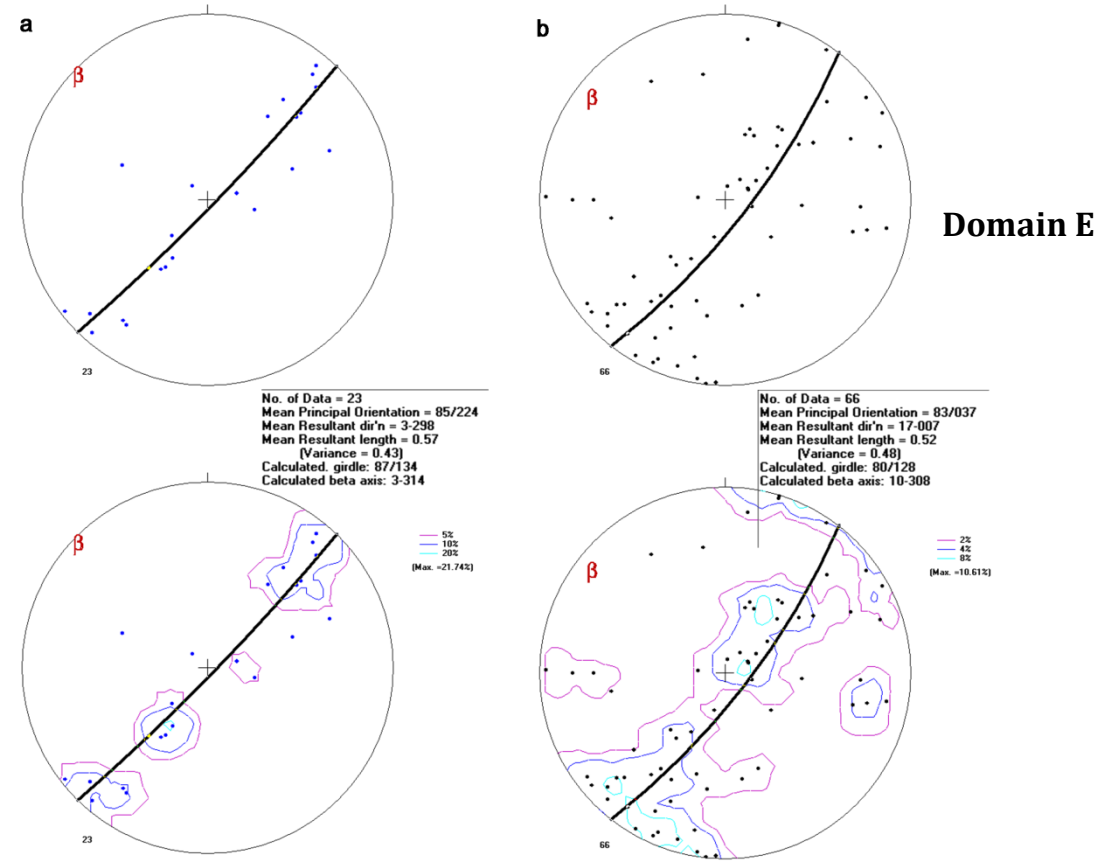

Domain E

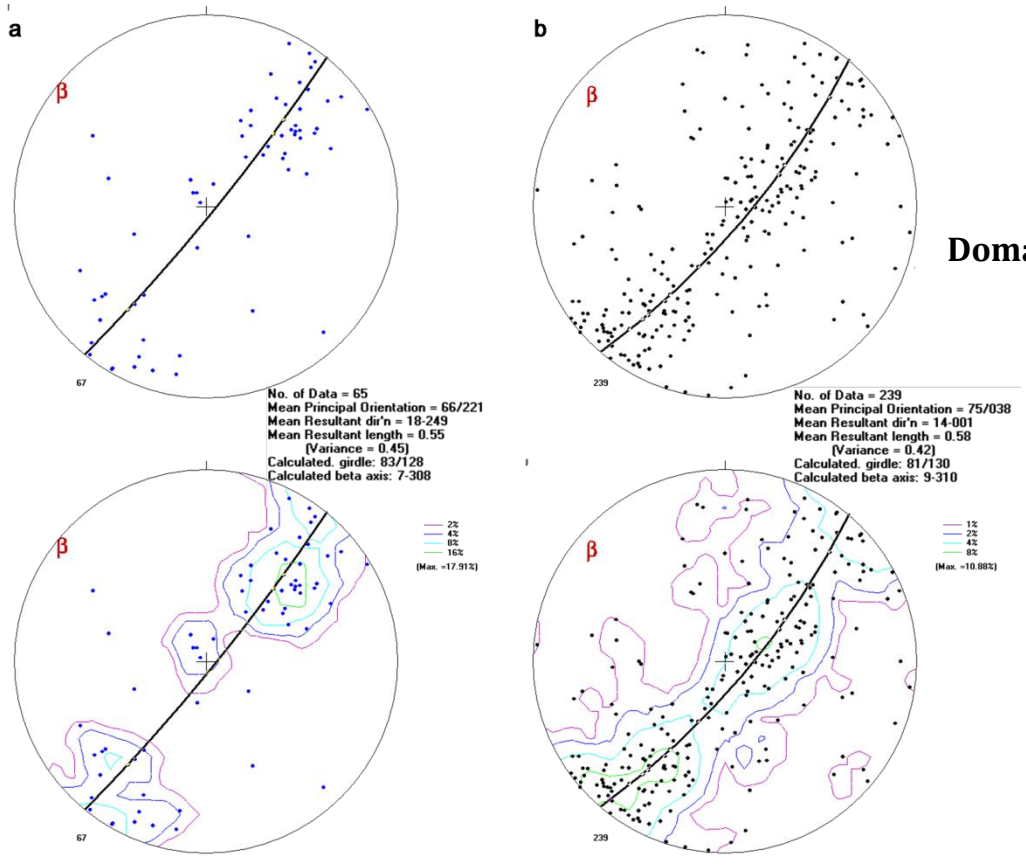

Domain F

Appendix 10. Stereonet comparisons of poles-to-bedding

Appendix 11. Literature review

Correcting and calibrating LiDAR backscatter intensity: Potential laser reflectance applications for earth science research

Matthew J. Cracknell BSc.

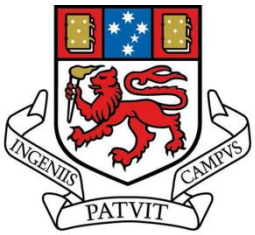

UNIVERSITY OF TASMANIA

A literature review submitted in partial fulfilment of the requirement of a Bachelor of Science with Honours.

Primary supervisor: Dr Michael Roach
Associate supervisors: Dr Arko Lucieer & Dr David Green

Project sponsor: Mineral Resources Tasmania

School of Earth Sciences

University of Tasmania

November 2009

Abstract

Light Detection and Ranging (LiDAR) laser airborne scanners produce high resolution (sub-metre scale) point cloud data containing information on the geometry and backscatter intensity properties of the Earth's surface. Raw LiDAR intensity data must be corrected and calibrated in order to produce meaningful and comparable values of surface reflectance in Wm^{-2}. Until recently there has been very little research into applying LiDAR reflectance imagery to earth science studies. This review investigates the main influences on LiDAR reflectance from illuminated surface materials, including composition, texture/roughness and moisture content then discusses their potential use in the fields of geology, geomorphology and hydrology.

Keywords: LiDAR, intensity, reflectance, corrections, calibration

Table of Contents

List of Figures

1. Introduction

Airborne Light Detection and Ranging (LiDAR) scanning systems are active remote sensing systems that generate dense three-dimensional point cloud data from multiple discrete laser pulse returns. LiDAR data contains accurate geometric information on the Earth's surface and objects (e.g. trees and buildings). Included with this geometric information is a backscattered (laser pulse echo) intensity measurement. Until recently, attention has focused on the analysis of LiDAR point cloud geometry, neglecting backscattered intensity as it is a function of complex interactions between many variables (Jong-Suk, Jung-Il & Kyu-Sung, 2008; Mao *et al.*, 2008).

Wagner *et al.* (2006), Coren & Sterzai (2006) and Kaasalainen *et al.* (2009) conclude that the most important factors influencing measured LiDAR backscatter intensity are:

- scanner system parameters (laser wavelength, transmitted power, source/receiver aperture and Automatic Gain Control state)
- survey geometry (range, incident angle and topography)
- atmospheric attenuation (scattering and absorption)
- surface characteristics (composition, texture/roughness, and moisture content)

Unfortunately, commercial LiDAR system intensity values are rarely corrected or calibrated and merely give a relative measure in Digital Numbers (DNs) of discrete pulse return maximum amplitude (Wagner *et al.*, 2006). Corrections and calibrations are required to convert raw intensity DNs into comparable values of surface reflectance. However, the effective use of LiDAR backscatter intensity as an imaging tool is currently limited due to a lack of robust correction and calibration methods (Kaasalainen *et al.*, 2005; Jong-Suk, Jung-Il & Kyu-Sung, 2008). The Finnish Geodetic Institute's (FGI) Department of Remote Sensing and Photogrammetry is currently conducting research into calibrating corrected LiDAR intensity measurements. One of the FGI's aims is to characterise the reflectance response of different surfaces and objects for use in land cover classification and change detection studies (Kaasalainen *et al.*, 2009).

Full-waveform LiDAR systems are an emerging technology that have the ability to digitise the complete waveform of the backscattered laser pulse. This technology can potentially eliminate some of the uncertainty inherent in the correction and calibration of intensity measurements obtained with conventional discrete pulse systems. For example, full-waveform systems record transmitted laser pulse energy, allowing corrections to be made for variations in this parameter rather than assuming it is constant as with conventional LiDAR systems (Wagner *et al.*, 2006;

Mallet & Bretar, 2009). In the future, full-waveform LiDAR data will be used for more robust analysis of surface reflectance characteristics than is currently possible with conventional discrete pulse systems.

LiDAR intensity is currently being utilised in ways beyond what was originally intended or thought possible (Boyd & Hill, 2007). Several recent studies have explored the use of discrete pulse intensity (corrected and calibrated to varying degrees) in surface feature classification (Jong-Suk, Jung-Il & Kyu-Sung, 2008; Mao *et al.*, 2008), vegetation distribution analysis (Langford *et al.*, 2006; Boyd & Hill, 2007), glacial (Arnold *et al.*, 2006), and archaeological studies (Coren *et al.*, 2005). In most cases, the best results have been obtained when intensity images are integrated with the geometric information collected by LiDAR systems or other remotely sensed datasets (e.g. aerial photography and hyperspectral imagery) (Kaasalainen *et al.*, 2009).

Very few studies have attempted to use LiDAR intensity for earth science applications. Mazzarini *et al*. (2007) and Fornaciai *et al.* (2008) have successfully discriminated and selected different types of volcanic deposits using combined LiDAR geometry and intensity measurements. However, intensity was only corrected for range (source-target distance) resulting in a measure of relative surface reflectance, or pseudoreflectance. These studies concluded that the major influences on intensity were range, surface material texture/roughness at the scale of the laser footprint and mineral composition.

This review discusses the potential for using corrected and calibrated LiDAR backscatter intensity measurements in earth science studies. Evidence is presented to suggest that high resolution LiDAR reflectance imagery may benefit research in the fields of geology, geomorphology and hydrology when integrated with other relevant datasets. However, the influences on surface reflectance response due to mineral composition, surface texture/roughness and moisture content will need to be investigated in more detail if these benefits are to be realised.

2. Corrections and calibration

Conventional discrete pulse multiple return LiDAR systems collect geometric and backscatter intensity information on the Earth's surface and objects. Accurate three-dimensional coordinates of point reflections from surfaces and objects are obtained by measuring the two-way travel time of backscattered laser light while simultaneously knowing the precise location and orientation of

the sensor. LiDAR systems also have the ability to record return pulse intensity, described as the peak energy (signal strength) of a discrete laser pulse return as measured by the receiver (Baltsavias, 1999; Mao *et al.*, 2008). Most LiDAR scanner systems convert recorded intensity to an 8, 12 or 16 bit DN (Coren *et al.*, 2005).

Backscatter intensity DNs obtained with commercial LiDAR systems are neither corrected nor calibrated (Wagner *et al.*, 2006) and as a result obvious differences can be observed between survey flight lines (Boyd & Hill, 2007). The correction process attempts to find a quantifiable relationship between measured intensity and surface target reflectance (Coren & Sterzai, 2006). Corrected intensity measurements are then calibrated using reference targets to obtain comparable values of surface reflectance for use in change detection (Kaasalainen *et al.*, 2005) and robust classification of surface materials and objects (Mallet & Bretar, 2009).

2.1 The LiDAR equation

The measurement principles of LiDAR are based on theory developed for radar remote sensing. Signal strength relationships for both techniques can be explained by the radar equation (Wagner *et al.*, 2006; Höfle & Pfeifer, 2007). The LiDAR equation is a modified form of the radar equation, initially proposed by Baltsavias (1999) and further refined by Wagner *et al.* (2006). The LiDAR equation defines the power (energy) entering the receiver P_r as:

$$P_r = \frac{P_t \, D_r^2}{4\pi \, R^4 \, \beta_t^2} \sigma \qquad (1)$$

P_t is the transmitted power, D_r is the receiver aperture diameter, β_t is the transmitter beamwidth (beam divergence), R is the range (source-target distance), and σ is the backscatter cross-section (Figure 1). The backscatter cross-section defines the target characteristics influencing measured intensity and is given by:

$$\sigma = \frac{4\pi}{\Omega} \rho \, A_S \qquad (2)$$

ρ represents reflectance (or reflectivity), A_S the effective receiving (projected) area and Ω the roughness of the illuminated surface (assuming that the incident energy is scattered uniformly into a cone of solid angle) (Figure 2). Relating the above equations to the intensity measured from a surface, and assuming that it is a horizontal perfect Lambertian (diffuse) reflector, we can conclude that A_S is equal to the laser footprint A_L at normal incidence (Baltsavias, 1999; Wagner *et al.*, 2006) and hence proportional to the inverse cosine of the incident angle θ_i (Ulaby, Moore & Fung, 1982; Arnold *et al.*, 2006; Coren & Sterzai, 2006; Jong-Suk, Jung-Il & Kyu-Sung, 2008). Thus A_S becomes:

$$A_S = \frac{A_L}{\cos\theta_i} = \pi \frac{R^2 B_t^2}{4\cos\ \theta_i} \quad (3)$$

Combining the above equations and incorporating a variable M, representing atmospheric attenuation (Ulaby, Moore & Fung, 1982; Baltsavias, 1999; Kaasalainen *et al.*, 2009) results in a modified version of the LiDAR equation:

$$P_r = \rho \frac{\pi\, P_t\, D_r^2\, M^2}{4\, R^2\, \Omega \cos\theta_i} \quad (4)$$

The following sections examine in detail the components of Eq. 4. Discussions include the implications for P_r when target surfaces do not conform to the assumptions described above.

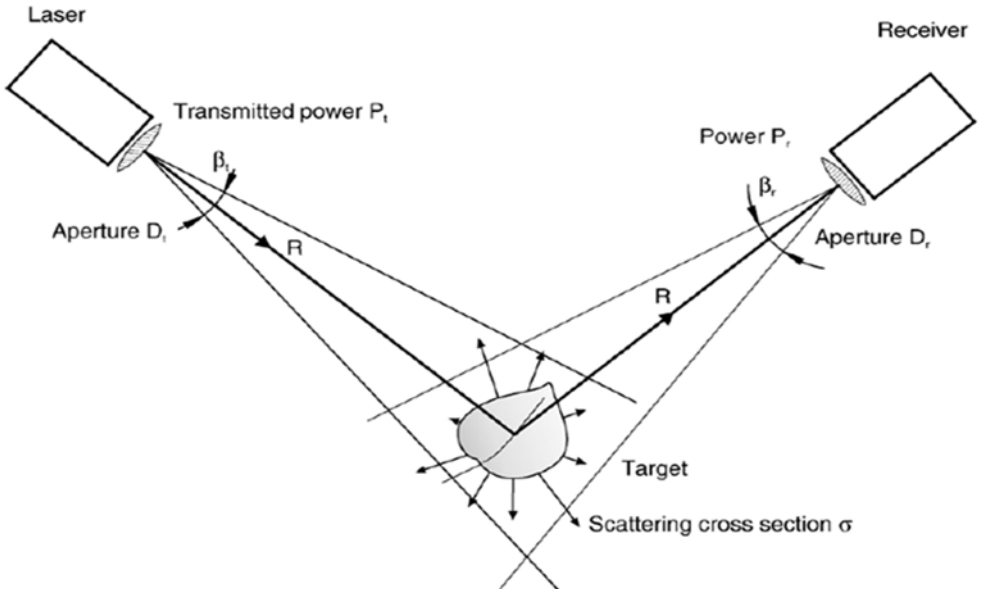

Figure 1 LiDAR equation system parameters, geometry components and backscatter cross-section. The source and receiver are drawn at different locations for clarity (Wagner et al., 2006, p.102)

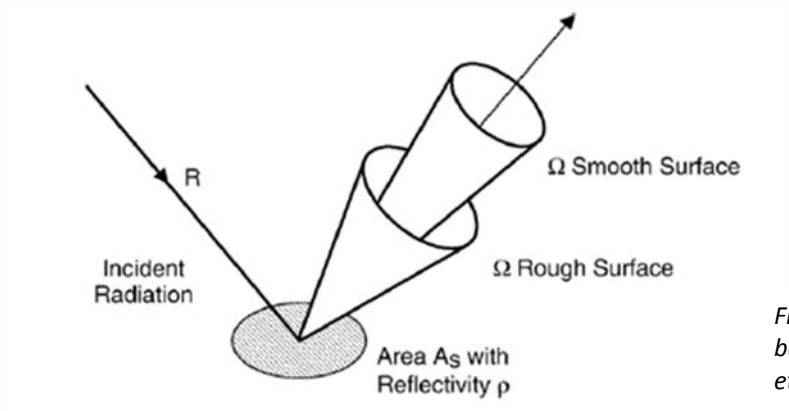

Figure 2 Factors affecting target backscatter cross-section (Wagner et al., 2006, p.102)

2.2 Corrections

Höfle & Pfeifer (2007) define two approaches for correcting LiDAR intensity measurements in order to obtain a value proportional to the reflectance of the illuminated surface. Firstly, the data driven approach uses preselected homogeneous surfaces to empirically estimate the best parameters (via least squares adjustment) for a given correction function. Secondly, a model driven approach corrects intensity based on the physical principles of LiDAR systems. The following sections describe corrections for a model driven approach. It is this approach used by the FGI and will be the norm for corrections applied to full-waveform data (see Section 4).

2.2.1 System parameters

LiDAR system parameters that influence measured intensity include laser wavelength, transmitted power, source/receiver aperture and Automatic Gain Control (AGC) state (Baltsavias, 1999; Boyd & Hill, 2007; Liu, 2008). These parameters must be corrected for if quantitative comparisons between different surveys and systems are to be made (Langford *et al.*, 2006; Kaasalainen *et al.*, 2009).

Backscatter intensity is a function of emitted laser wavelength for two reasons. Firstly, surface reflectance properties determine the proportion of reflected energy at a particular wavelength (Lillesand, Kiefer & Chipman, 2007) and secondly, emitted wavelength affects pulse beamwidth (see below) (Boyd & Hill, 2007). Laser wavelengths in LiDAR systems range from green visible (~500 nm) for terrestrial and bathymetric scanners, to Near-Infrared (NIR) (~700-1000 nm) and Mid-Infrared (MIR) (~1500 nm) for airborne scanners.

Transmitted power is a function of Pulse Repetition Rate (PRR) and laser system stability. PRR is dependent upon the scanning system used, its acquisition mode, and survey flying height, ultimately determined by the perceived application for the data being collected. Höfle & Pfeifer (2007) suggest that PRR is indirectly proportional to a decrease in peak power output, assuming that the transmitter operates with constant average power and pulse duration. Laser system stability refers to the deterioration of emitted power with age and fluctuations in power for individual pulses. Laser system stability in discrete pulse systems cannot be corrected for without detailed information from the manufacturer. This information is not usually available so it is assumed that the pulse energy is constant (Coren & Sterzai, 2006; Starek *et al.*, 2006). Full-waveform systems record the emitted pulse energy and therefore eliminate this assumption from corrections (Wagner *et al.*, 2006).

Laser wavelength and source aperture affect beamwidth. Beamwidth gives a measure of the divergence of a laser beam with distance from the transmitter and is used to calculate the laser footprint (see Eq. 3). Beamwidth is proportional to wavelength and inversely proportional to source aperture (Lillesand, Kiefer & Chipman, 2007).

AGC is a time dependent scaling function imposed on the received signal in order to identify late arrival low amplitude return pulses (Kaasalainen *et al.,* 2007). Recent advances in Digital AGC (DAGC) allow for greater control over and monitoring of the applied gain to a signal (McDonald, 2000). Therefore, deconstruction of the applied gain when using digital systems is possible, although it is uncommon for LiDAR data providers to supply the information necessary for this correction (Jensen, 2007).

2.2.2 Range

According to several authors, range (sensor-target distance) appears to be the most influential geometric property that affects LiDAR intensity (Arnold *et al.*, 2006; Mazzarini *et al.*, 2007; Jong-Suk, Jung-Il & Kyu-Sung, 2008). Range is directly affected by aircraft flying height, scan angle and topography (Baltsavias, 1999; Jong-Suk, Jung-Il & Kyu-Sung, 2008; Mao *et al.*, 2008). As shown in Eq. 4, intensity is a function of the inverse square of the range (Coren & Sterzai, 2006; Starek *et al.*, 2006; Mao *et al.*, 2008; Kaasalainen *et al.*, 2009).

Starek *et al.* (2006) have developed a simple program to correct LiDAR intensity for range effect over horizontal surfaces. It utilises sequential pulse returns and their position, combined with knowledge of the scan angle and aircraft position, to back calculate the distance from sensor to target. The program has the ability to normalise range corrected data to a user defined standard, useful for the comparison of datasets collected with varying flying heights.

2.2.3 Incident angle

The incident angle is defined as the angle that the emitted light makes with a line normal to the target surface (Lillesand, Kiefer & Chipman, 2007), which in turn is a function of sensor orientation, off-nadir scan angle and topography. Simplistically, intensity is proportional to the inverse cosine of the incidence angle such that for horizontal surfaces, as off-nadir scan angles increase intensity decreases (Lichti & Harvey, 2002; Coren & Sterzai, 2006; Jensen, 2007). However, this is complicated by two factors; the concept of Lambertian surfaces and geometry of the local topography at the scale of the laser footprint.

The wavelength of the incident energy and the relative roughness or irregularity of the reflecting surface governs whether the energy reflected is diffuse, specular or a combination of both (Figure 3). A Lambertian surface is defined as an ideal diffuse reflector that reflects energy uniformly in all directions (Lillesand, Kiefer & Chipman, 2007). As Kaasalainen *et al.* (2007) and Mazzarini *et al.* (2007) point out, Lambertian surfaces will return a signal equal in strength regardless of incident angle. Therefore, as surface roughness (relative to wavelength) increases the effect of the incident angle on intensity is reduced thus eliminating the need for corrections. In reality, most Earth surfaces are neither ideal diffuse or specular reflectors and intensity has been found to decrease significantly at incident angles greater than 20° (Kukko, Kaasalainen & Litkey, 2008). This assumption is only applicable to *perfect* Lambertian surfaces and problems arise when correcting intensity as it is difficult to classify surfaces without *a priori* knowledge of their reflection characteristics (Coren & Sterzai, 2006).

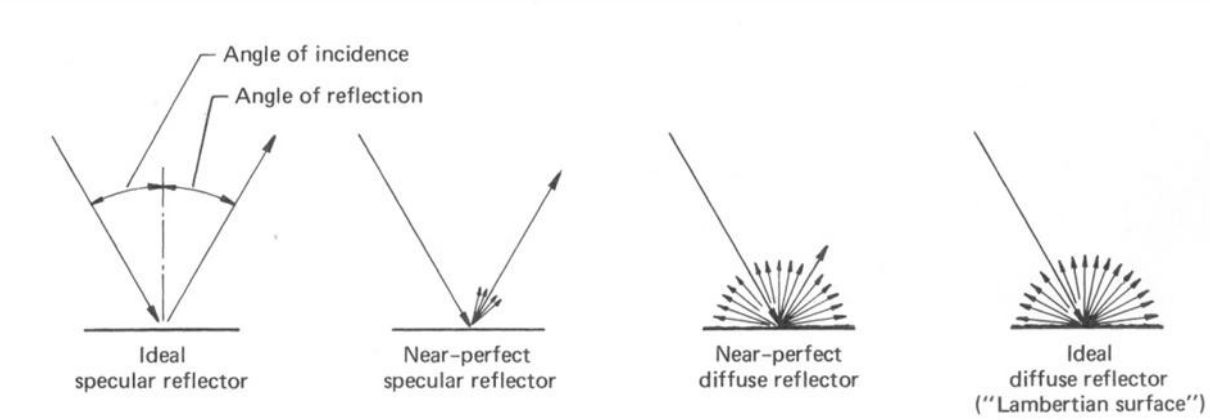

Figure 3 Specular versus diffuse reflections (Lillesand, Kiefer & Chipman, 2007, p.25)

In areas of non-flat topography the incident angle is directly affected by the slope and aspect of the target surface relative to the direction of the incident energy. For conventional discrete pulse LiDAR systems, a proxy for the actual incident angle must be calculated using scan angle, sensor orientation and topographic information. Baltsavias (1999) provides a formula for determining the area of an elliptic laser footprint in undulating terrain, although it only accounts for changes in slope, parallel to the incident energy. It may be possible to apply a correction factor for the projected laser footprint based on this equation. However, no studies have been encountered that attempt to address this issue. As discussed in Section 4, full-waveform LiDAR systems have the ability to determine surface slope within the laser footprint. This will eliminate some of the uncertainty associated with incident angle corrections over undulating terrain associated with conventional discrete pulse systems (Mallet & Bretar, 2009).

2.2.4 Atmospheric attenuation

Atmospheric attenuation of electromagnetic radiation, such as scattering and absorption due to aerosols (i.e. water vapour and particulate matter) is wavelength dependent (Lillesand, Kiefer & Chipman, 2007). Scattering is dominant over absorption for typical LiDAR wavelengths (Kim et al., 2000 in Coren & Sterzai, 2006). The degree to which attenuation affects laser backscatter intensity is dependent on the local weather conditions at the time of survey (Mazzarini *et al.*, 2007). This results in highly irregular and unpredictable spatial and temporal effects on intensity that are difficult to correct (Wagner *et al.*, 2006; Kaasalainen *et al.*, 2007; Höfle & Pfeifer, 2007). More research is needed to fully realise the influence of water vapour on LiDAR intensity measurements (Wagner *et al.*, 2006).

With clear and uniform conditions, atmospheric effects are minor and have been disregarded in some investigations (e.g. Mazzarini *et al.*, 2007). This simplistic approach is not suitable for the comparison of surveys collected over the same area at different times and in different geographic locations (Kaasalainen *et al.,* 2007). Kaasalainen *et al*. (2009) and Höfle & Pfeifer (2007) have approached this issue using the radiative transfer modelling software MODTRAN. MODTRAN outputs an estimate of total atmospheric transmission that can be input into Eq. 4 for intensity corrections.

2.3 Calibration

Calibration is an assessment of the ratio (reflectance factor) of the corrected reflectance of surfaces to that obtained from reference samples with stable reflectance properties (perfectly diffuse Lambertian reflectors) at particular wavelengths (Lillesand, Kiefer & Chipman, 2007; Kaasalainen *et al.*, 2009). The ultimate aim of calibration is to convert high resolution LiDAR intensity measurements into comparable units of absolute reflectance (Wm^{-2}). This will result in a more robust classification of surface materials and has applications in the measurement of the Earth's energy budget for the analysis of climate change feedback mechanisms (Kaasalainen *et al.*, 2005). Calibration reduces the need for separate aerial data acquisition flights with different scanner systems, thus improving data capture efficiency (Kaasalainen *et al.*, 2009).

There are two general approaches to calibrating LiDAR intensity measurements. The first uses laser reflectance measurements from homogeneous materials obtained under laboratory conditions, then determines a reflectance factor by scanning and comparing analogous surfaces during LiDAR surveys (Kaasalainen *et al.*, 2005; Kaasalainen *et al.*, 2009). The second directly measures the reflectance of homogeneous surfaces (e.g. roads) using a spectroradiometer (Jong-

Suk, Jung-Il & Kyu-Sung, 2008). The challenge when calibrating LiDAR intensity measurements is to choose reference surfaces at appropriate spatial, spectral and temporal resolutions (Boyd & Hill, 2007).

Kaasalainen *et al.* (2005) attempted to calibrate LiDAR intensity using synthetic surfaces with differing reflectance properties, while more recently Kaasalainen *et al.* (2009) used commercially available building materials and natural surfaces (e.g. grass and unconsolidated geological materials such as gravels and sand). These investigations suggest that there is a need in the future to focus on the selection of reference surfaces and the uncertainty associated with corrections applied to different scanning systems to improve calibration methods.

Studies such as Coren & Sterzai (2006), Arnold *et al.* (2006) and Mazzarini *et al.* (2007) have only applied geometric corrections to LiDAR intensity measurements resulting in a pseudoreflectance value. Pseudoreflectance is only a relative measure of the reflectance properties of surfaces and objects. It does not provide absolute values of reflectance for comparisons between different surveys.

3. Surface reflectance

Absolute surface reflectance is preserved (ρ in Eq. 2, 3 and 4) after corrections and calibration have been applied to LiDAR intensity measurements. The reflectance of a surface or object is a function of many parameters; the most influential are composition, texture/roughness and moisture content (Coren & Sterzai, 2006; Starek *et al.*, 2006; Boyd & Hill, 2007; Jensen, 2007; Voegtle, Schwab & Landes, 2008).

3.1 Composition

Surface composition determines the reflectance of incident energy at particular wavelengths (Tian *et al.*, 2002; Lillesand, Kiefer & Chipman, 2007; Mao *et al.*, 2008). Unfortunately, airborne LiDAR scanners emit monochromatic laser light at wavelengths equivalent to the NIR and MIR portion of the electromagnetic spectrum with a small bandwidth typically in the range of 2-5 nm (Coren *et al.*, 2005; Jensen, 2007). This results in limited potential to glean radiometric information as a function of composition (Coren *et al.*, 2005; Coren & Sterzai, 2006; Jensen, 2007). However, MIR wavelengths between 1600-2200 nm are thought to contain the most important information on

the reflectance characteristics of geological materials (Lillesand, Kiefer & Chipman, 2007). Tian *et al.* (2002) presents results for the spectral reflectance of sedimentary rocks, as a function of major element composition, providing analysts with base line information with which to investigate compositional influences on LiDAR reflectance measurements.

In theory one would assume that the composition of the illuminated target is the main influence on the measured reflectance of incident laser light at a particular wavelength. However, this is not always the case (Mazzarini *et al.*, 2007; Jong-Suk, Jung-Il & Kyu-Sung, 2008). For example, healthy forest areas in optical remote sensing images appear bright at NIR wavelengths but in LiDAR intensity images (at equivalent wavelengths) the same areas appear dark. Jensen (2007) and Jong-Suk, Jung-Il & Kyu-Sung (2008) speculate that textural influences on the scattering behaviour of incident LiDAR energy within a forest canopy are dominant over composition (see below).

3.2 Texture/roughness

When applying the LiDAR equation we assume that the surfaces being scanned are perfect Lambertian reflectors (Section 2.2.3). In reality this is rarely the case. LiDAR reflectance is a combination of individual reflections from many scattering points within the laser footprint (as with radar) (Kaasalainen *et al.*, 2007; Jensen, 2007). Therefore, the proportion of reflected LiDAR energy is dependent on the texture and roughness of the reflecting surface at the scale of the laser footprint (Mazzarini *et al.*, 2007). For example, specular reflectors will direct a larger proportion of incident energy away from the receiver at off-nadir angles thus appearing dark in LiDAR reflectance images. If the illuminated surface is texturally heterogeneous then reflectance will be a function of the dominant scattering characteristics of the surface in question.

3.3 Moisture content

Surface moisture content is related to local weather patterns, climate, vegetation, the physical properties of materials (porosity and permeability) and relative topographic position. This leads to complex heterogeneous spatial distribution of moisture that is difficult to quantify. Laboratory tests conducted on flat planar surfaces of different materials by Lichti & Harvey (2002) and Voegtle, Schwab & Landes (2008) (at green visible wavelengths ~500 nm) have shown that for most materials surface moisture decreased measured reflectance. Kaasalainen *et al.* (2009) support these findings after conducting field tests where thoroughly wet samples displayed a 30-50% decrease in reflectance (at NIR wavelengths ~700-1000 nm). They suggest that future investigations attempt to find a relationship between the moisture content of surface materials and measured reflectance.

4. Full-waveform LiDAR systems

Full-waveform LiDAR scanners are an emerging technology that digitises the complete backscattered laser pulse waveform recorded as a series of echoes through time (Wagner *et al.*, 2006). The full-waveform signal is processed via a series of steps including: deconvolution of the transmitted and received waveforms in the Fourier domain; Gaussian waveform fitting using an estimated surface function; and waveform modelling. Full-waveform scanners have the potential to remove some elements of uncertainty associated with the corrections and calibration of conventional discrete pulse LiDAR intensity data (Mallet & Bretar, 2009).

Full-waveform systems record emitted pulse energy (P_t in Eq. 1) enabling corrections for fluctuations in the emitted pulse amplitude thus eliminating the assumption that it is constant. Incident angle, as a function of surface slope and scan angle can be estimated from pulse shape, due to an observed spreading and decrease in amplitude of the return pulse with an increase in slope (Figure 4) (Mallet & Bretar, 2009). According to Wagner *et al.* (2006) the use of full-waveform LiDAR systems allow for the accurate calculation of both echo amplitude and width resulting in improved classification of point data for the production of Digital Elevation Models (DEMs) and target classification.

Kaasalainen *et al.* (2009) concludes that in order to calibrate heterogeneous targets full-waveform scanners will be necessary. In the future, full-waveform LiDAR scanning systems could incorporate hyperspectral scanners leading to automated classification of surfaces (Kaasalainen *et al.*, 2007). However, this will require precise feature characterisation obtained via systematic radiometric calibration (Kaasalainen *et al.*, 2005). Full-waveform laser scanners will allow for more robust corrections to be applied to LiDAR backscatter intensity in the future (Boyd & Hill, 2007).

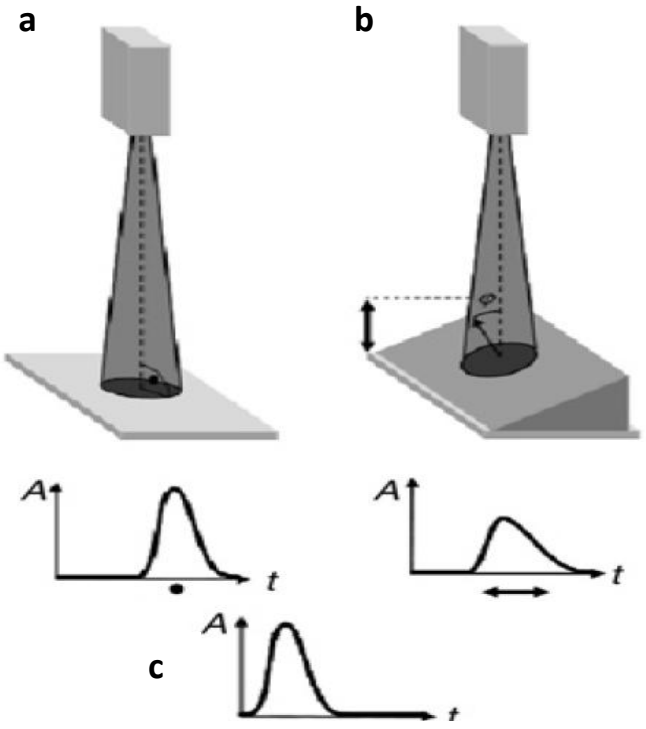

Figure 4 LiDAR full-waveform behaviour for surfaces a) normal to and b) inclined to c) the incident beam, modified from Jutzi & Stilla (2006) in Mallet & Bretar (2009)

5. Feature classification

LiDAR intensity measurements have recently been used in a wide range of feature classification applications. Investigations of this kind have been dominated by vegetation analysis but also include general land cover type discrimination, glacial studies and archaeological investigations. These studies have utilised intensity data corrected to varying degrees. Some researchers (e.g. Brennan & Webster (2006), Langford *et al.* (2006) and Boyd & Hill (2007)) have analysed uncorrected LiDAR intensity and encountered issues with contrasting values between different flight lines and therefore limited their investigations to areas covered by singular (first *and* ground) returns from individual flight lines. Other studies found that the specific interpolation techniques used to create LiDAR intensity images altered the outcome of vegetation type classification (Langford *et al.*, 2006; Boyd & Hill, 2007).

Feature classification with LiDAR intensity utilises the fundamental concept of data integration. At its simplest level data integration involves combining LiDAR geometric and intensity data for the classification of land cover types and objects (Axelsson, 1999). Integrating both geometric and uncorrected intensity data can improve classification of LiDAR point cloud data (ground and non-ground returns) for the production of accurate Digital Elevation Models (DEMs) and Digital Surface Models (DSMs) (Hui *et al.*, 2008; Kaasalainen *et al.*, 2009). At higher levels of integration, both geometric and intensity data are combined with other remote sensing data (e.g. aerial photography or hyperspectral imagery) producing new images for the automated classification of land cover types (Coren *et al.*, 2005; Wagner *et al.*, 2006; Jensen, 2007; Hui *et al.*, 2008). For example, combining aerial photography with LiDAR intensity images has been used for the identification of the reflection properties and geometries of targets (Mao *et al.*, 2008; Jong-Suk, Jung-Il & Kyu-Sung, 2008).

Spectral signature analysis of LiDAR intensity images using traditional remote sensing supervised classification techniques have been successful in defining training areas for the discrimination of vegetation types. These techniques include maximum likelihood classification (Hui *et al.*, 2008) and spatial autocorrelation analysis (e.g. Moran's I) at varying scales (Langford *et al.*, 2006). Other studies discriminated forest age based on canopy height and vegetation density (Jong-Suk, Jung-Il & Kyu-Sung, 2008). Regression analysis of LiDAR intensity (NIR wavelengths) and coincident hyperspectral data conducted by Boyd & Hill (2007) concluded that intensity was a general function of the NIR radiative properties of different vegetation types. Further investigations into these responses showed that differences in vegetation classes were found to be a function of

canopy structure (e.g. species, moisture content and the proportion of living to dead organic matter) which in turn was relative to forest age (Langford *et al.*, 2006; Boyd & Hill, 2007).

Brennan & Webster (2006) integrated colour orthophotographs and uncorrected LiDAR intensity images, linearly interpolated from Triangular Irregular Network (TIN) surfaces, to assess the accuracy of object based land cover classification. In other research, Mao *et al.* (2008) used a process called Spectral Imagery LiDAR Composite (SILC) that combines LiDAR intensity and geometry data fused with coincident aerial photography. The SILC method was able to categorise land cover types based on the typical range of intensity values observed for each class.

Arnold *et al.* (2006) created LiDAR pseudoreflectance images, corrected for range and incident angle assuming horizontal surfaces, to discriminate between bare rock (bedrock and moraines), snow-covered and bare ice surfaces in a glaciated environment. The results of this research concluded that pseudoreflectance in conjunction with geometric information can be used to track changes in snow cover and the difference between ice/snow and ice/rock boundaries over long periods of time.

Coren *et al.* (2005) generated LiDAR reflectance images to enhance automatic data segmentation of hyperspectral imagery for the detection of potential archaeological sites. In this study, corrected and calibrated LiDAR intensity was used for defining general land cover categories. These categories were then further subdivided using a Principle Component Analysis technique to classify hyperspectral images, which were then integrated with DEMs and DSMs produced from LIDAR point cloud data. The final images were able to define, with reasonable accuracy, the location of surface/sub-surface archaeological heritage.

6. Earth science applications

There is a distinct lack of earth science research investigating the use of LiDAR intensity/reflectance data. I propose that with appropriate corrections and calibration it will be possible to use LiDAR reflectance imagery for applications in the fields of geology, geomorphology and hydrology. The best results will be obtained when using full-waveform LiDAR data integrated with other information; this includes field surveys, DEMs generated from LiDAR point clouds and a variety of remote sensing datasets such as hyperspectral imagery.

To date the only investigations into the use of LiDAR intensity measurements for purely geological/geomorphological applications has been the discrimination of extrusive igneous materials of different ages at Mt Etna (Mazzarini *et al.*, 2007) and geomorphological expression at Mt Stromboli (Fornaciai *et al.*, 2008). These studies combined LiDAR DEMs and intensity corrected for range only and found a relationship between pseudoreflectance, landforms, surface texture and alteration minerals. Surface texture was a function of surface morphology and age, providing a foundation for exploring these influences on intensity at the scale of the laser footprint. Mazzarini *et al.* (2007) found an inverse relationship between pseudoreflectance and volcanic deposit age concluding that this response was due to increased surface weathering causing a more subdued micro-topography. However, volcanic deposits older than six years of age displayed an increase in pseudoreflectance values, this was attributed to a relative increase in the proportion of alteration minerals at the surface (predominantly oxides). Fornaciai *et al.* (2008) combined slope and aspect topographic derivatives with pseudoreflectance images to distinguish between four of the most common types of volcanic deposits.

One major factor in the success of the volcanic material and landform investigations was the lack of vegetative cover within the study areas. Mazzarini *et al.* (2007) analysed the pseudoreflectance response from vegetated surfaces and found that vegetation had a major influence on results. This is due to the fact that for multiple LiDAR echoes (from a single pulse) the first two reflections intercept approximately 90% of the total reflected signal power (Mallet & Bretar, 2009). Therefore, if geological interpretations are to be successful in areas of dense vegetation the attenuation of the laser pulse as it filters through the canopy must be removed (Fornaciai *et al.*, 2008). This can be achieved either by removing the influence of vegetation from the dataset altogether or employing full-waveform scanners during surveys.

Selecting singular returns (i.e. single recorded return for an individual laser pulse) and filtering reflections from non-ground objects (i.e. buildings) (Jong-Suk, Jung-Il & Kyu-Sung, 2008), is a simple approach to eliminating the effects of vegetation on surface reflections. However, this filtering step will reduce the resolution of the data set considerably, especially in densely vegetated areas. The complete waveform of the backscattered pulse contains information on both vegetation structure and intensity response (Mallet & Bretar, 2009). It may be possible to quantify the effect of non-ground surface features from the full-waveform and therefore remove this from the surface reflectance response.

Many authors (e.g. Lichti & Harvey (2002) Coren & Sterzai (2006), Starek *et al.* (2006), Kaasalainen *et al.* (2007) and Kaasalainen *et al.* (2009)) agree that surface texture/roughness is a major

component of the LiDAR backscatter reflectance response. It is feasible that the classification of surfaces based on their textural characteristics is a viable means of discriminating surface materials. Reflectance pattern analysis combined with geometric data, may also provide information that can be use for delineating contrasting lithologies and/or landforms.

Laboratory experiments conducted by Tian *et al.* (2002) investigated the reflectance of sedimentary rocks using a halogen light source at wavelengths ranging from 400-2500 nm with a detection resolution of 2-4 nm. In this study, reflectance was tentatively correlated major element composition (i.e. oxides). Further investigations into the intensity response of geological materials (i.e. rocks with composite mineral content) at wavelengths emitted by LiDAR systems will aid in rock and soil type discrimination. Unfortunately, because wavelengths emitted by LiDAR systems laser are monochromatic, compositional classification will only be possible where good spectral seperatability of minerals is available (Höfle & Pfeifer, 2007).

Another important application for LiDAR intensity and geometry is for use in hydrological studies. Moisture content has been found to play an influential role in reflectance response of surface materials in LIDAR intensity data (Lichti & Harvey, 2002; Langford *et al.*, 2006; Coren & Sterzai, 2006; Voegtle, Schwab & Landes, 2008; Kaasalainen *et al.*, 2009). This information may be able to characterise changes in surface moisture content, in otherwise relatively homogeneous geological materials (Arnold *et al.*, 2006; Kaasalainen *et al.*, 2007) enabling the identification of hydrological flow paths for use in environmental monitoring.

Fully realising the potential for high resolution LiDAR reflectance data to aid earth science research will necessarily require high levels of data integration (Coren & Sterzai, 2006). Field surveys that relate surface properties to measured reflectance are needed for analysts to begin to understand the complex interaction of variables that influence reflectance. The integration of full-waveform LiDAR with remotely sensed data will improve our understanding of the geometric and thematic properties of the Earth's surface (Wagner *et al.*, 2006). Remotely sensed geological information is not restricted to spectral reflectance imagery (i.e. hyperspectral data, RADAR) it also includes geophysical datasets such as radiometric, potential field data and Electromagnetic Methods.

7. Conclusions

LiDAR backscatter intensity measurements have the potential to provide high resolution reflectance information on the Earth's surface and above ground objects. To date this information has not been fully investigated and has only been applied to real world examples on a few occasions. This is in part due to the complexity of the laser backscatter response and the uncalibrated and uncorrected raw format of the intensity measurements supplied by commercial LiDAR surveyors.

In order to use LiDAR intensity measurements for land surface classification it is necessary to correct the raw intensity data for a range of variables. These include system parameters, range, incident angle, and atmospheric attenuation. After corrections have been applied, calibrations are necessary to define comparable values of surface material reflectance for analysis between different surveys and datasets. Using full-waveform LiDAR data can eliminate some of the gross assumptions that are made when correcting and calibrating conventional discrete pulse LiDAR intensity (Wagner *et al.*, 2006; Mallet & Bretar, 2009).

LiDAR reflectance response of illuminated surface materials is primarily a function of composition, texture/roughness and moisture content (Coren & Sterzai, 2006; Wagner *et al.*, 2006; Kaasalainen *et al.*, 2009). Further investigations into the role that these influential variables have on surface reflectance will be necessary if LiDAR reflectance data is to be applied to earth science studies.

The most promising finding of this review is the realisation of the potential for high resolution LiDAR reflectance data, integrated with geometric information and other datasets, to be used in the fields of geology, geomorphology and hydrology. The influence of mineral composition and texture on surface reflectance will provide a means of discriminating between contrasting lithologies and landforms (Mazzarini *et al.*, 2007; Fornaciai *et al.*, 2008). The ability to determine moisture content from surface reflectance analysis may be applicable to hydrological studies (Kaasalainen *et al.*, 2009). However, realising the full range of LiDAR data applications for the next generation of earth science studies will require dedicated research.

8. References

Arnold, N. S., Rees, W. G., Devereux, B. J. & Amable, G. S., 2006: 'Evaluating the potential of high resolution airborne LiDAR data in glaciology', *International Journal of Remote Sensing*, **Vol. 27, no. 6**, pp. 1233-1251.

Axelsson, P., 1999: 'Processing of laser scanner data-algorithms and applications', *ISPRS Journal of Photogrammetry and Remote Sensing*, **Vol. 54, no. 2-3**, pp. 138-147.

Baltsavias, E. P., 1999: 'Airborne laser scanning: basic relations and formulas', *ISPRS Journal of Photogrammetry and Remote Sensing*, **Vol. 54, no. 2-3**, pp. 199-214.

Boyd, D. S. & Hill, R. A., 2007: 'Validation of Airborne LiDAR Intensity Values from a Forested Landscape Using Hymap Data: Preliminary Analyses', in P Rönnholm, H Hyyppä & J Hyyppä (eds), *Workshop on Laser Scanning 2007 and SilviLaser 2007*, International Archives of Photogrammetry, Remote Sensing and Spatial Information Sciences, Espoo, Finland, **Vol. XXXVI (Part 3 / W52)**, pp. 71-76.

Brennan, R. & Webster, T. L., 2006: 'Object-orientated land cover classification of LiDAR-derived surfaces', *Canadian Journal of Remote Sensing*, **Vol. 32, no. 2**, pp. 162-172.

Coren, F. & Sterzai, P., 2006: 'Radiometric correction in laser scanning', *International Journal of Remote Sensing*, **Vol. 27, no. 15**, pp. 3097-3104.

Coren, F., Visintini, D., Prearo, G. & Sterzai, P., 2005: 'Integrating LiDAR intensity measures and hyperspectral data for extracting of cultural heritage', in *Proceedings of Italy–Canada 2005, Workshop on 3D Digital Imaging and Modeling: Applications of Heritage, Industry, Medicine and Land*, Padova, Italy.

Fornaciai, A., Bisson, M., Landi, P., Mazzarini, F. & Pareschi, M. T., 2008: 'A LiDAR survey of Stromboli volcano (Italy): DEM-based geomorphology and Intensity analysis', *unpublished manuscript for peer review only, International Journal of Remote Sensing*, p. 26.

Höfle, B. & Pfeifer, N., 2007: 'Correction of laser scanning intensity data: Data and model-driven approaches', *ISPRS Journal of Photogrammetry and Remote Sensing*, **Vol. 62, no. 6**, pp. 415-433.

Hui, L., Liping, D., Huang, X. & Deren, L., 2008: 'Laser Intensity Used in Classification of LiDAR Point Cloud Data', in *IEEE International Geoscience and Remote Sensing Symposium, 2008*, Boston, Massachusetts, **Vol. II**, pp. 1140-1143.

Jensen, J. R., 2007: *Remote Sensing of the Environment: An Earth Resources Perspective*, 2nd edition, Pearson Prentice Hall, Upper Saddle River, New Jersey, p. 592.

Jong-Suk, Y., Jung-Il, S. & Kyu-Sung, L., 2008: 'Land Cover Characteristics of Airborne LiDAR Intensity Data: A Case Study', *IEEE Geoscience and Remote Sensing Letters*, **Vol. 5, no. 4**, pp. 801-805.

Kaasalainen, S., Ahokas, E., Hyyppa, J. & Suomalainen, J., 2005: 'Study of surface brightness from backscattered laser intensity: Calibration of laser data', *IEEE Geoscience and Remote Sensing Letters*, **Vol. 2, no. 3**, pp. 255-259.

Kaasalainen, S., Hyyppa, H., Kukko, A., Litkey, P., Ahokas, E., Hyyppa, J., Lehner, H., Jaakkola, A., Suomalainen, J., Akujarvi, A., Kaasalainen, M. & Pyysalo, U., 2009: 'Radiometric calibration of LiDAR intensity with commercially available reference targets', *IEEE Transactions on Geoscience and Remote Sensing*, **Vol. 47, no. 2**, pp. 588-598.

Kaasalainen, S., Hyyppä, J., Litkey, P., Hyyppä, H., Ahokas, E., Kukko, A. & Kaartinen, H., 2007: 'Radiometric Calibration of ALS Intensity', in P Rönnholm, H Hyyppä & J Hyyppä (eds), *Workshop on Laser Scanning 2007 and SilviLaser 2007*, International Archives of Photogrammetry, Remote Sensing and Spatial Information Sciences, Espoo, Finland, **Vol. XXXVI (Part 3 / W52)**, pp. 201-205.

Kukko, A., Kaasalainen, S. & Litkey, P., 2008: 'Effect of incidence angle on laser scanner intensity and surface data', *Applied Optics*, **Vol. 47, no. 7**, pp. 986-992.

Langford, J., Niemann, O., Frazer, G., Wulder, M. & Nelson, T., 2006: 'Exploring Small Footprint LiDAR Intensity Data in a Forested Environment', in *IEEE International Geoscience and Remote Sensing Symposium, 2006*, Denver, Colorado, pp. 2416-2419.

Lichti, D. D. & Harvey, B. R., 2002: 'The Effects of Reflecting Surface Properties on Time-Of-Flight Laser Scanning Measurements', in *Geospatial Theory, Processing and Applications, ISPRS Commission IV, Symposium 2002*, International Archives of Photogrammetry, Remote Sensing and Spatial Information Sciences, Ottawa, Canada, **Vol. XXXIV (Part 4 / CIG)**.

Lillesand, T. M., Kiefer, R. W. & Chipman, J. W., 2007: *Remote Sensing and Image Interpretation*, 6th edition, John Wiley & Sons Inc., Hoboken, New Jersey, p. 756.

Liu, X. Y., 2008: 'Airborne LiDAR for DEM generation: Some critical issues', *Progress in Physical Geography*, **Vol. 32, no. 1**, pp. 31-49.

Mallet, C. & Bretar, F., 2009: 'Full-waveform topographic LiDAR: State-of-the-art', *ISPRS Journal of Photogrammetry and Remote Sensing*, **Vol. 64, no. 1**, pp. 1-16.

Mao, J. H., Zeng, Q. H., Liu, X. F. & Lai, J. Z., 2008: 'Filtering LiDAR Points by Fusion of Intensity Measures and Aerial Images', in *ISPRS Congress Beijing 2008, Proceedings of Commission V*, International Archives of the Photogrammetry, Remote Sensing and Spatial Information Sciences, Beijing, China, **Vol. XXXVII (Part B3b)**, pp. 25-32.

Mazzarini, F., Pareschi, M. T., Favalli, M., Isola, I., Tarquini, S. & Boschi, E., 2007: 'Lava flow identification and aging by means of LiDAR intensity: Mount Etna case', *Journal of Geophysical Research*, **Vol. 112,** p. B02201.

McDonald, M. K., 2000: *Digital Automatic Gain Control (DAGC) for Surveillance Radar Applications: Theory and Simulation*, Technical Report DREO TR 2000-155 October 2000, Defence Research Establishment Ottawa, p. 36.

Starek, M., Luzum, B., Kumar, R. & Slatton, K. C., 2006: *Normalizing LiDAR Intensities*, GEM Center Report No. Rep_2006-12-001, Geosensing Engineering and Mapping (GEM), Civil and Coastal Engineering Department, University of Florida, Gainesville, Florida, p. 11.

Tian, Q. J., Gong, P., Xu, B., Wang, X., Guo, H. & Tong, Q., 2002: 'Reflectance, dielectric constant and chemical content of selected sedimentary rocks', *International Journal of Remote Sensing*, **Vol. 23, no. 23**, pp. 5123-5128.

Ulaby, F. T., Moore, R. K. & Fung, K. A., 1982: *Microwave Remote Sensing: Active and Passive, Volume II: Radar Remote Sensing and Scattering and Emission Theory*, **Vols. II &III**, Artech House Inc., Norwood, Massachusetts, p. 1064.

Voegtle, T., Schwab, I. & Landes, T., 2008: 'Influences of Different Materials on the Measurements of a Terrestrial Laser Scanner (TLS)', in *ISPRS Congress Beijing 2008, Proceedings of Commission V*, International Archives of the Photogrammetry, Remote Sensing and Spatial Information Sciences, Beijing, China, **Vol. XXXVII (Part B5)**, pp. 1061-1066.

Wagner, W., Ullrich, A., Ducic, V., Melzer, T. & Studnicka, N., 2006: 'Gaussian decomposition and calibration of a novel small-footprint full-waveform digitising airborne laser scanner', *ISPRS Journal of Photogrammetry and Remote Sensing*, **Vol. 60, no. 2**, pp. 100-112.